Characterisation of Specific Parameters of the Framestore pn-CCD for eROSITA

Diploma Thesis

submitted by

Kai Lorenz Freund

Eberhard Karls Universität Tübingen
Fakultät für Mathematik und Physik
Institut für Astronomie und Astrophysik
Abteilung Astronomie

June, 2008

Contents

List of Tables

List of Figures

Zusammenfassung

Ziel dieser Arbeit war es, spezielle Eigenschaften eines framestore pn-CCDs für den niederenergetischen Röntgenbereich (0.1–20 keV) zu vermessen. CCDs sind bildgebende Halbleiterdetektoren, die im Spektralbereich von infrarotem Licht (d.h. Photonenenergien von wenigen Elektronenvolt), bis hin zu Röntgenlicht (etliche tausend Elektronenvolt) sensitiv sind. Das in dieser Arbeit vermessene CCD soll auf der internationalen Satellitenmission Spectrum-RG als Detektor des Hauptinstruments eROSITA eingesetzt werden. Spectrum-RG wird zwischen 2011 und 2012 von Baikonur aus starten und soll mit seinen Instrumenten den Himmel im mittleren bis harten Röntgenbereich beobachten. Dadurch, dass in diesem Energiebereich stellare und galaktische Objekte bis in hohe Entfernungen sichtbar sind, erhofft man sich neue Aufschlüsse über Dunkle Energie und das Schicksal des Universums. Dunkle Energie und Dunkle Materie sind Bestandteile des Universums, deren Zusammensetzung noch weitgehend unbekannt ist. Jedoch beeinflussen sie die kinematischen und thermodynamischen Eigenschaften des Universums auf Skalen von Galaxien, Galaxienhaufen und die Eigenschaften des Raumes selbst.

Das framestore pn-CCD ist ein moderner Röntgendetektor, dessen Vorgänger schon auf erfolgreichen Röntgenmissionen wie XMM-Newton eingesetzt wurden. In dieser Arbeit wurde der Tübinger pn-CCD Messstand modifiziert, um ein CCD für eROSITA betreiben zu können. An diesem CCD wurden eine Reihe von Untersuchungen durchgeführt, um genaueren Aufschluss über das Verhalten des CCD unter Bedingungen auŝerhalb des Labors zu erhalten. Durch die Bahn des Satelliten ergeben sich veränderte Betriebsbedingungen wie zum Beispiel eine andere Temperatur. Das Verhalten bei einer Temperaturänderung wurde anhand der Offset- und Rauscheigenschaften des CCD charakterisiert. Ebenso wurden die Absorptionseigenschaften des auf dem Eintrittsfenster des CCD aufgebrachten optischen Filters durch Beleuchtung mit Leuchtdioden untersucht. Für die Auswertung wurde erstmals die FITS-pipe eingesetzt, ein von den Universitäten Tübingen und Bamberg-Erlangen entwickeltes Software-Paket zur Echtzeitanalyse von bildgebenden Halbleiterdetektoren für die Röntgenastronomie.

Chapter 1

Introduction

In the last fifty years the field of astronomy has experienced a tremendous change in the possibilities of observation. With the advent of space travel, a new scope of scientific observations were made available, as the atmosphere of the earth absorbs broad bands of the in-falling electro-magnetic radiation. Satellites are frequently used as vehicles for space-based astronomy that are able to supply data for five to ten years. Even though astronomy in the optical region is still the most-noticed field in the media, observations in other regions of the electromagnetic spectrum are contributing strongly to our knowledge about stellar and galactic objects.

Spectrum-RG with its main telescope eROSITA is a planned mission which will observe the sky in the X-ray region. The satellite is designated for launch in the time-frame of 2011-2012 and its main scientific goal is the search for dark energy. In the X-ray region, sources are observable at such great distances that with their behaviour assumptions about the evolution of the universe can be made, which is dependent on the amount of dark energy that the universe contains. Both dark energy and dark matter are hypothetical forms of energy and matter. Their effects on the kinematic and thermodynamical properties of large scale structures in the universe are observable but their constitution is so far unknown.

The aim of this thesis is a study of specific properties of the pixilated semiconductor detector that will be used on eROSITA, the framestore pn-CCD. However, the detectors on board of satellites are not operated in specified laboratory conditions. Operational parameters are subject to change either caused by the satellites orbit or by the object the telescope is observing. Of main interest was the behaviour of the detector under a change of temperature and the impact of its illumination with optical light.

In the first chapter, an overview of X-ray astronomy will be given. The generation mechanisms of X-rays will be introduced and X-ray objects will be described both on stellar and galactic scale. Special consideration will be given on the impact of X-ray astronomy in the search for dark energy as this is one of the main goals of the Spectrum-RG mission. In the second chapter, successful X-ray missions and their detection systems will be described. The instrumentation and the scientific goals for

Spectrum-RG and eROSITA are discussed. In the third chapter, the semiconductor physics is described that is needed to understand and operate the detector for the eROSITA telescope. In the fourth chapter the experimental setup is described along with the tools for data analysis. The additional components for the optical illumination of the detector are described in detail. In the fifth chapter the results are presented and discussed. In the outlook, a number of further investigations will be suggested.

Chapter 2

X-Ray Astronomy and Dark Energy

The term *astronomy* usually refers to the research of phenomena on stellar, galactic or extra-galactic scale by means of electromagnetic radiation, which has either been emitted or influenced by the phenomenon in question. In this chapter, a brief overview of the generation mechanisms of X-ray photons ($0.1 - 100\,\mathrm{keV}$) in celestial objects will be given. Furthermore, the search for dark energy and dark matter will be discussed, with special consideration on how X-ray astronomy can help to deepen the knowledge of the structure of the universe.

2.1 X-Ray Astronomy

The spectrum of electromagnetic radiation is divided into regions based on its energy. The energy of a photon, the exchange particle of the electromagnetic radiation, is given by

$$E_{\mathrm{Photon}} = h\nu = \frac{hc}{\lambda} \tag{2.1}$$

where ν is its frequency, λ its wavelength, h the Planck constant[1] and c the speed of light[2]. It ranges from the radio region (all wavelengths greater than 1 mm) over the optical region (wavelengths from 700 nm for red light to 400 nm for blue light) to the X-ray ($10 - 0.01\,\mathrm{nm}$) and gamma region (below 0.1 nm). The higher energy bands are usually denoted with their energy in electron Volt (eV)[3].
A limiting factor for astronomical observations is the Earth's atmosphere. While it supplies the oxygen we need to survive, it also absorbs broad bands of wavelengths of the electromagnetic spectrum. Figure 2.1 shows the transparency of the atmosphere with regard to the wavelength. Some bands are transmitted, like the radio frequencies or visible light, while others are almost entirely absorbed, like the UV spectrum. In order to observe these energy regions, the instruments need to be in

[1] $h = 6.626 \times 10^{-34}\,\mathrm{Js}$; named after the German physicist Max Planck (⋆1858 †1947)
[2] $c = 299\,792\,\mathrm{km/s}$ in vacuum
[3] $1\,\mathrm{eV} = 1.602 \times 10^{-19}\,\mathrm{J}$

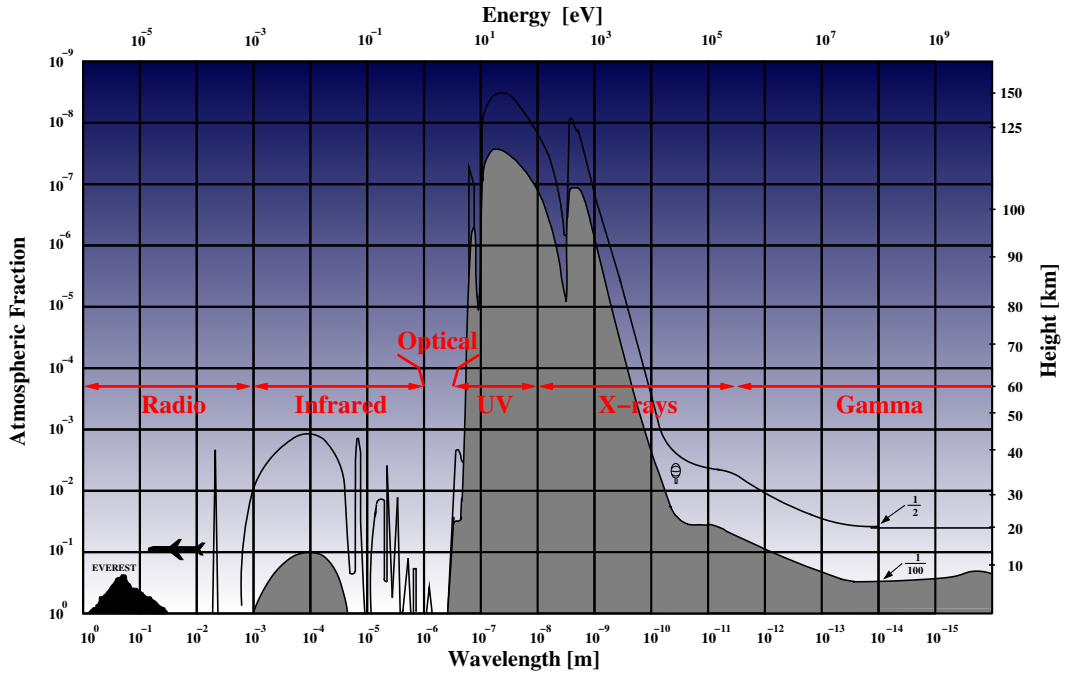

Figure 2.1: The transparency of the earth's atmosphere as function of the wavelength. Upper curve: height where 1/2 of infalling radiation is absorbed, lower curve: 99% absorption. Image: courtesy of Thomas Schanz and Chris Tenzer based on (Reidy et al., 1968)

a higher part of the atmosphere. The absorption is the probability of the incident photon to interact with an atmospheric molecule and therefore a function of the atmospheric height. By interacting with another particle before it is detected, the photon can be scattered away from its axis and therefore be lost for detection purposes.

Even in the transmitted regions, ground-based astronomy may not be viable. Weather effect (clouds, fog, turbulences) or man-made disturbances like scattered light from cities can inhibit accurate measurements. Satellites circumvent the atmospheric absorption but even planes or balloons can reach a height in which some desired regions become visible.

The first observation of an extra-solar X-ray source was therefore tied to the development of rockets, with enough payload to carry an experiment. In 1962, Riccardo Giacconi[4] observed the X-ray source Scorpius X-1 with an array of Geiger counters on board an Aerobee rocket, that was designated to observe fluorescence X-ray emissions on the lunar surface (Giacconi et al., 1962).

X-rays can be emitted by objects with a high temperature or a strong gravitational field, which either means very large stars or stars in states at the end of their life

[4] Italo-American astrophysicist (⋆1931), he was awarded the Nobel Prize in physics in 2002 for his contribution to x-ray astronomy.

— like X-ray binaries or supernova remnants. The flux of X-rays that can be detected is low enough, that with state-of-the-art semiconductor detectors like the pn-CCD on XMM-Newton a simultaneous spectroscopic and imaging measurement can be carried out. In addition, the interstellar medium (gases and particles in the universe that do not belong to a celestial object) is more transparent in the X-ray region (Zombeck, 1990), so sources at great distances can be observed. Therefore, X-ray astronomy allows us to study large scale structures in the universe and make assumptions about cosmological questions like the constituents of the universe.

2.2 Mechanisms of X-ray Generation

In the following, the most predominant physical processes for X-ray generation are briefly introduced. Unless indicated otherwise, the rest of this chapter is based on Unsöld & Baschek (1999), Schneider (2006) and Wilms (2002).

2.2.1 Blackbody Radiation

A radiating object in thermal equlibrium emits an electromagnetic spectrum according to their temperature. An idealised object that absorbs and emits photons across all wavelengths has a characteristic spectrum. These objects are called *black bodies* and the emitted spectrum is dependent on the temperature. This blackbody spectrum was discovered by Max Planck[5] in 1900. The spectral radiation density of a black body is given by

$$B\nu(T) = \frac{2h\nu^3}{c^2} \frac{1}{\exp(h\nu/k_B T) - 1} \tag{2.2}$$

where T is the objects temperature and k_B the Boltzmann constant[6]. The position of maximum intensity of the spectrum is given by the displacement law

$$\nu_{\max} = \frac{T}{hb} \tag{2.3}$$

where b is Wiens constant[7]. For an object to emit blackbody radiation primarily in the X-ray region, its temperature needs to be in the region of $10^6 - 10^8$ K. The sun, a G-type yellow dwarf[8] star, has an effective surface temperature of 5 778 K and its spectrum would therefore have a maximum around 500 nm if it were a perfect black body.

[5] German physicist (⋆1858 †1947)
[6] $k_B = 1.381 \times 10^{-23}$ J/K, named after the Austrian physicist Ludwig Boltzmann (⋆1844 †1906)
[7] $b = 2.898 \times 10^{-3}\,\mathrm{m \cdot K}$
[8] Stars are classified by their mass and luminosity *O-B-A-F-G-K-M*, from highest to lowest.

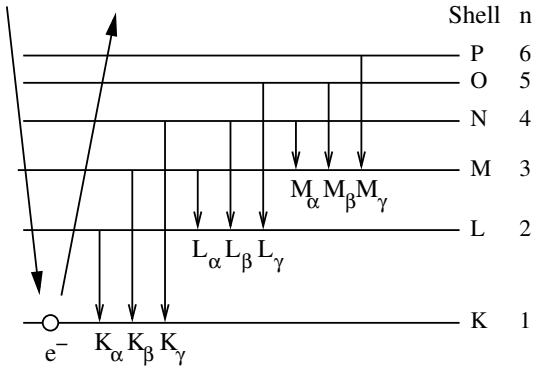

Figure 2.2: Model of characteristic X-ray emission from shell transitions.

2.2.2 Characteristic Radiation and Fluorescence

Both characteristic radiation and fluorescence may occur, when a free electron or photon interacts with a bound electron in a low shell of a specific atom. The states of an electron which is bound in an atom are characterised by their main quantum number n. The lowest shell is the K-shell ($n = 1$) followed by the L-shell ($n = 2$), M-shell ($n = 3$) and so on. Electron transitions between the shells are named by the shell the electron now occupies, so all transition ending in the K-shell form the K-series. The originating shell is denoted by a subscript (for example α for a transition of a single shell) as seen in figure 2.2.
When a free electron of sufficient energy interacts with an atom, it can ionise an electron in one of the inner shells. The unoccupied level is then filled by the capture of a free electron or with a bound electron of an upper shell. As the shells for each type of atom have distinct and discrete energy levels, a characteristic line for each shell transition will be emitted. Therefore, this process is called *characteristic radiation*. If the ionisation was caused by an incident photon, it is called *fluorescence*. Both are bound-free processes, as in both cases an electron is removed from its bound state around an atomic nucleus.
Characteristic X-rays mostly originate from K-series transitions in heavier elements. These processes are relevant to detect X-ray radiation. Fluorescense emission, however, plays a key role in many astrophysical contexts like accretion discs, clusters of galaxies and supernova remnants.

2.2.3 Bremsstrahlung

A charged particle like an electron is deccelerated by the Coulomb field of another charged particle like an atomic nucleus. Bremsstrahlung is a free-free scattering process, since both participants are not bound to a certain state or change this

state by this interaction. The emitted electromagnetic spectrum of the decelerated electron has a maximal frequency $\nu_{\max}$ that is given by the electrons energy $E_{e^-} = h\nu_{\max}$. The emission of bremsstrahlung in terms of the free-free emissivity ϵ_ν^{ff} is therefore tied to the temperature of the electrons and hence their energy is

$$\epsilon_\nu^{ff} \propto Z^2 n_e n_i \sqrt{\frac{1}{k_B T}} e^{-hp\nu/k_B T} \tag{2.4}$$

where $n_{e/i}$ are the densities of electrons and ions respectively and Z is the ion's charge. X-ray emission of thermal bremsstrahlung can be found in hot gases ($T \sim 5 \times 10^7\,\mathrm{K}$) of massive galaxy clusters ($M \sim 10^{14}\,\mathrm{M}_\odot$).

2.2.4 Comptonisation

In Compton scattering a photon is elastically scattered by a free, stationary electron and transfers a part of its energy and momentum. The energy E' that the photon still retains after the interaction is given by

$$E' = \frac{E}{1 + \frac{E}{m_e c^2}(1 - \cos\theta)} \tag{2.5}$$

where θ is the angle by which the photon is scattered. When the interacting electrons are not assumed to be stationary, but to have a temperature T_e so that their energy is of the order of the photon, the energy transfer can be from electrons to photons. In the non relativistic case and assuming an average over the whole solid angle Ω of the scattered particles, the transferred energy can be approximated as (Wilms, 1998)

$$\frac{\Delta E}{E} \approx \frac{4k_B T_e - E}{m_e c^2} \tag{2.6}$$

so in the case of $4k_B T_e > E$, a positive amount of energy will be transferred to the photon and they will be scattered to higher energies. As a side effect the electron gas is being cooled by this process. A spectrum that shows photons that underwent several of these inverse scattering processes is called comptonised. This process can be observed in the halo of black holes and in jets of active galactic nuclei.

2.2.5 Nuclear Processes

Nuclear processes such as radioactivity may also emit photons in the X-ray region by gamma decay. An example of such a decay is the inverse beta decay of the iron isotope $^{55}_{26}\mathrm{Fe}$. The electrons in the K-shell (or 1S-orbit) of an atom have a non-negligible probability of interacting with the nucleons in the atoms core. A proton can capture this electron and create a neutron under the emission of an electron neutrino ν_e. This leaves a space in the K-shell of the newly formed manganese atom

$^{55}_{26}$Mn unoccupied, and it will be replaced by either an electron from the L-shell (K_α emission) or the M-shell (K_β emission):

$$^{55}_{26}\mathrm{Fe}\,(e^-, \nu_e)\,^{55}_{26}\mathrm{Mn}^*\,(h\nu)\,^{55}_{26}\mathrm{Mn} \tag{2.7}$$

The emitted photons have an energy of 5.90 keV for the K_α transition and 6.41 keV for the K_β transition. This isotope is commonly used to calibrate X-ray detectors.

2.2.6 Synchrotron radiation

In the presence of a magnetic field, moving charged particles like electrons are affected by the Lorentz-force

$$\vec{F}_{\mathrm{Lorentz}} = \frac{q}{c}(\vec{v} \times \vec{B}) \tag{2.8}$$

where $\vec{v}$ is the velocity of the particle and $\vec{B}$ the magnetic field. If the particles have a speed component perpendicular to the magnetic field, they are forced on a helical orbit around the magnetic field lines. Since an orbit is a form of acceleration ($|\vec{v}|$ will not necessarily change but $\vec{v}$ will) the electron will emit electromagnetic radiation. The energy of the emitted photon is dependent on the strength of the magnetic field and the speed of the electron. The frequency is given by

$$\nu_{\mathrm{syn}} = \frac{3\gamma^2 eB}{4\pi m_e c} \approx 4.2 \times 10^6\,\gamma^2 \left(\frac{\mathrm{B}}{1\mathrm{Gauss}}\right) \mathrm{Hz} \tag{2.9}$$

where $m_e = 511\,\mathrm{keV/c^2}$ is the rest mass of the electron and $\gamma = \frac{1}{\sqrt{1-(v/c)^2}}$ the Lorentz factor for relativistically accelerated particles. To reach frequencies in the X-ray region, the magnetic field needs to be extremely high[9] (the order of 10^6 G) and the electrons need to be at highly relativistic speeds ($\gamma > 1\,000$).

2.2.7 Cyclotron radiation

In environments of extremely high magnetic fields, the electrons which move in a magnetic field cannot acquire certain energies. The electron orbits around the magnetic field lines become quantised. These energy levels are called Landau niveaus and their energy is given by (Truemper et al., 1978)

$$E_n = m_e c^2 \left(\sqrt{1 + \left(\frac{p_\parallel}{m_e c}\right)^2 + n\left(\frac{B_n}{B_{\mathrm{crit}}}\right)} - 1\right) \tag{2.10}$$

where$n = (2j + l + 1)$ stands for general quantum number, angular momentum and spin quantum number respectively. If the magnetic field surpasses the critical field

[9] In comparison, the earths magnetic field is of the order 0.5 G.

$B_{\text{crit}} = (m^2c^3/eh)$ relativistic effects have to be taken into account and the Landau niveaus are not equidistant. For a magnetic field $B \ll B_{\text{crit}}$ the distance between the Landau niveaus is given by the "$12 - B_{12}$" rule:

$$E_{cyc} = E_{n+1} - E_n = \frac{he}{m_e c} B = 11.6\,\text{keV} \left(\frac{\text{B}}{10^{12}\text{G}} \right) \tag{2.11}$$

High-energy photons from deeper regions of the star can excite these transitions and therefore the stars spectrum will show characteristic cyclotron absorption lines around the energies given by the "$12 - B_{12}$" rule. The emitted cyclotron photons are scattered in random directions and can excite more transitions, so they are lost from the angle of view and show up as an absorption line.

2.3 X-ray Objects

In the following, some of the brightest celestial X-ray sources are introduced. X-rays are caused by a wide range of physical mechanisms and are therefore also emitted by distinctly different stellar or galactical objects. A general introduction to X-ray objects is given even though only certain classes of X-ray emitters might be of interest for a single mission.

2.3.1 Stellar Sources

Stars on the main sequence do not have a temperature that permits the emission of thermally generated X-rays as their effective surface temperature is orders of magnitudes too low. The effective temperatures of stars range from 40 000 K for O-type stars to 5 778 K for the sun (G-type) or 3 000 K for M-type red dwarfs. However, the sun[10] does show an X-ray luminosity of the order of $L_\odot/L_x \approx 10^{-6}$. Heavier stars show even stronger X-ray emissions.

Magneto acoustic heating – The sun shows its X-ray emission not homogeneously distributed over the whole surface but rather from arched structures called *coronal loops* shown in figure 2.3. These are caused by magnetic field tubes which develop in the convection zone of the star and can arch outwards into the corona, the thin and hot outmost part of the sun's atmosphere. These field tubes are magnetic field lines that were "twisted" because stars have a differential rotation. Ionised coronal material will be trapped between the field lines, causing them to heat up via collisions. Temperatures exceeding 10^6 K can be reached and the matter can cool itself by emitting radiation through the optically thin corona. This heating mechanisms is dependent on the strength of the magnetic field, its rotational velocity and its age because

[10] The total luminosity of the sun is $L_\odot \approx 3.839 \times 10^{33}$ erg/s.

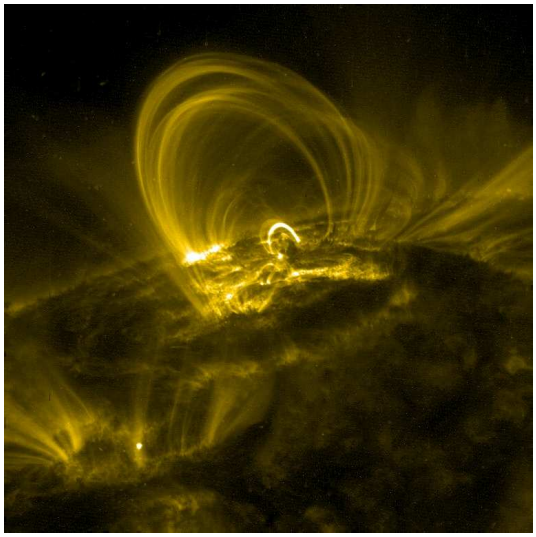

Figure 2.3: Coronal loops of the sun, taken by the NASA mission *Transition Region and Coronal Explorer* [http://trace.lmsal.com].

the star loses angular momentum to the surrounding interstellar medium over time (Hempelmann et al., 1995).

Stellar winds – Heavier stars like O-type stars ($L \approx 10^6 L_\odot$) show even stronger X-ray emissions, the X-ray spectrum is mostly thermal. Since O-type stars have much faster stellar winds than G-type stars ($\dot{M}_O \approx 3\,000\,\mathrm{km/s}$ in comparison to $\dot{M}_\odot \approx 300\,\mathrm{km/s}$), a heating by stellar winds has been suggested by Lucy & White (1980). "Blobs" of matter are driven outwards by radiation pressure and heat the surrounding gas, which itself is not affected by the radiation.

2.3.2 Supernovae and their Remnants

A star is defined as a stellar object that reaches a temperature in its core region high enough to sustain thermonuclear fusion. In main sequence stars like our sun, hydrogen is burning to helium. This is called *pp-chain*, as two protons start the chain. The three different branches of the chain that leads to helium are as follows

$$\begin{array}{lllll} {}^1H\,(p,e^+\nu)\,{}^2D\,(p,\gamma)\,{}^3He & \rightarrow & {}^3He\,({}^3He,2p)\,{}^4He & & ppI \\ & \rightarrow & {}^3He\,(\alpha,\gamma)\,{}^7Be & \rightarrow \quad {}^7Be\,(e^-,\nu)\,{}^7Li\,(p,\alpha)\,{}^4He & ppII \\ & & & \rightarrow \quad {}^7Be\,(p,\gamma)\,{}^8B\,(e^+\nu)\,{}^8Be\,(2\alpha) & ppIII \end{array} \tag{2.12}$$

Once the hydrogen density in the star's core becomes too low to sustain the pp-chain, the star will contract and heat up in the central region and may start further fusion processes. Nuclear fusion is strongly dependent on the temperature that the

star will reach in the core region, so only stars with a helium core that exceeds $0.35\,M_\odot$ will ignite higher fusion processes. Helium burning, carbon burning, neon burning and finally silicon burning will produce elements up to iron, since iron has the highest binding energy of all the elements. No energy will be gained by a fusion process to higher elements than iron. Once either the temperature is not sufficient to ignite higher fusion or the fusion to iron has stopped, the star will collapse due to its own gravitation. The end of the star is now highly dependent on its remaining mass[11].

Smaller stars ($\approx 1\,M_\odot$) will end their life with a core that consists mostly of carbon and oxygen. Once they collapse, the pressure in the core will degenerate the electron gas inside, but no further fusion processes will be initiated. These stars are called *white dwarfs*. If a white dwarf is part of a binary system in which matter can be transferred onto the white dwarf, the star can reach the Chandrasekhar-limit of $M_{Ch} = 1.44\,M_\odot$, which is the mass limit for a gas of degenerate electrons to withstand gravitational pressure. If the accretion continues and if the temperature is sufficiently high to ignite carbon burning throughout the star, the star will end its life in a thermonuclear explosion called *thermonuclear supernovae* or *type Ia*.[12]

Heavier stars that started their life with a mass $\gtrsim 8\,M_\odot$ will have reached the final stages of the fusion chain, so their core consists of iron and nickel. For a core of a mass between $M_{Ch} = 1.44\,M_\odot$ and the Oppenheimer-Volkoff limit of $M \approx 3M_\odot$ the pressure becomes high enough to force the protons in the star to undergo an inverse beta decays: $p + e^- \rightarrow n + \nu_e$. Since the star now consists mainly of neutrons, it is called a *neutron star*[13]. Once the collapse starts, the core will again reach the Chandrasekhar-limit. Since no nuclear reaction can be ignited anymore, the core will continue to collapse until it reaches the density of nuclear matter ($\approx 10^{14}\,\mathrm{g/cm^3}$). The strong force and neutrino degeneracy will forbid a further collapse of the core. In-falling matter that can reach speeds up to $0.2\,c$ will rebound and produce a shock wave. These supernovae are called *hydrodynamic supernovae* or *type Ib,c / II*, depending on their spectral composition and the mass of the progenitor star.

Above the Oppenheimer-Volkov limit, the pressure becomes high enough to force the core to collaps into a singularity. Its radius becomes smaller than the Schwarzschild-radius $R_S \approx 3\,(M/M\odot)[\mathrm{km}]$ which is the radius of an object from which no information can escape. As no photons can escape this object anymore, it is called a *black hole*.

During their outbreak, a supernovae can release energies exceeding $10^{51}\,\mathrm{erg/s} \approx 10^8\,L_\odot$, which is a luminosity of the order of a galaxy. Hard X-rays are produced by decaying radioactive materials, that are formed during the outbreak. The shock wave caused by the supernova will "plough" through the former star's shedded outer

[11] A star may lose a big fraction of its mass during its life via for example stellar winds.

[12] Since SN Ia develop as a cause of a mass transfer over M_{Ch}, the lightcurve of the resulting supernova will be nearly the same. For this reason Ia supernovae are used as *standard candles* to determine the distance in which the supernova has occurred.

[13] Neutron stars are considerably smaller than white dwarfs. Typical values are: $R_{\mathrm{WD}} \approx 10^7\,\mathrm{m}$, $R_{\mathrm{NS}} \approx 10^4\,\mathrm{m}$

layers and the ambient gas and heat it up to 10^7 K, so that it will become a plasma and emit a thermal X-ray spectrum. In addition to the thermal X-ray spectrum, supernova remnants also show strong line emissions in the X-ray band. This is caused by heated electrons which can ionise the surrounding gas and cause characteristic line emission from C, N, O or Ne atoms. The electrons can even be accelerated to energies up to the TeV range, which will be influenced by the magnetic field to emit synchrotron radiation.

2.3.3 X-ray Binaries

A binary system consists of two stars rotating around their centre of mass (CM). X-ray binaries are subspecies of binaries that emit their radiation primarily in the X-ray band. Even binaries that have white dwarf as the primary object emit X-rays, but their main spectrum is in the UV or the optical band. X-ray binaries consist of a black hole or neutron star as the compact object and a normal companion.
The main source of power for binary systems in general is accretion. A particle of mass m falling onto a gravitating object with mass M and radius R will release the energy $E = mGM/R$, which will give particles falling onto a small stellar object enough energy to either heat the surface or the ambient gas and emit X-rays[14]. For a mass flow or *accretion rate* $\dot{m}$ onto the object, its X-ray luminosity is of the order

$$L_x \approx \dot{m}\frac{GM}{R}. \tag{2.13}$$

The radius of a compact object like a neutron star or a black hole is much smaller than the radius of a white dwarf. Thus, mass flow onto these two types of compact objects will yield a much higher X-ray luminosity. Possible models for accretion onto the compact object are:

Roche lobe overflow – Under the assumption that the two stars are point masses in a corotating system, the *Roche-potenial* ϕ_{Roche} (seen in figure 2.5) is given by the gravitational potentials of the masses M_1, M_2 as well as the centrifugal potential.

$$\phi(\vec{r}) = -\frac{GM_1}{|\vec{r} - \vec{r_1}|} - \frac{GM_2}{|\vec{r} - \vec{r_2}|} - \frac{1}{2}(\vec{\omega} \times \vec{r})^2 \tag{2.14}$$

The points in the Roche potential where the potential disappears are called Lagrange-points L_1-L_5. During its evolution, the normal companion star can reach a size where it extends over the L_1 point between the two stars (the equipotential area containing the L_1 point is called *Roche lobe*). Matter from the companion star that extends over the L_1 point is accreted onto the compact

[14] A particle falling into a black hole can liberate up to 30% of its rest-mass of $E = mc^2$, which makes accretion a more efficient energy source than hydrogen burning, which can only liberate 7‰ (Rosswog & Bruggen, 2003).

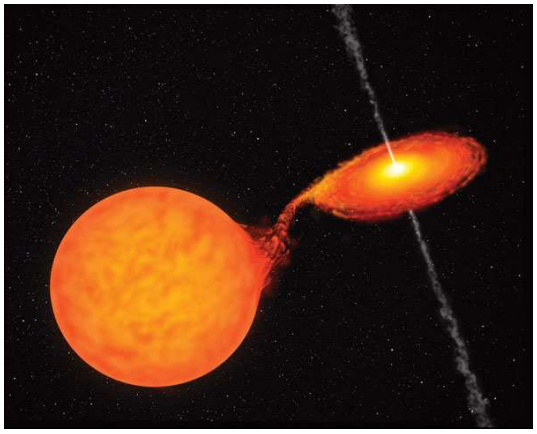

Figure 2.4: Artists sketch of an X-ray binary system (Eckart, 2002). The companion star (left) fills its Roche lobe and matter is accreting onto the smaller compact object (right).

object through L_1. Energy and momentum conservation dictates that the mass will not fall onto the compact object directly, but will spiral on Keplerian orbits around the star. Energy and angular momentum can be transported away via friction, so the matter will spiral inwards and form rotating viscous discs called *accretion discs*. The temperature in accretion discs can exceed 10^7 K and will therefore emit thermal X-rays. The streaming matter also has to impact on the compact object itself, where it produces a *hot spot* in the case of a neutron star of a white dwarf. Figure 2.4 shows a sketch of a binary with a black hole. Jets protruding from the compact object are also often observed in these systems. Their origin is still debated.

Wind Accretion – Early type stars (*O,B*) have very strong mass loss rates by solar winds. These stars are close to the so called *Eddington limit* where radiation pressure from the stars interior almost cancel the gravitational pull inwards. A wind from an O-type star may emit between $10^{-6} - 10^{-4}\,\mathrm{M}_{\odot/\mathrm{a}}$ while the sun emits $2 \times 10^{-14}\,\mathrm{M}_{\odot}/\mathrm{a}$. A fraction of this mass ($10^{-4} - 10^{-3}$ of the total wind) will be accreted by the smaller companion. An accretion disc may form, but it will be smaller due to the fact that the emitted gas has a smaller angular momentum than in the case of Roche lobe overflow. This process is also called *Bondi-Hoyle accretion* (Bondi & Hoyle, 1944).

Be-accretion – Early type stars in the range of *O9-B2* have both a high rotational speed and a strong stellar wind, so that disc-like "bulges" can develop around the stars equatorial region. These bulges show emission lines in the B-stars spectrum (therefore these objects are also called Be star). If a compact companion like a neutron star is rotating in an elliptical orbit around the Be-star close enough that it passes in the periastron through the bulge it

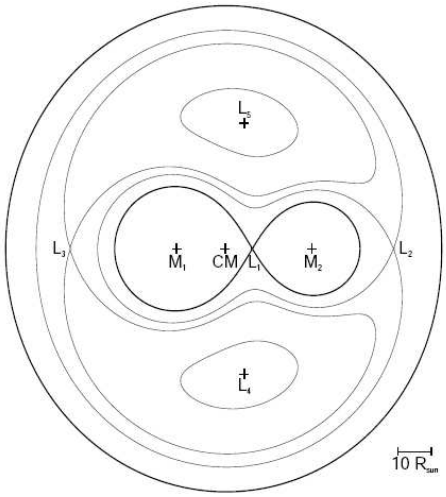

Figure 2.5: Roche potential in a binary system. (Wilms, 1996)

can accrete mass. This will result in irregular X-ray outbursts. For this reason Be-accretors are X-ray *transients* opposed to the *persistents* with a continuous X-ray emission (Ziolkowski, 2002).

There are two types of X-ray binaries, which are distinguished by the companion star:

Low mass X-ray binaries (LMXB) – The donor star, the non-compact star, has a spectral class of A or later and therefore a mass $M \lesssim 1.2 M_\odot$. Because of the low mass of the donor, its stellar wind is small and its nuclear evolution is slow. Wind accretion is therefore not possible, but once the donor expands over its Roche lobe, an overflow will occur. Due to the slow evolution this state can persist for over 10^8 years. If the compact object is a neutron star, its original magnetic field of 10^{12} G will have decayed by the time the system evolves into an X-ray binary up to a point where it will not influence the accretion mechanisms. During the long accretion phase, the neutron star will gather angular momentum from the accreting matter, which may cause it to increase its rotational velocity to milliseconds giving rise to the class of accreting *millisecond pulsars*. In addition to the discs and the hot spots X-ray emission ($\lesssim 10\,\mathrm{keV}$), the matter falling onto the star can compress and ignite a nuclear reaction with high X-ray emission on the stars surface. These so called *X-ray bursts* last for the order of 1 s and the system will settle into the old state afterwards.

High mass X-ray binaries (HMXB) The donor star has a spectral class of B or earlier and a mass of $M \gtrsim 10 M_\odot$. Heavy stars like O-type stars have short

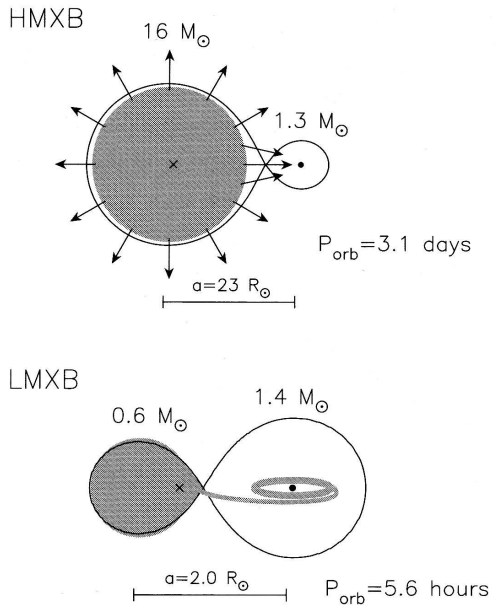

Figure 2.6: High and low mass X-ray binary (Rosswog & Bruggen, 2003). The HMXB is mainly powered by wind accretion on the young neutron star, the LMXB accrets via Roche lobe overflow.

lifetimes in comparison to G-stars like our sun, so they are only observed in star-forming regions in the galactic disc. The main accretion mechanism in HMXB is the wind accretion due to the strong stellar wind of the heavy star. These stars emit broadband spectra which extend from energies of keV to tens of keV. The neutron star is in general young, therefore its magnetic field is strong enough ($\approx 10^{12}$ G) to force the in-falling material along its field lines and channel it towards its magnetic poles. Since the spin axis of the neutron star is not necessarily aligned with the magnetic axis, the X-ray emission from the magnetic poles pulsates with the neutron stars spin period ($10 - 300$ s). The high density of the magnetic field at the poles will cause cyclotron lines, which can be used to measure the neutron star's magnetic field.

2.3.4 Active Galactic Nuclei

Active galactic nuclei (AGN) are core regions of galaxies that show very strong electromagnetic emission either in the whole spectrum or distinct energy bands. The luminosity of the core that extends ≈ 1 pc may even be equal to the rest of the galaxy. Even though a multitude of different properties of AGNs are observed, a common structure has been suggested by Urry & Padovani (1995). In the centre, a super-massive black hole (SMBH) with a mass of $10^6 - 10^{10}\,M_\odot$ is gathering mass

with an accretion disc. The heated material will be emitting in the X-ray region. A dust torus and several gas clouds of varying speeds surround the central region. Two jets, a highly relativistic outflow of hot plasma, are emitted from the black hole of radio-quiet AGN. The viewing angle on such a galactic nucleus is very important as some region may be occluded, which will influence the observed spectrum. Examples for AGN are quasars (bright featureless spectrum), radio galaxies (very strong radio lines) or seyfert galaxies (very bright nuclei with emission lines of highly ionised atoms). Due to their brightness, AGNs are amongst the farthest objects we can currently see. Therefore they play a crucial role in cosmology, as their light will be influenced on its way by gravitational lensing effects, so the amount of (dark) matter in the lensing plane can be estimated.

2.3.5 Clusters of Galaxies

Clusters of galaxies like the local group which contains the Milky Way are the biggest gravitationally bound objects known in the universe. They contain $\approx 10 - 10^3$ single galaxies and are together with AGNs the brightest X-ray sources in the sky. Large amounts of intergalactic gas is present, called *inter-cluster medium* (ICM). The gas has temperatures of $10^7 - 10^8\,\mathrm{K}$ and therefore emits X-rays because of bremsstrahlung and recombination lines of highly ionised atoms. Typical of clusters of galaxies are *cooling flows*. The x-ray emissivity of the hot gas is proportional to the density, so the hot gas in the centre loses energy via radiation. Its temperature drops and the gas falls deeper into the gravitational well because the pressure decreases with the temperature. This further compresses the gas and therefore the emission is rising again. Cooling flows are a run-away process until the gas condenses into a star forming region and becomes invisible.

2.4 The Quest for Dark Matter and Dark Energy

Dark matter is commonly referred to as massive particles, that interact via gravitation, but not via electromagnetic radiation. Unlike “ordinary” baryonic matter, dark matter is difficult to detect. Its additional mass influences the gravitational field and therefore the mechanical and thermodynamical behaviour of objects on a galactic scale. Thus, dark matter’s gravitational properties are observable on large scales structures in the universe. Recent discoveries in astronomy not only show that the observed baryonic matter is a fraction of the total mass but also that a form of “dark” energy has to exist in order to explain the kinematic behaviour of the universe. Therefore the search for dark matter and dark energy is vital in order to make assumptions about the fate of the universe on a cosmological scale.

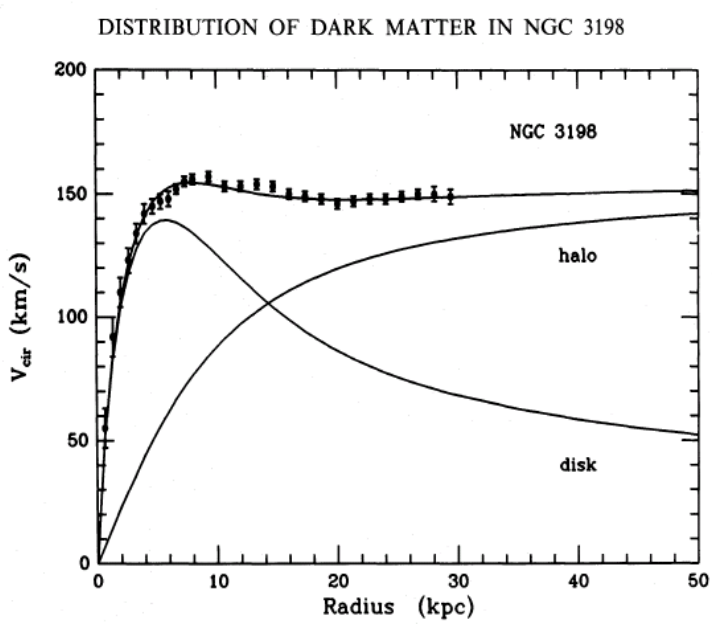

Figure 2.7: Rotational Curve of NGC 3198. In addition, the curve only for the visible matter is shown ("disk") under the assumption that it follows a Keplerian motion around the galactic centre. A halo of non-visible, dark matter can therefore be assumed ("halo") that accounts for the missing rotational speed in the outer regions.

2.4.1 The Friedmann Equations

When considering the motion of the universe as a whole, the question arises if the universe behaves similarly everywhere. This is being assumed by the *cosmological principle*, which says that the universe is homogeneous and isotropic on very large scales ($> 100\,\mathrm{Mpc}$). In 1922, Alexander Friedmann derived a set of equations that are based on the cosmological priciple and describe the motion of space. They can be written in the form:

$$\begin{aligned}\left[\frac{\dot{R}(t)}{R(t)}\right]^2 &= H^2(t) \\ &= H_0^2\left[R^{-4}(t)\Omega_{\mathrm{rad}} + R^{-3}(t)\Omega_m + R^{-2}(t)(1-\Omega_m-\Omega_\Lambda) + \Omega_\Lambda\right]\end{aligned} \tag{2.15}$$

where $R(t)$ is the scale factor, $\dot{R}(t)$ the expansion rate and $H(t)$ the Hubble parameter. Ω_{rad} and Ω_m are dimenstionless density parameters that describe the total amount of either radiation energy or mass in the universe, normalised with the critical density[15]. Ω_Λ is the density parameter associated with the cosmological constant Λ which was introduced to the Friedmann equation by Albert Einstein. The universe was believed to be static and only a constant term in the Friedmann equations allows a static solution. However, in 1929 Edwin Hubble[16] discovered a relation between the redshift of galaxies and their distance (Hubble, 1929). This was first interpreted as a Doppler-shift caused by the velocity of the galaxies. The Doppler-redshift z is given by

$$1 + z = \frac{\lambda'}{\lambda} \tag{2.16}$$

where λ' is the Doppler shifted wavelength. Hubble found that the escape velocity is proportional to their distance $v = H_0 r$, where H_0 is today's Hubble constant[17]. Later the Doppler-redshift was discarded in favour of a redshift that is caused by the expansion of space, which was given the name *Hubble redshift*. Hubble's discovery caused Einstein to revoke the cosmological constant as the "biggest blunder" of his life[18] (Gamov, 1970). However, recent discoveries have shown that the cosmological constant (which is associated with dark energy) not only exists but is also the universes main constituent. Dark energy and dark matter therefore dictate the overall behavious of the universe. The total density for example

$$\Omega_{tot} = \Omega_m + \Omega_\Lambda \tag{2.17}$$

is a measure for the fate of the universe. A total density of $\Omega_{tot} < 1$ is equivalent to a stopping expansion and a collapse, $\Omega_{tot} = 1$ is the critical value where the universe reaches a boundary limit (also called *flat* universe) or $\Omega_{tot} > 1$ is the case of a monotonous growing universe.

[15] The critical density $\rho_{\mathrm{cr}} = 3H_0^2/8\pi G$ marks the line between a collapsing and an ever expanding universe.

[16] American astronomer ($\star$1889 †1953)

[17] Hubble found a constant of $H_0 = 530\,\mathrm{kms}^{-1}\mathrm{Mpc}^{-1}$, which is a factor of 7 higher than newer measurements as the distances used were incorrect.

[18] Original: "..die größte Eselei meines Lebens."

2.4.2 Evidences for Dark Matter

The first evidence for "missing mass" and also dark matter in general was a study of the mass of the Coma[19] galaxy cluster by Zwicky (1937). By applying the virial theorem[20] to the rotational velocity of the cluster, the total mass of the cluster could be estimated and compared to the value taken from the observation of the number of galaxies in the cluster and their brightness. Zwicky found, that the gravity of the galaxies could not explain the rotational velocity of the cluster, as the observed mass was a factor 160 less than what was needed to explain the rotational speed. The term *dark matter* is already used in Zwicky's paper, but it is used in the context of "cool and cold stars, macroscopic and microscopic bodies and gases".
Another example for missing mass are the rotational curves of galaxies. The rotational speed of a galaxy can be derived by assuming an equilibrium between its gravitation and the centrifugal force. This so called Kepler rotation is given by

$$v^2 R = \frac{GM(R)}{R} \tag{2.18}$$

by applying mass-to-luminosity ratios of the visible stars in the galaxy. In the outer regions of the galaxy, the rotational speed should therefore drop with a factor of $\propto 1/R$. Galaxies show a flat rotational curve towards their outer region as seen in figure 2.7. As a solution, a halo of gravitating non-luminous *dark* matter was suggested by van Albada et al. (1985), that extends linearly from the core region outwards. This halo influences the total rotational speed by $v_{dark}^2 = v^2 - v_{lum}^2 = GM_{dark}/R$ so that the mass distribution of the dark matter can be derived. It was found that for the galaxy NGC 3198 the mass of the dark matter halo surpassed the luminous mass by a factor of 6 in the distance of 50 kpc.
Candidates for dark matter include heavy neutrinos, new elementary particles like the *weakly interacting massive particle* (WIMP) or cold baryonic stellar bodies called *massive astrophysical compact halo object* (MACHO) for single objects or *robust association of massive baryonic objects* (RAMBO)[21] for clusters of "dark" objects.
While astronomers try to observe the secondary or indirect influences of dark matter, nuclear physicists have conceived ways to measure the impact of dark matter directly. The *Cryogenic Rare Event Search with Superconducting Thermometers* (CRESST) experiment for example consists of highly shielded sapphire crystals with superconducting tungsten films attached. The tungsten films are operated in the transition state to the normal conducting regime, so when an incident dark matter particle interacts with the crystal lattice via nuclear recoil, the resulting lattice vibrations can be observed by a change in temperarture (Bravin et al., 1999).

[19] Abell 1656
[20] In a gravitational system the average kinetic energy equals half the negative average potential energy $\langle T \rangle = -\frac{1}{2}\langle V \rangle$.
[21] Astrophysicists have humour!

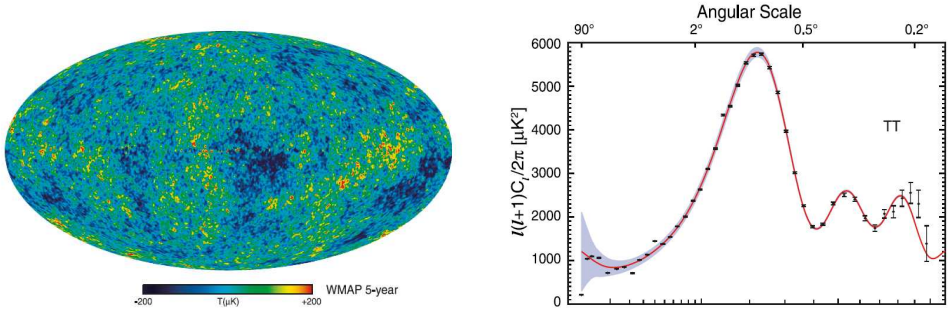

Figure 2.8: The cosmic microwave background (CMB) observed by WMAP. The temperature power spectrum of the CMB in terms of the angular scale. Height and position of the acoustic peaks allow assumptions about cosmological parameters.(Hinshaw et al., 2008)

2.4.3 Evidences for Dark Energy

There are multiple evidences for dark energy. The first was revealed by the study of supernovae of the type Ia. These supernovae are standard candles on a cosmic scale, because their progenitor star reaches the critical mass via accretion and therefore have the same light-curve. A number of supernovae were studied by Riess et al. (2004) with data from ground based telescopes and the Hubble Space telescope up to redshifts of $z \lesssim 2$. For redshifts $z \lesssim 1$ the supernovae are more luminous than an empty universe ($\Omega_m = \Omega_\Lambda = 0$) would suggest. For the case $z \gtrsim 1$ the supernovae are less luminous. Since a value for the mass density was already known from dark matter studies ($\Omega_m \approx 0.3$), the only way to explain this behaviour is to assume an accelerated expansion of the universe, which demands a cosmological constant $\Omega_\Lambda > 0$. The supernova surveys resulted in a cosmological model with $\Omega_m = 0.27$ and $\Omega_\Lambda = 0.71$. The first results of this survey were published in 1998 and up to that point the cosmological constant was believed to be zero.
Another evidence for dark energy comes from the study of the cosmic microwave background radiation, which was incidentally discovered by Penzias & Wilson (1965). During the early stages of development in the Big Bang model, the universe was so hot that every emitted photon was re-absorbed. In the timeframe of 3.8×10^5 y after the Big Bang the universe had cooled down enough so that photons could decouple from the matter. This "afterglow" of the Big Bang can still be observed today in form of the cosmic microwave background radiation, an almost perfect black body spectrum at 2.73 K.
The black body spectrum shows anisotropies on the scale of $\Delta T/T \approx 10^{-3}$. This variation reflects the inhomogeneities of the universe at the time of the decoupling. If there were no inhomogeneities, the universe could not have formed any of the structures we see today. The anisotropies of the CMB have been studied to great accuracy by the WMAP (Wilkinson Microwave Anisotropy Probe) satellite, which

Table 2.1: Select cosmological parameters derived from WMAP for the ΛCDM model (Hinshaw et al., 2008).

Description	Symbol	WMAP
Age of universe	t_0	$13.73 \pm 0.12\,\mathrm{Gyr}$
Hubble constant	H_0	$70.1 \pm 1.3\,\mathrm{km\,s^{-1}\,Mpc^{-1}}$
Baryon density	Ω_b	0.0462 ± 0.0015
Dark matter density	Ω_c	0.233 ± 0.013
Dark energy density	Ω_Λ	0.721 ± 0.015
Total density	Ω_{tot}	1.0052 ± 0.0064

started in 2001. In figure 2.8, the CMB anisotropies and its temperature power spectrum can be seen. The angular scale on which the anisotropies are being observed is a measure for the universes constituents at the decoupling. Below a characteristic angle θ_H the particles could have interacted physically before the decoupling, which is given by the event horizon of the photons. Photon-matter interaction could only have happened below this characteristic angle in form of acoustic waves in the coupled plasma. The position of these *acoustic peaks* can be calculated and fitted to the observed data, by varying cosmological parameters like the density parameters for dark matter, baryonic matter or dark energy (Ω_c, Ω_b, or Ω_Λ respectively).
From the observations of WMAP and other cosmological surveys like the supernova Ia survey, the new standard model of cosmology emerged. It is called the flat Λ cold dark matter (ΛCDM) model, since the total density Ω_{tot} is close to unity and the universe is dominated by the effects of the dark energy density Ω_Λ and secondary by dark matter. Dark and baryonic matter are both only a fraction of the universes constituents and it has to be mentioned, that baryonic matter makes up only 4% of the total universe. The key parameters of this cosmological model can be seen in table 2.1.

2.4.4 Impact of X-Ray Astronomy on Dark Matter Research

X-ray astronomy allows the study of the largests known structure in the universe such as galaxy clusters as well as stellar systems at the end of their life. In both cases, objects at very high distances can be observed which can help to understand the evolution of the universe. Dark matter and dark energy strongly influence the behaviour in both cases. X-ray astronomy adds another method of investigating cosmological parameters to the previous (and ongoing) surveys of the CMB and the supernovae Ia.

Chapter 3

X-Ray Satellites

The X-ray mission Spectrum-Roentgen-Gamma is a new and powerful satellite that is to be launched in 2011. Before giving a summary of the science and instrumentation of the mission, an overview of "historical" X-ray satellite missions and the development of X-ray detection techniques will be given. The *Institut für Astronomie und Astrophsik, Abteilung Astronomie* (IAAT) has participated in satellite collaborations like XMM-Newton, INTEGRAL, ROSAT or Mir-Kvant and conducted a multitude of balloon experiments.

3.1 Successful X-ray missions and their detection systems

3.1.1 Uhuru

Uhuru (or *Small Astronomy Satellite A*) was the first satellite dedicated to the observation of X-rays (Giacconi et al., 1971). It was launched December 12, 1970 from the east coast of Kenya. This day was the seventh anniversary of the Kenyan independence and in recognition of Kenya's hospitality, the satellite was named Uhuru (Swahili for "freedom"). In its three-year survey, galactic and extra-galactic X-ray sources were studied in the range of 2–20 keV with a limiting sensitivity of $5 \times 10^{-4}\,\mathrm{L_{x,crab}}$[1]
The instruments on Uhuru (seen in figure 3.1) were two banks of proportional counters mounted back to back. Two collimators (one on the front side, one on the backside) defined the field of view (FOV) to $5° \times 5°$ and $0.5° \times 5°$ respectively. The proportional counters are gaseous ionisation counters. X-ray photons interacting with the inner shells of atomes produces primary free electrons. Two electrodes now accelerate both the ion and the electron. If the voltage is sufficiently high, the free electrons ionise more atoms along their path. An avalanche is caused which is proportional to the energy of the incident photon and can be measured at the readout anode. Background noise by high-energy photons and particles is filtered out with a pulse-shape discriminator and an anti-coincidence filter. Due to the low

[1] The luminosity of the Crab nebula is frequently used to describe the luminosity of X-ray sources.

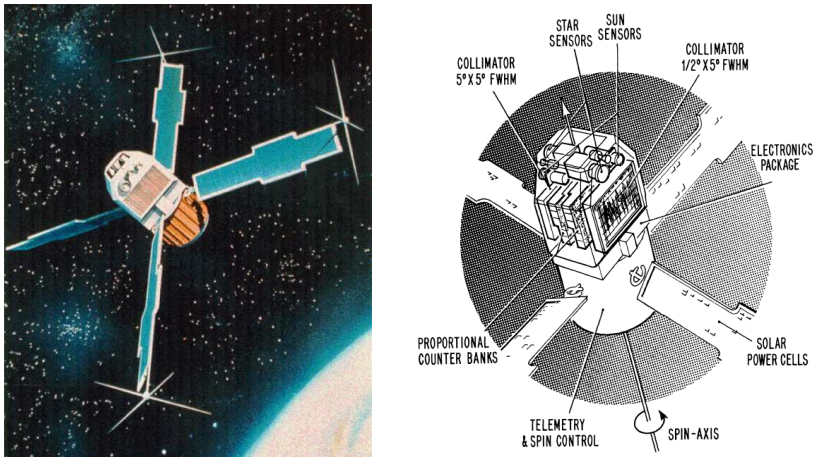

Figure 3.1: An artist impression of UHURU (http://heasarc.gsfc.nasa.gov) and a sketch of the satellite payload (Giacconi et al., 1971).

angular resolution and not optimal energy resolution, these detectors were replaced in later missions with solid-state detectors like semiconductors, which offer a much better energy resolution and the option of creating a pixilated structure for imaging purposes.
Uhuru was the cornerstone satellite for X-ray astronomy. Apart from observing already known X-ray sources like Tychos supernova (SN1573), Cyg X-1 or the Crab nebula, about two hundred new X-ray sources were discovered. The sources discovered and observed by Uhuru can be found in the Uhuru catalogue (Giacconi et al., 1974).

3.1.2 ROSAT

The **Ro**entgen **Sat**ellite (ROSAT) was the first German X-ray satellite with US and British collaboration and it was launched on June 1, 1990 from Cape Canaveral. It was named after Wilhelm Conrad Röntgen, who discovered the X-rays in 1895. The most notably surveys that it carried out in its $8\frac{1}{2}$ years of operations were an all-sky-survey, which revealed about 150 000 new X-ray sources, an extreme ultra-violet survey, which discovered 479 EUV sources, and many pointed observations on X-ray objects.
Its main instrument was the X-ray telescope XRT, which consisted of four nested Wolter-I mirror shells with an energy range of 0.1–2.4 keV. In its focus were either one of two position sensitive proportional counters (PSPC) or a high resolution imager (HRI). While conventional mirrors use a reflector which is positioned in a plane perpendicular to the incoming radiation, Wolter-I mirrors work on the principle of total reflection at small grazing angles. The critical angle when total reflection on a

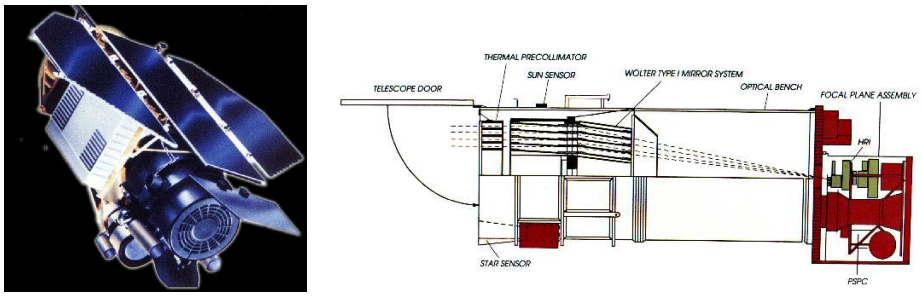

Figure 3.2: An impression of the ROSAT satellite and its Wolter telescope (http://wave.xray.mpe.mpg.de/rosat).

perfect surface will occur can be calculated as (Aschenbach, 1985)

$$\alpha = \lambda \sqrt{\rho \frac{N_0 Z r_e}{\pi A}} \tag{3.1}$$

where λ is the incident wavelength, Z and A atomic number and weight respectively, N_0 Avogadro's number, r_e the electron radius and ρ the mirror density. For X-rays with a wavelength of 0.1 nm the critical angle is of the order $\alpha \approx 1°$. High density coatings on the mirror increase the critical angle, however atomic absorption lines have to be considered (gold for example has an absorption line at 0.56 nm). The incident radiation is first being reflected from the inside of a paraboloid mirror shell onto the inside of a hyperboloid shell, which has a much shorter focus at a comparable aperture. In figure 3.2 the layout of the four telescope shells can be seen. XRT had a total unobscured geometric collecting area of 1141 cm^2 and was sensitive in the area of 0.1–2.4 keV (Truemper, 1982) .
In addition to the XRT, ROSAT had a wide field camera (WFC) installed, which was coaligned with the main telescope. The WFC also applied the Wolter-I optics to focus extreme ultra-violet light (XUV) in the energy range of 0.042–0.21 keV. Two early-type CCDs were used as star trackers.

3.1.3 XMM-Newton

The **X**-ray **M**ultimirror **M**ission - Newton (named in honour of Sir Isaac Newton) was launched on December 10, 1999 and was with a lenght of about 10m the largest scientific satellites ever launched by ESA up to this date. The scientific mission description is High-Throughput X-ray Spectroscopy Mission because XMM-Newton was designed to supply highly accurate spectroscopic data (Jansen et al., 2001).
The main telescope on XMM-Newton consists of three Wolter-I mirror modules with 58 mirrorshells and a total geometric effective area of 1 500 cm^2 per module. In

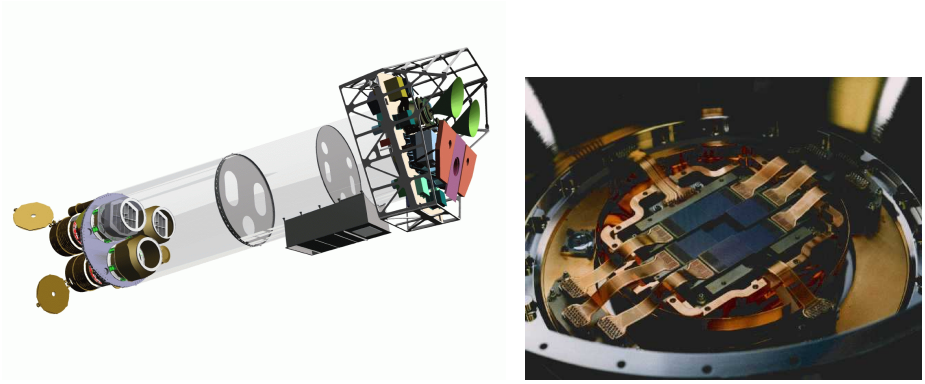

Figure 3.3: A sketch of a "seethrough" XMM-Newton satellite (http://wave.xray.mpe.mpg.de/xmm/) and one of its focal MOS-CCD arrays (http://sci.esa.int).

the focus of the Wolter-I mirrors, CCD arrays are placed – the **E**uropean **P**hoton **I**maging **C**amera (EPIC). In two of the telescope beams, a reflection grating spectrometers (RGS) is placed. The undeflected light is observed by two EPIC arrays of seven MOS-type CCDs (Turner et al., 2001) as shown in figure 3.3. The grated spectrometers disperse the X-rays according to the groove spacing of the grate and the wavelength of the photon and the X-rays are detected with nine large-format CCDs which are placed on the angle of dispersion. With this setup, a spectrum in the soft X-ray range (0.3–2.1 keV) can be taken, which is the energy range of K-shell transitions of a number of heavier atoms like carbon and nitrogen.
The EPIC in the focus of the third (unobstructed) beam, is a $6 \times 6\,\mathrm{cm}^2$ monolithic pn-CCD (Strüder et al., 2001) which is sensitive in the energy region up to 15 keV. This CCD is the predecessor of the framestore pn-CCD used in this thesis. Its basic working principles are explained in the following chapter and its properties are given in table 4.2.

3.1.4 INTEGRAL

The **INTE**rnational **G**amma-**R**ay **A**strophysics **L**aboratory (INTEGRAL) is an ESA satellite in collaboration with NASA and the Russian Space Agency and it was launched on October 17, 2002 from Baikonur. The two main instruments onboard, the spectrometer SPI[2] and the imager IBIS[3] are both sensitive in the energy range from hard X-rays to soft gamma rays. In addition, INTEGRAL carries an X-ray monitor and an optical camera.

[2] **SP**ectrometer for **I**ntegral
[3] **I**mager on-**B**oard the **I**NTEGRAL **S**atellite

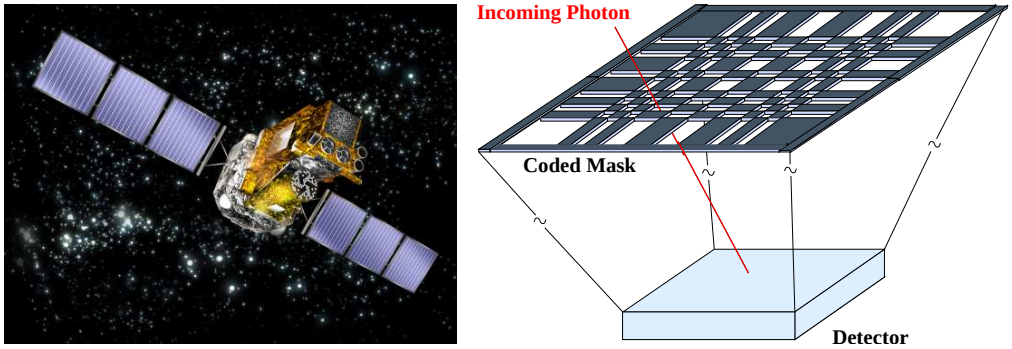

Figure 3.4: An artists impression of the INTEGRAL satellite (http://www.esa.int/esaMI/Integral) and a sketch of a coded mask optic. (Image courtesy of Christoph Tenzer).

The energy ranges of the spectrometer (20 keV–80 MeV), the imager (15 keV–10 MeV) and the X-ray monitor (3–35 keV) are too high to work with an imaging optic like the Wolter-I mirrors. The critical angle for total reflection is dependent on the wavelength and would be too low especially for the gamma-ray instruments. Instead a coded-mask imager is used (in 't Zand, 1996). Coded masks do not focus the incoming radiation, but encode (or multiplex) the incident radiation dependent on the dicrection of the source. The mask consists of a pattern of opaque and transparent elements that is placed in front of the detector as shown in figure 3.4. Each source in the telescope's field of view will cast a unique shadow patter on the detector that has to be reconstructed by correlating the recorded image with the mask pattern. Even though photons of higher energy can be detected with a coded mask the signal-to-noise ratio is far lower than with a focussing instrument. The image is not concentrated on a certain detector area, so background events recorded over the entire detector contribute to the noise.
At higher energies, the photons are less likely to interact with matter and therefore more likely to pass through the satellites sides. To ensure that a gamma photon is originating from the telescopes field of view, the detectors have to be shielded. On IBIS (Ubertini et al., 2000) the detector aperture is passively shielded by a lead layer between mask and detector system. In addition the other sides of the detector are covered with active scintillation detectors, which will veto an event in the case of a coincidential measurement. The detector of IBIS also reflects the broad energy range that is to be detected. It consists of two layers: First a cadmium-zinc-telluride layer for the detection of hard X-rays ($> 15\,\mathrm{keV}$) and second a caesium-iodine layer, with a sensitivity ($\approx 511\,\mathrm{keV}$) in the soft gamma band.
In its almost six years of service, INTEGRAL has supplied a number of results and discoveries like a catalogue of over 400 gamma-sources, detailed observations of X-ray binaries and gamma-ray bursts. INTEGRAL is still fully operational and will continue its surveys at least until the year 2010.

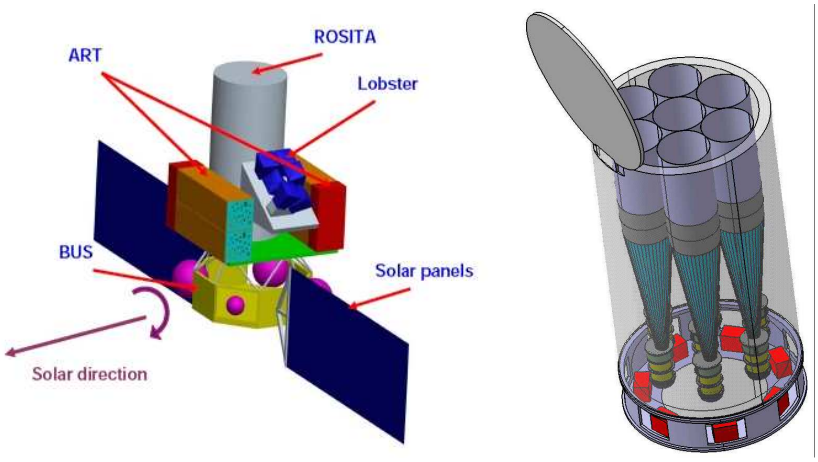

Figure 3.5: An early sketch of the Spectrum-RG satellite and its main telescope eROSITA (Dmitriev et al., 2005). The main instrument consists of seven Wolter-I telescopes with independent pn-CCDs in their focal planes.

3.2 Spectrum-RG

The Spectrum-RG mission is a medium size satellite mission, that will be launched in the timeframe of 2011-2012 from Baikonur. It is a successor of both ROSAT and ABRIXAS[4], since it will conduct an all-sky survey in the X-ray spectrum as well as pointed observations in regions of interest. It is expected that Spectrum-RG will discover several hundered thousand new X-ray sources and give valuable data on the dark energy research by observing distant glalaxy clusters and AGNs. Spectrum-RG is an international collaboration with contributions from Germany, the UK, the Netherlands and Russia (Pavlinsky et al., 2006), (Dmitriev et al., 2005).

3.2.1 Instrumentation

Apart from the main telescope on Spectrum-RG (eROSITA), the instrumentation is still under discussion and might be subject to changes.

eROSITA: **e**xtended **RO**entgen **S**urvey with an **I**maging **T**elescope **A**rray [*Max Planck Institut für extraterrestrische Physik* in collaboration with the universities of Tübingen, Hamburg, Potsdam and Erlangen-Nuremberg, Germany].

[4] **A BR**oadband **I**maging **X**-ray **A**ll-Sky **S**urvey; this mission consisted of 7 Wolter-I telescopes which should provide an all-sky survey at higher energies (0.5–15 keV) than ROSAT. Unfortunately the mission failed shortly after its launch (April 29, 1999) due to an overheating in the power supply.

Table 3.1: Properties of the eROSITA X-ray optics (Predehl et al., 2006)

mirror modules	7	grazing angles	$16' < \alpha < 96'$
mirror shells	54 / Module	wall thickness	0.2-0,9 mm
energy range	0.2–12 keV	microroughness	< 0.5 nm RMS
angular resolution	$< 15''$ on-axis	mirror coating	Gold (> 50 nm)
outer diameter	358 mm	focal length	1600 mm
inner diameter	76 mm	weigth of mirror	57 kg / Module
length of shells	300 mm	material of shell	Nickel

This instrument consits of seven independent Wolter I mirrors with 54 mirrorshells (ABRIXAS had 27 mirrorshells) with a total collecting area of 2 500 cm^2 (effective area: 700 cm^2 at 1 keV). In each of the foci of the Wolter mirrors, there will be a 384×384 pixel framestore pn-CCD with a field of view (FOV) of $41.5' \times 41.5'$ and an energy resolution of 130 eV FWHM at 6 keV. Details on the detector will be given in the following chapter. The optics are designed for an energy range from 0.2–12 keV with an angular resolution of less than $15''$ on axis. Details on the mirror system can be seen in table 3.1. The CCD-camera will yield measurements of unprecedented accuracy.

Lobster: Lobster-eye wide field camera [*Leicester University*, UK]. The lobster camera consists of an array of microchannel plates (6×60 plates). Each of the six plates has a FOV of $27.5° \times 22.5°$ with an energy range of 0.1–4 keV. Energy resolution ($\Delta E/E \approx 20\%$) and angular resolution ($4'$) are low, but due to the large field of view, Lobster is able to cover the entire sky in 96 minutes. This lead to the motto "All the sky, all the time".

ART-XC: Hard X-ray concentrator [*Space Research Institut (IKI)*, Russia]. ART is designed to provide observations in the high-energy range up to 80 keV. The focussing optics originally consisted of capilliary concentrators ("Kumakhov optics" after (Dabagov et al., 1995)) with a fallback on coded-mask optics, both with a cadmium-zinc-tellurite detector. Recently also grazing incidence mirrors have been discussed. The six modules have a field of view of $2.8' \times 2.8'$ at 80 keV with an energy resolution better than 1 keV at 60 keV.

SXC: **S**pectrum-**X** **C**alorimeter [*Netherlands Institut for Space Research (SRON)*]. An array of microcalorimeters with a single Wolter-I telesope identical to the one used for eROSITA. Calorimeters in general use highly temperature sensitive materials like doped semiconductors or superconductors in its phase transition to acquire the energies of incident photons with an energy resolution of the order of 10 eV at 6 keV. The calorimeter will provide highly accurate spectral measurements in the energy range of eROSITA.

Table 3.2: An overview of the eROSITA surveys (Dmitriev et al., 2005)

Survey	All-Sky-Survey	Wide	Deep Survey
Solid Angle [□°]	42 000	20 000	200
Exposure time [yr]	1	2.5	0.5
0.5–2 keV $S_{\mathrm{min,AGN}}$ [cgs]	5.7×10^{-14}	1.5×10^{-14}	4×10^{-15}
2–10 keV $S_{\mathrm{min,AGN}}$ [cgs]	1.0×10^{-12}	2.1×10^{-13}	2.4×10^{-14}
0.5-5 keV $S_{\mathrm{min,Cluster}}$ [cgs]	1.6×10^{-13}	3.3×10^{-14}	8×10^{-15}
0.5-2 keV AGN	240 000	800 000	740 000
2-10 keV AGN	12 600	84 000	44 000
Clusters	32 000	72 000	6 500

3.2.2 Science with eROSITA

Three surveys are planned with eROSITA: first, an all-sky survey will cover the entire X-ray sky within a year and will reveal obscured black holes and galactic X-ray sources. Second, a wide survey at high galactic latitudes which will discover of the order of 10^6 AGNs and 10^5 clusters of galaxies and finally a deep survey at the galactic south pole. A summary of the surveys can be seen in table 3.2. All three surveys also reach a flux limit that is orders of magnitudes better than all previous missions as seen in figure 3.6.
The two main scientific aims for eROSITA are:

The Quest for Dark Energy: Clusters of galaxies are the largest objects in the universe. Their structure and evolution is dependent on their total mass therefore on the amount of dark matter they contain. On the other hand, their spatial distribution and number is dependent on the total amount of dark energy, because dark energy is acting as a negative pressure on the universe. eROSITA will be able to study these objects up to high redshifts ($z < 2$) and can therefore help to further increase the accuracy of the cosmological model by applying another method (next to CMB anisotropies and the study of type Ia supernovae) for the determination of the cosmological parameters (Dmitriev et al., 2005).

The Quest for Obscured Accretion: A second scientific goal for for the Spectrum-RG mission is the detection of active galactic nuclei. As most of the radiation emitted by the AGNs is obscured by dust and gas clouds, these phenomena have to be studied in an energy range that can penetrate these clouds like for example hard X-rays. Previous survey indicated that both star formation and black hole feeding mechanisms were orders of magnitudes higher in the early universe, which is not yet understood.

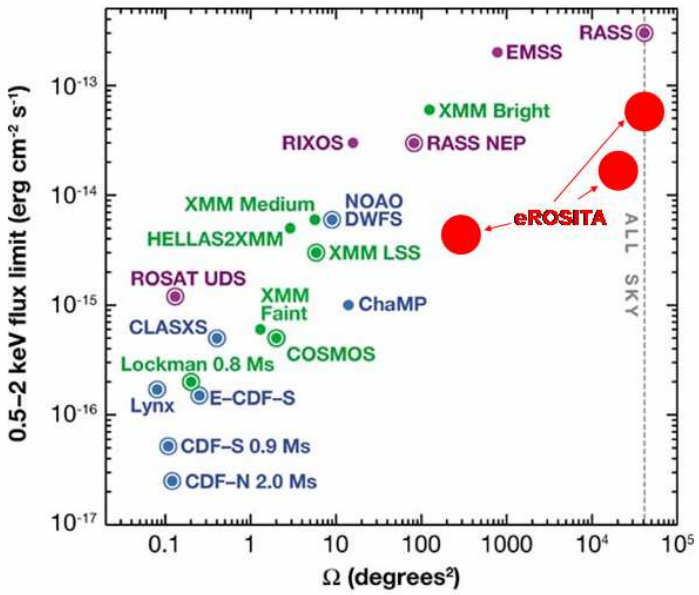

Figure 3.6: Sensitivity and sky coverage of the three eROSITA surveys in comparison to previous surveys (Dmitriev et al., 2005).

Chapter 4

Semiconductor Detectors

In this chapter a brief summary of semiconductor physics will be given, including the different structures that are needed to understand the imaging semiconductor detector called framestore pn-CCD[1]. Its properties and working principles are explained. The general semiconductor physics is based on Lutz (2001) and Spieler (2005).

4.1 Why Semiconductor Devices?

Semiconductor devices owe their success in the field of particle and photon detectors to a number of unique properties. First, the crystal structure of commonly used semiconductors —silicon, germanium or compound semiconductors like gallium arsenide— is a durable diamond (Si and Ge) or a zinc blende (GaAs) lattice. In the case of silicon, monocrystal ingots with a diameter of 30 cm can be grown. The high density of solid-state materials permit the production of small yet sturdy detectors. Second, the electrical properties of high-purity semiconductors can be easily altered via doping. The doped materials can then be used to create a variety of junctions like the "classic" pn-diode or JFETs (see below). Third, the relatively small band gap of semiconductors (1.12 eV in the case of silicon at room temperature) permits the detection of optical photons, giving semiconductor detectors a very broad range of applications. Fourth, semiconductors allow a simultaneous measurement of energy and position using pixelated detectors like the CCD. And finally, the first amplifier can be made out of the same material as the detector itself, allowing an integrated structure on a common substrate.
In addition to the scientific application, the use of CCDs in digital cameras and even cellphones has become almost a mandatory feature. The public demand for smaller, more efficient or even new types of semiconductor cameras is of course a different reason for research, but deserves a mention.

[1] Charged Coupled Device

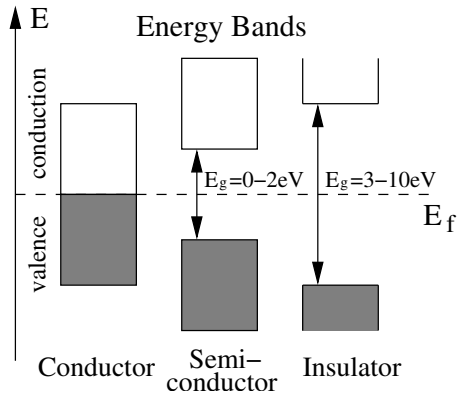

Figure 4.1: Electron bands in solids

4.2 Semiconductor Physics

Conductors, insulators and semiconductors are characterized by the size of their bandgap E_g, as seen in figure 4.1. The bandgap of a solid is the energy needed for an electron in the atomic lattice to cross from a lower band (the valence band) to a higher band of allowed energies (the conduction band). In conductors, those two bands are adjacent or even overlapping. The size of the bandgap is therefore zero. The size of the bandgap in semiconductors and insulators is greater than zero and the size of the gap determines the type of material. For semiconductors the gap ranges from $0 - 2\,\mathrm{eV}$ and for insulators from $3 - 10\,\mathrm{eV}$. Therefore, thermal excitation or optical photons may cause electrons in semiconductors to cross the bandgap into the conduction band[2], while this is not possible in the case of an insulator. A semiconductor might have a small number of electrons occupying the conduction band at room temperature.

The energy bands are a result of the distance in between the atoms in a solid or – in the case of most semiconductors – of the crystal lattice. At great distances, the energy levels are N-fold degenerate (with N being the number of atoms) since the probability of electrons of two atoms interacting becomes neglectable. Once the spacing between the atoms becomes smaller, the quantum-mechanical wave functions of the electrons overlap causing the energy levels to broaden, merge and split at even closer distance. The valence band is now defined as the highest fully occupied energy band in the lattice at 0 K. No conduction can take place in the valence band, since any electron movement in a fully occupied band demands that another electron immediately takes its place, so the electrons will just change places. The conduction band is the next band over the valence band. Charges in the conduction band can move freely and their movement can be influenced by an outer electrical field $\vec{E}$.

[2]The energy of optical photons ranges from 1.7 eV to 3.1 eV.

Table 4.1: Properties of three select semiconductors

Property	**Si**	**Ge**	**GaAs**
Nuclear Charge	14	32	31:33
Density [$\mathrm{kg\,m^{-3}}$]	5.333×10^3	2.3×10^3	5.35×10^3
Atoms [$\mathrm{cm^{-3}}$]	5.0×10^{22}	4.4×10^{22}	4.4×10^{22}
Bandgap [eV]	1.12	0.67	1.43
Charge density n_i [$\mathrm{cm^{-3}}$]	1.02×10^{10}	2.33×10^{10}	2.10×10^{10}
Mean energy for e^--hole formation [eV]	3.63	2.96	4.35
Electron mobility μ_n [$\mathrm{cm^2\,V^{-1}\,s^{-1}}$]	1350	3900	8500
Hole mobility μ_p [$\mathrm{cm^2\,V^{-1}\,s^{-1}}$]	480	1900	450

Any charge carrier lifted into the conduction band will leave an electron hole in the crystal lattice since it can drift away from its former position. The convection density for a number of electrons n and for a number of holes p with corrosponding mobilities μ_n and μ_p is given by:

$$\vec{i}_{\mathrm{drift}} = q(p\mu_p + n\mu_n)\vec{E} \tag{4.1}$$

The mobility of both electrons and holes can be seen in table 4.1[3]. It is important to note, that the mean energy for an electron-hole pair is much larger than the bandgap. Both bands have a certain extension, so electrons can be lifted from and to different energies and the transition can also excite lattice vibrations called *phonons*.

4.2.1 Doped Semiconductors

The properties described in the previous section all apply to high purity or *intrinsic* semiconductors. In these materials conduction can only be caused by thermally generated holes and electrons. Since the purity needed for an intrinsic material is quite high, it is more convenient to alter the semiconductors structure by implanting small amounts of specific impurities. The charge density in semiconductors is relatively low in comparison to the number of atoms (see table 4.1), so even an impurification as small as $1 : 10^{12}$ atoms will influence the charge density as much as the thermally generated electron-hole pairs at room temperature. These impurities can be implanted during the growth of the crystal or later by sputtering selected areas. This process is called *doping*.

There are two kinds of dopands, *donors* and *acceptors*. The most important semiconductors – silicon and germanium – are quatrovalent elements (four electrons in the outmost shell), forming a tetrahedral crystal lattice. An "impurity" with an

[3]The resistivity for example can be calculated via formula 4.1, since $e(p\mu_p + n\mu_n) = \sigma$, the resistivity, which is the inverse of the conductivity. Using the numbers for silicon from above, a resistancy of the order of $10^5\,\Omega$ can be obtained, which is indeed the case for high purity silicon.

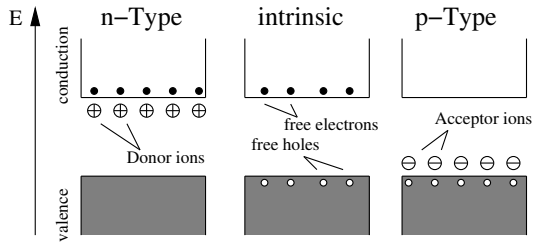

Figure 4.2: The three types of (doped) semiconductors. In this notation, a $+/-$ stands for strong / weak doping.

additional electron in the outer shell (arsenic or phosphorus) will provide an additional electron that is not used for the covalent bonds with the four neighbouring atoms and can easily be transferred into the condution band, leaving a positively charged ion behind. Since negative charges are provided by the dopand, this type of doped semiconductor is called an *n-type* and the donating atoms are called donors. Similarly, an impurity with only three electrons in the outer shell (boron) will lack one electron for the fourth covalent bond. This electron can be accepted from a neighbouring bond[4] and the ions are called acceptors. A negative ion remains but the positively charged hole can move and form a current; these semiconductors are called *p-type*. See figure 4.2 for the three types of doped semiconductors.

4.2.2 Pn-Junctions

One of the most basic elements of semiconductor electronics is the pn-junction. A p-type semiconductor is brought into contact with an n-type semiconductor. Both materials are electrically neutral and free of an electrical field. However, once brought into contact with each other, a charge carrier diffusion will occur, since the free electrons will combine with the free holes in the contact region. The diffusion current for a charge density n or p is given by:

$$\begin{aligned} \vec{i}_n &= +qD_n\nabla n \\ \vec{i}_p &= -qD_p\nabla p \end{aligned} \tag{4.2}$$

The constant of diffusion D is given by the Einstein equation

$$D_{p/n} = \frac{kT}{q}\mu_{p/n} \tag{4.3}$$

The carrier density abruptly changes in the contact region, so free electrons from the n-type will combine with free holes from the p-type until the field that is caused

[4]The ionisation energy for both donors and acceptors are of the order 0.05 eV, so at room temperature the charge carriers can move freely.

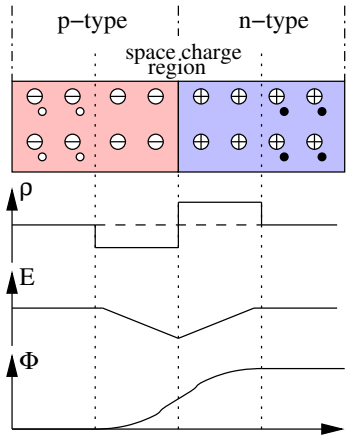

Figure 4.3: Cross section of a p-n junction, including the electric properties.

by the stationary dopand ions is in equilibrium with the diffusion. A so called *space charge region* or *depletion zone* is formed in the proximity of the junction, in which the nuclear charge is not neutralized by the charge carriers any more. The total diffusion density becomes

$$\vec{i}_{tot} = q(p\mu_p + n\mu_n)\vec{E} + q(D_n\nabla n - D_p\nabla p) \tag{4.4}$$

The effects of the pn-junction on charge density, field and potential can also be seen in figure 4.3. The same is true for compound semiconductors with the same dopand but different doping density. These junctions are abbreviated with $n^+ - n$ or $p^+ - p$. Even though there are no electron-hole pairs that can recombine, the different charge densities will cause a diffusion of charges into the area of lower doping.

If an external voltage is applied to the pn-junction, the properties will change as follows. If the voltage is positive with respect to the p-side, electrons are supplied to the n-side and removed from the p-side, effectively decreasing the width of the space charge region up to the point where it is possible for the charges to drift over the depleted zone, causing a current (*forward bias*). A negative voltage will do the opposite: more carriers will recombine, increasing the space charge region and so turning the pn-junction into an insulator (*reverse bias*).

4.2.3 Radiation Effects on pn-Junction

Depletion is the key property of a semiconductor detector. A pn-junction under irradiation with photons can either be hit by a photon in the space charge region or in the remaining neutral region, generating electron hole pairs by either photo or

Compton (for higher energies) effect. While an electron-hole pair in the neutral region has the possibility of recombining with other free charge carriers around it, this cannot happen in the space charge region. First, there are no charge carriers for the recombination and second, the internal field of the pn-junction will separate the two charges (even more when the junction is operated in reverse bias) into the opposite neutral zones causing a so called *photocurrent*. This makes a depleted semiconductor an ideal material for the main body or *bulk* of a semiconductor detector. Figure 4.4 shows the *sideways depletion* of a silicon wafer. The whole backside of the wafer[5] is covered with a p-doped cathode, and the frontside with the necessary structures for pixel generation and readout. In addition a n-doped anode is implanted into the "side" of the front. When a sufficiantly high positive voltage is applied to the anode, the wafer can be fully depleted and therefore be photosensitive. These detectors are called *backside illuminated*in contrast to *frontside illuminated* detectors where the incident radiation can be partially absorbed by the structures.
The mean value N for the number of created electron-hole pairs however is not constant for photons of equal energy. This number varies by

$$\langle \Delta N^2 \rangle = F \cdot N = F \frac{E}{\epsilon} \tag{4.5}$$

where E is the energy deposited in the detector, ϵ the mean energy for electron-hole creation and F the Fano-factor[6], which is constant for each material ($F_{Si} = 0.115$). For a Fano factor of $F = 1$, this would be equivalnet to a Poisson statistics. Since the generated charges can influence each other, the electron-hole pair generation is not purely statistical.
Backside illuminated, sideways depleted semiconductors provide the bulk of most modern detectors. The generation of the pixilated structure and the readout electronics however differ greatly and shall be addressed in the following chapters.

4.2.4 Metal-Oxide-Semiconductor (MOS) Junctions

Apart from the pn-junction, the second most important structure for semiconductor detectors is a metal-insulator-semicondutor junction, commonly referred to as a MOS (metal-oxide-semiconductor), since the most frequently used insulator is silicon-dioxide (SiO_2). This insulating layer separates a doped semiconductor (in the example in figure 4.5 an n-doped substrate) from a conducting (metallic) contact. Without an external field, the MOS junction is in the so-called *flat band* condition: since both metal and semiconductor are insulated, no charge transfer may occur, the charge density is uniform and hence the field is zero in the whole MOS. A characteristic voltage can be introduced as a difference between the vacuum- and Fermi-levels.

[5] Usually $300 - 500\,\mu$m thick
[6] Measure of the dispersion of a probability distribution. Named after the italo-american physicist Ugo Fano (1912-2001).

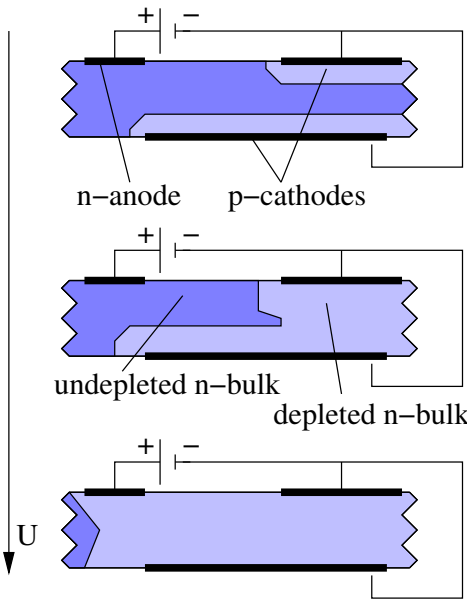

Figure 4.4: Formation of a fully, sideways depleted semiconductor, which is the bulk of most semiconductor detectors.

For a flat band MOS, the vacuum level is uniform throughout the junction (hence the name), so it is given by

$$U_{FB} = \Phi_M - \Phi_S \tag{4.6}$$

If a negative voltage with regard to the semiconductor is applied to a n-doped MOS, the field will draw additional electrons towards the insulating layer on the semiconductor side and holes towards the metal side. Charges are *accumulated* so an electric field forms within the oxide. The build-up potential increases the voltage across the junction, so that $U_{ACC} > U_{FB}$. On the other hand, a positive voltage will *deplete* the semiconductor layer, as seen in the previous chapter and decrease the voltage so that $U_{DEP} < U_{FB}$. This state is stable, if the field is weak enough to permit the recombination of thermally generated electron-hole pairs. If the field is further increased, thermally generated electron-hole pairs will not be able to recombine again. The electrons will be drawn towards the anode and the holes towards the oxide, forming an *inversion* layer of positive charges.
In this state, the MOS can be used for detection purposes, since electron-hole pairs generated by incident radiation will be separated. The electrons will drift towards the anode, whereas the holes will gather at the semiconductor-oxide boundary. The radiation can be measured either by the change of the field caused by the additional charges or the generated charges can be moved sideways towards a readout electrode.

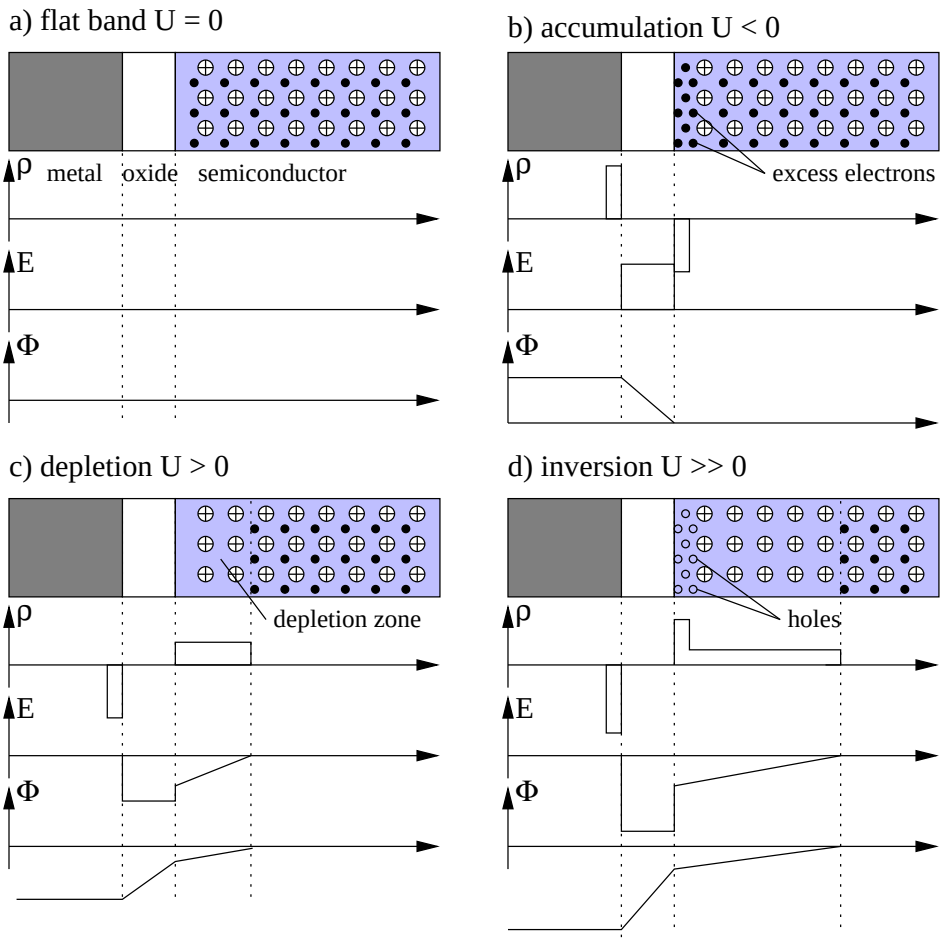

Figure 4.5: Cross-section of a n-type MOS junction. The height and polarity of the voltage applied to the junction can create the four different sets seen in a)-d).

4.2.5 Field Effect Transistors (FET)

There are two basic layouts for a Field Effect Transistor (FET), the junction structure (JFET) and the metal-oxide-semiconductor structure (MOSFET). The latter is the most commonly used FET and the basis for microprocessors and high-speed semiconductor detectors including the DEPMOSFET detector matrices. However, JFETs offer a better noise performance at lower frequencies and are for example used as amplifiers on the pn-CCD. Therefore, the FET principles will here be explained by means of the JFET.
An n-channel JFET consists of an n-doped body with n^+-doped contacts for *source* and *drain* as well as p^+-doped *gate* electrodes[7]. In operation, a positive voltage V_{ds}

[7]The convention for bipolar transistors is usually *emitter*, *base* and *collector*.

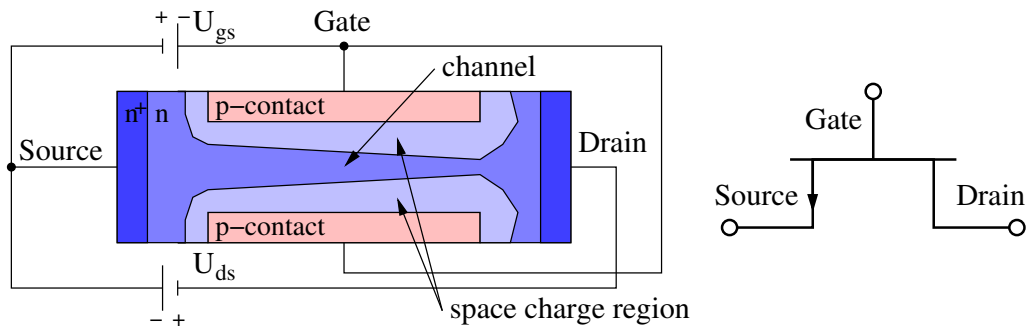

Figure 4.6: The physical setup of a JFET junction and its circuit diagram.

is applied to the drain and a negative voltage to the gate U_{gs} both with respect to the source. The pn-junction between gate and body is now operated in reverse bias, so a space charge region will form in the body. The shape of the channel and therefore the behaviour of the junction depends on the gate and drain voltages.
For low drain voltages, the channel depth will be almost constant over the junction. Therefore, it will act like an ohmic resistor, since the current across the junction is proportional to channel depth (and therefore U_{gs}) and drain voltage. This is called the *linear region* in the current-voltage characteristic and the relation for a JFET with channel depth d, channel length L, channel width W, doping conentration N and electron mobility μ_e is given by:

$$I_{ds} = 2d\frac{W}{L}eN\mu_e U_{ds} \tag{4.7}$$

For higher values of U_{ds}, the form of the channel will not be uniform anymore. Electrons will be drawn to the positive drain and be repelled from the negative source (this intermediate state is shown in figure 4.6). Once the drain voltage becomes high enough to fully deplete the channel, which will occur at the characteristic voltage $U_{ds} = U_p$, the junction is said to be "pinched-off". A current flow is still possible across the pinched-off channel, since the carriers follow the potential drop from source to drain. Now the junction operates in *saturation*, because the current is only weakly dependent of the drain voltage and therefore the junction acts like a current source. This regime also offers the highest voltage gain, which makes it useful for amplification purposes.

4.3 pn-CCD Detectors

The buried channel framestore pn-CCD used for this thesis has been conceived and fabricated by the Halbleiterlabor of the MPE (*Max Planck Institut für extraterrestrische Physik*, Garching). All cited values for the pn-CCD have been taken from (Meidinger et al., 2003, 2004a,b, 2006).

4.3.1 Pixel formation

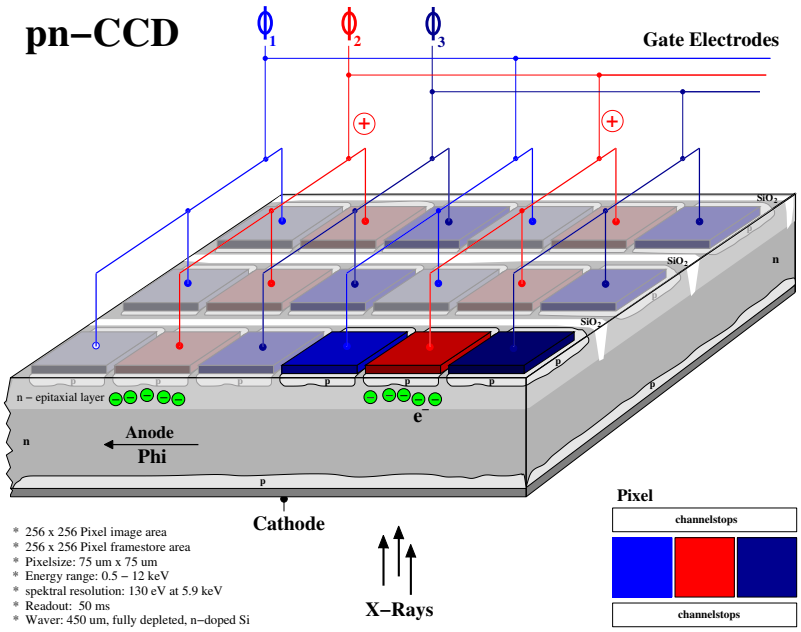

Figure 4.7: The pixel structure and working principal of a pn-CCD (Schanz, 2007).

The bulk of a the pn-CCD is made of 450 μm thick ultra pure n^--type silicon with a thin p-implanted layer on the back side (*back contact*), an 8 μm thick n^+ doped epitaxal layer on the front side and p-implanted registers (also called *phi-registers*) on top of the epitaxal layer. The CCD is a so-called *3-phase* CCD, which means that a single pixel consists of three transfer registers. Thus, three pn-junctions are created, the first between the p-type registers and the n^+-type layer, the second between the n^+-type layer and the n^--type bulk and the third between the n^--type bulk and the p-type back contact.
By applying a high negative voltage to the p-type back contact with respect to the bulk and thus operating the bottom pn-junction in *reverse bias*, the CCD can be fully depleted. Electron-hole pairs generated by incident radiation will now be

immediately seperated, the holes drift towards the back contact and the electrons towards the epitaxal layer, since the higher concentration of donors will create a higher potential in the n-type layer. The depth of the potential maximum can now be influenced by applying two different negative voltages to the three transfer registers. By setting two of the phi registers to the lower voltage Φ_{low} and one to the higher voltage Φ_{high}, a potential well within the epitaxal layer can be created in which the electrons are trapped (see figure 4.7).
The pixels of a column are not separated from each other, the pixels of a row however are separated by SiO_2 implantations (called *channelstops*), which prevent a charge movement in the lateral direction within the epitaxal layer. Thus, a pixel consists of three registers and its adjacent channelstops and has a size of $75\,\mu\text{m} \times 75\,\mu\text{m}$. The tested module (C11_12_45) has 256×256 pixel[8], so the side lenght of the CCD is 19.2 mm.
The pn-CCD has a quantum efficiency of over 90% in the energy region of $0.3 - 11\,\text{keV}$. The mean energy for the generation of an electron-hole pair in silicon is 3.63 eV, so a 11 keV photon will create roughly 3 000 electron-hole pairs. With sensible values of the phi-voltages, each pixel can store more than 10^5 electrons (see table 4.2).
In addition, the *buried channel* feature (which already existed for the MOS-CCDs) permits that the generated charges are not accumulated at the surface of the bulk but $7\,\mu\text{m}$ within the epitaxal layer. Thus, interactions of the charges with lattice defects, which are usually abundant at the surface of the wafer (Lutz, 2001), can be avoided and a higher transfer efficiency and transfer speed can be reached.
Prior to the pn-CCD, the pixilated structure of CCDs was mostly generated by implanting MOS structures onto the bulk instead of pn-contacts. The advantage of the pn-CCD over the MOS-CCD are:

- Full depletion of the bulk. Unlike MOS-CCDs, the pn-CCD can be fully depleted, so that the whole bulk is photosensitive. This feature is particularly important when high energy photons are to be observed, since the absorbtion coefficient (and thus the penetration depth) is energy dependant.

- An uniform response of the chip with backside illumination, because the back contact as well as the depleted area are featureless.

- With a buried channel CCD higher transfer speeds can be reached, since charge collection and transfer happen within the bulk and not at the surface.

- A higher transfer speed also allows the constuction of larger CCD structures.

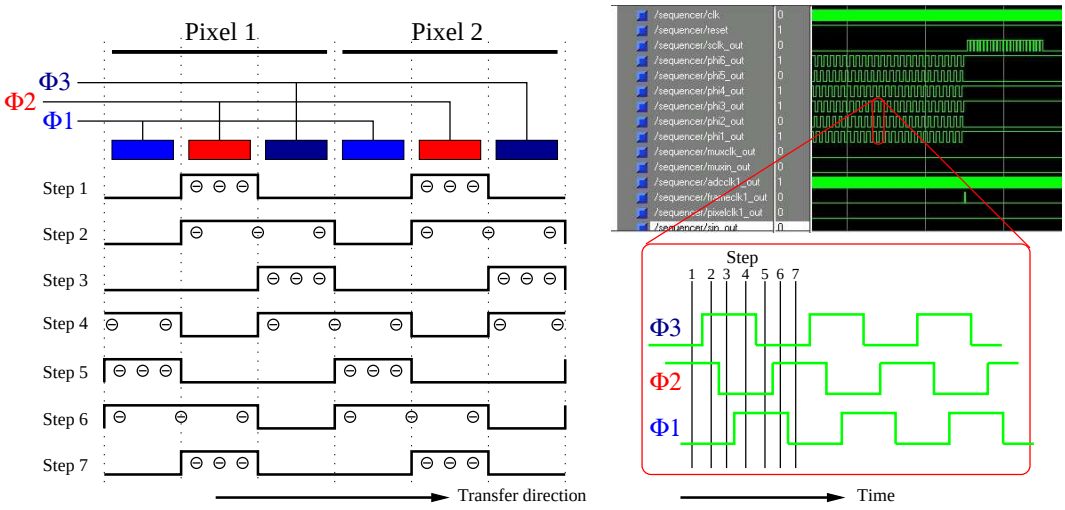

Figure 4.8: Charge transfer in a 3-phase CCD. The logic signals given by the sequencer are shown (right) and their impact on the collected charges (left).

4.3.2 Transfer mechanism

Once the charges from a photon are collected in the potential minimum beneath a register, they have to be moved towards the readout anode. A transfer can be achieved by varying the voltages that are applied to the phi-registers, which form a pixel. In figure 4.8, the transfer for a 3-phase CCD is shown:

Step 1: The middle register is on Φ_{High}, the others on Φ_{Low}, charges can be collected under the middle register as described above. This setup is also typically used for the integration, the time between the readout cycles.

Step 2: The second and third register are set to Φ_{High}, the first remains on Φ_{Low}, so that the charges can drift under the third register as well.

Step 3: Only the third register is set to Φ_{High}, the charges that were still under the second will be collected under the third.

Step 4: The first and the third register are set to Φ_{High}, the charges can drift into the first register of the next pixel.

Step 5,6: The charges are further transported.

Step 7: The original configuration is reached again, but the charges have traveled a whole pixel.

[8] The eROSITA flight modules will have 384×384 pixel.

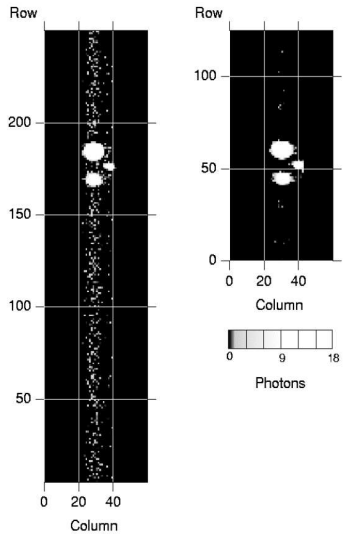

Figure 4.9: Out-of-time events and the effect of a framestore area. On the left, three bright sources are observed in *full frame* mode and a trace of out of time events is clearly visible. When operated in *frame store* mode, the number is greatly reduced (Meidinger et al., 2003).

A full transfer of 256 rows can be completed in 75 μs. Both Φ voltages are generated by an external power supply, the sequence in which they are applied to the registers are governed by the *sequencer*. Both of which will be described in chapter 5.

4.3.3 Framestore Mechanisms

The total speed of the electronic readout of the CCD does not only depend on the charge transfer speed within the CCD, but also on the time that the amplification and readout electronics need to process the charges into a usable signal. While 256 pixel can be transferred within 75 μs, the readout electronics require 5 ms to process the 256 pixel into a digitisable signal.
Therefore, in a regular CCD, the overall transfer speed is determined by the speed of the readout electronics. Since the CCD does not have a shutter, which protects it from incident photons during the transfer and readout, an event can occur during the transfer. This event will have a displacement to its original location given by the fraction of the readout sequence when the event occured. These events are called *out-of-time events* (OOT) (see figure 4.9).
In order to reduce the amount of OOT-events a so called *frame store area* was added to the CCD. This area has the same number of pixels as the *image area* and is shielded from radiation. A whole CCD frame can now be transported into the frame store area with the fast transfer speed. After the fast transfer is completed, the slow readout will begin not directly from the image but from the frame store area. At the start of the readout, the image area can already begin an integration for the next frame. Thus, the probability of out-of-time events can be minimized. In comparison to the XMM-CCD, the frame store pn-CCD has a factor 30 less out-

of-time events (see table 4.2). The pixels in the framestore area can be physically smaller than the imaging pixels, if they are still able to store the generated charge cloud. In case of the eROSITA pn-CCD a framestore pixel is $51\,\mu\text{m} \times 75\,\mu\text{m}$ compared to the $75\,\mu\text{m} \times 75\,\mu\text{m}$ of the imaging area.

4.3.4 CAMEX

CAMEX stands for **C**MOS **A**mplifier and **M**ultipl**EX**er chip and it has been developed by the *Werner-Heisenberg-Institut für Physik* and the *Fraunhofer Institut für Mikroelektronsiche Schaltungen*. It is an integrated analog amplification chip, which can amplify and filter 128 signals of a CCD row simultaeously and then multiplex each processed signal on a common output driver. In figure 4.10, one of the 128 amplification channels is shown. The overall charge generated in the CCD is low[9], so before passing the bondwires that connect the CCD with the CAMEX, the signal has to be pre-amplified.
This is being achieved by a JFET (also called "First-FET"), which is implanted onto the CCD itself and linearly operated. The gate of the JFET is connected to the CCDs anode and it is operated with a constant current between source and drain $I_{DS} = \text{const}$. Afterwards the signal is transferred to the CAMEX. Alternatively to the first-FET, a test-signal can be applied to the CAMEX. Details on the test-input and the operation of the CAMEX during a readout cycle will be given in section 5.3. The different parts of a CAMEX channel are:

Current Source – generates the constant current which is needed for the first-FET. It is realised by a JFET in saturation and it can be switched into a standby mode to reduce power consumption and heat dissipation. The power dissipation of the CAMEX is 5 mW per channel for a readout speed of 6 MPixel/s and 0.2 mW in standby (Meidinger et al., 2004a).

JFET-amplifier – further amplifies the signal voltage from first FET and current source. Two capacitors within the amplifier allow a modulation of the gain by factors of 1, 1/5, 1/32 and 1/160 for a minimum signal input of 20 keV (with maximum gain) to the highest of 3 MeV (with minimal gain). This spectrum of different amplifications makes the CAMEX a versatile amplifier since it can also be used in nuclear physics experiments. For the current experiment however, the highest gain (and energy resolution) can be used.

CDS Filter – further amplifies the signal and filters the signal noise. With eight dynamic switches the signal can be sampled and integrated. Before the signal is available at the first FET, the CCD is connected to the CAMEX, so that the basic noise and signal level of the CCD can be sampled eightfold and

[9] On the order of 100–3 000 electrons in the eROSITA energy range.

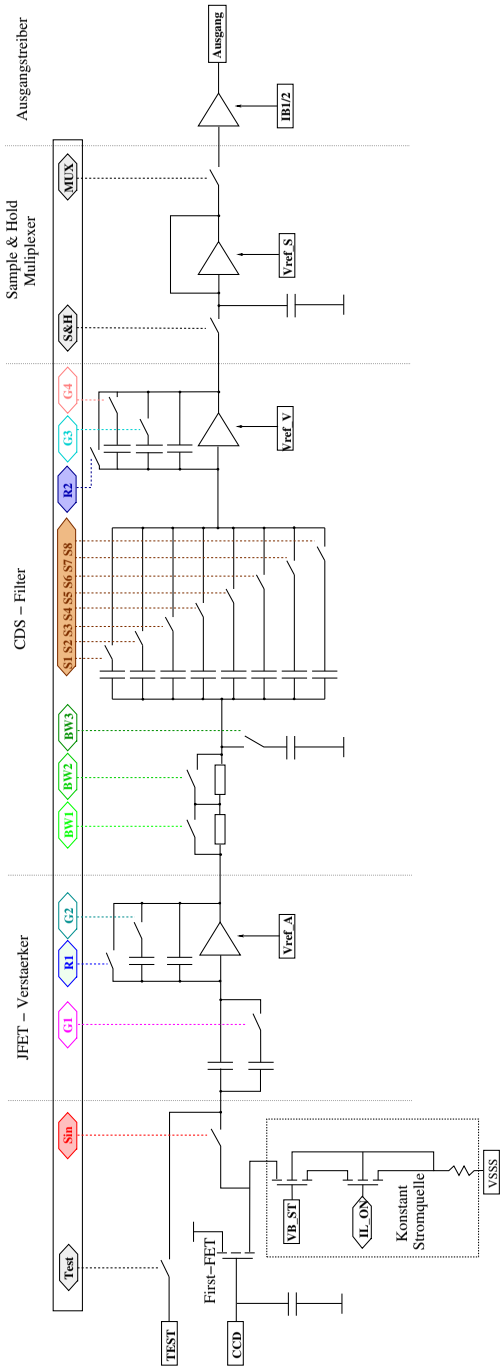

Figure 4.10: Schematic diagram of a single channel of the 128-CAMEX, including the on-chip first-FET.

Table 4.2: Properties of an 256 × 256 pixel framestore pn-CCD and the XMM pn-CCD (Meidinger et al., 2006).

Parameter	**frame store pn-CCD**	**XMM pn-CCD**
pixel size	$75 \times 75\,\mu$m	$150 \times 150\,\mu$m
sensitive depletion depth	$450\,\mu$m	$300\,\mu$m
readout noise	$2\,e^-$ ENC	$5\,e^-$ ENC
quantum efficiency	$\geq 90\%[0.3 - 11\,\text{keV}]$	$\geq 90\%[0.3 - 11\,\text{keV}]$
charge handling capacity	$> 10^5$ electrons / pixel	$> 10^5$ electrons / pixel
CTI (6 keV)	1×10^{-5} / transfer	50×10^{-5}
energy resolution	FWHM(227 eV)=48 eV	-
(20 images/s, T=−60 °C)	FWHM(5.9 keV)=125 eV	FWHM(5.9 keV)=140 eV
readout time	$20\,\mu$s/row (256 pixel)	$23\,\mu$s/row (64 pixel)
readout rate	13 Mpix s^{-1}	2.8 Mpix s^{-1}
frame rate	20/s	14/s
operating mode	frame store	full frame
fast transfer	$100\,\mu s/4cm^2$	n.a.
out-of-time events	0.2% (frame store mode)	6% (full frame mode)
power diss. (focal plane)	$0.3\,\text{W}/4\,\text{cm}^2$	$0.7\,\text{W}/36\,\text{cm}^2$
power diss. / pixel rate	$0.23\,\mu$J / pixel readout	$0.33\,\mu$J / pixel readout

integrated by closing the switches and submitting the resulting signal to the integration amplifier (*baseline sampling*). The preamplifiers are reset and when the signal is available at the first FET, the CCD is connected to the CAMEX and the signal is again sampled eightfold (*signal sampling*). The signal and the baseline are subtracted to produce the final output signal. The CDS filter reduces the signal noise, because the eight samples produce a mean of the sampled signal. The signals bandwidth can be influenced by a bandpass filter. Different capacitors in the feedback loop can be applied.

Sample & Hold – stores the sampled signal. An analog memory for the signal, until it is multiplexed onto the output driver

Serializer – multiplexes the signal onto the output driver. The 128 output signals per CAMEX have to be multiplexed on the driver which is realised by closing the multiplexer switch for the first channel and subsequentially shifting the switch through the channels by means of a multiplexer signal from the sequencer. Each CAMEX has its own physical output driver, so the signal for a full line has to be assembled by the data preprocessing devices.

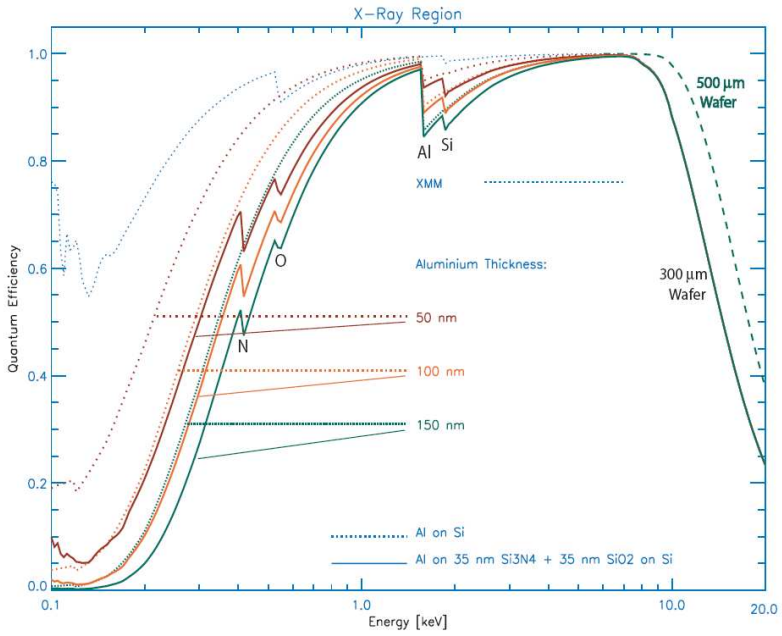

Figure 4.11: Quantum efficiency of the frame store pn-CCD, in terms of a different thickness of the aluminium coating (50 nm, 100 nm and 150 nm). For comparison, the efficiency of the unfiltered XMM-Newton CCD is plotted as well as the gain in high-energy quantum efficiency (> 7 keV) for a thicker wafer (500 μm instead of 300 μm), (Meidinger et al., 2004b).

4.3.5 Properties of the pn-CCD and its signal

There is a great number of properties of the CCDs signals that need to be taken into account in order to either correct systematic effects or apply the appropriate software options.

Quantum Efficiency – The probability of a photon interaction with the detector material. For complex cameras, the quantum efficiency is usually given by the sum of all factors that may prohibit an interaction, including intrinsical properties of the detector material as well as externally applied shieldings. The quantum efficiency of the pn-CCD can be seen in figure 4.11.

Energy pile-up – Two or more photons are collected in the same pixel during a single readout cycle. The two energies become indistinguishable, unless a monochromatic source is observed. In this case, peaks at multitudes of the main peak should be observed

Split-events – More than one pixel is hit by the electron cloud of an incident photon. For this CCD and the observed energy range, the only possible split events are *singles* (one pixel is hit), *doubles* (two neighbouring pixels are hit), *triples* and *quadruples*. Not all neighbouring events are split events though, because similar patterns can be produced by multiple photons. These events can be filtered by defining valid patterns (split events) and invalid patterns. Then, the energy of the photons from the valid events can be deduced by adding the energy of each split partner pixel. Without a split detection and reduction, a characteristic spectrum will be seen between main peak and the noise peak (coined *bathtub*, due to its shape). The probability of a split event occuring is antiproportional to the pixelsize, whereas the XMM-Newton CCD (pixelsize: $(150\,\mu\mathrm{m})^2$) had a split distribution of $70\%_{\mathrm{singles}} : 28\%_{\mathrm{doubles}}$, the framestore pn-CCD (pixelsize: $(75\,\mu\mathrm{m})^2$) has $57\%_{\mathrm{singles}} : 37\%_{\mathrm{doubles}}$ (Meidinger et al. (2003)).

Charge Transfer Efficiency – The charge transfer efficiency (CTE) is the fraction of the energy of an electron cloud, that is transported from one pixel (i) to the next (i+1) CTE $= \frac{E_{i+1}}{E_i}$. Similarly, the charge transfer inefficiency (CTI) is the energy lost after a single shift. Transport losses are the result of lattice defects and impurities in the crystal lattice. Atomic vacancies, additional "interstitial" atoms between the lattice sites, complexes of additional atoms, line defects (a single missing line) or "cluster defects" (high concentrations of single defects) may all inhibits the electron transfer. The CTI for the framestore pn-CCD is 10^{-5} @ 6 keV.

Offset – The readout electronics will generate a constant signal, even though no photon has been detected. This is caused by the first-FET and the amplifiers within the CAMEX, because when no photon is detected, the operational voltages are still applied and thus a constant signal is caused. The correlated

double sampling however eliminates most of the offset that is caused before the CDS filter, which is due to the fact that the (offset) signal is integrated and then subtracted again. The amplifiers after the CDS and the analog-digital-converter (ADC), which digitalised the analog signal, contribute to the offset, too.

Gain – Due to slight differences in the manufacturing of each amplification channel, each CAMEX row has not only a different offset, but also a slightly different ($\approx 1 - 3\%$) signal amplification called *gain*.

Noise – Thermally generated electron-hole pairs, faults in the semiconductor structures, thermally differing current-voltage characteristics and many other effects lead to a time dependent variation of the signal. The noise for semiconductor detectors is commonly measured in *equivalent noise charges* (ENC), which is the noise equivalent given in terms of electrons generated in the detector.

Common Mode – Since all the signal of a single CCD row are amplified and filtered simultaneously, a slight variation in the supply voltages of the amplifiers can cause an additive offset to each row. This is referred to as *common mode*.

Energy Resolution – After all corrections have been applied to a signal of a monochromatic source, the full width at half maximum ($FWHM$) is a measure for the quality of the detector and the readout electronics. The FWHM for the pn-CCD is 125 eV @ 5.9 keV.

Chapter 5

Experimental Setup and Data Analysis

In this chapter, the experimental setup is discussed. The vacuum chamber used for the eROSITA framestore pn-CCD (henceforth referred to as CCD) is the same as the chamber used by Burger (2005) for the DUO[1] framestore pn-CCD, however a new data acquisition rack has been integrated. In addition the data analysis with the FITS-Pipe and the components for optical illumination of the CCD are described.

5.1 Vacuum-Chamber

The performance of semiconductor devices are highly dependent on their temperature. Electron-hole pairs can be created by thermal excitation, which will be captured by the CCD like a pair generated by incident photons. This is of course an unwanted effect for high-precision measurements as the electron-hole pairs contribute to the overall background noise of the detector. For this reason the CCD on board eROSITA will be operated in the temperature range between -60°C and -80°C. Even a change in this temperature region will affect the measurement which will be shown in section 6.3. Therefore the CCD has to be operated not only in a low, but also a stable temperature environment.

5.1.1 Vacuum and Cooling

Under regular atmospheric condition, the humidity in the air would immediately precipitate on the CCD in form of ice if it were cooled to the temperature range mentioned above. To prevent condensation, the CCD is therefore operated in an evacuated chamber. Two vacuum pumps, a diphragm pump for a pressure down to 10^{-1} mbar and a turbo-molecular pump, evacuate the chamber down to a pressure of the order of 10^{-7} mbar. To monitor the pressure inside the chamber, two pressure gauges are mounted on the backside flange. The pressure down to 10^{-4} mbar can

[1] **D**ark **U**niverse **O**bservatory, a planned X-ray satellite which was not realised, but was supposed to use the same CCD-type as eROSITA.

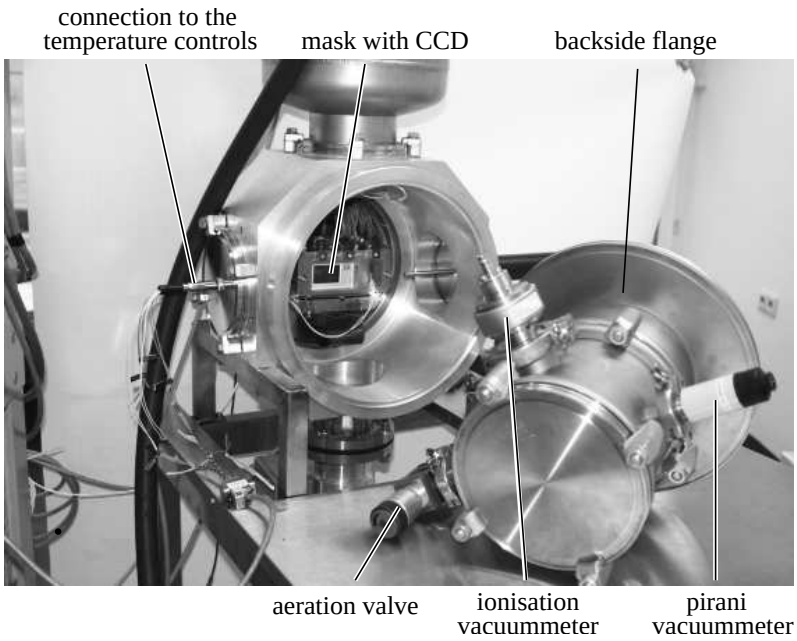

Figure 5.1: The open vacuum chamber.

be monitored with a Pirani vacuum-meter[2]. Below this pressure, a cold cathode pressure gauge can be used[3]. The open vacuum chamber is shown in figure 5.1.
Once a pressure of 10^{-6} mbar is reached within the chamber, the CCD can be cooled. The cooling system consists of a liquid nitrogen[4] cryostat cooling system on top of the chamber. Nitrogen is being pumped into the cryostat from a dewar storage flask. A copper "cold-finger" in the cryostat is being cooled down, which reaches into the chamber where it is connected to a two-piece copper mask via eight copper cords. The CCD resides between the two pieces of the cooling-mask mounted on the inner board.
To influence the temperature-gradient from the cryostat to the CCD, two heating resistors are attached to the cooling system. A $48\,\Omega$ resistor is attached to the cold-finger itself, a heating film is attached to the cooling-mask. The temperature of the CCD can be monitored with an on-chip temperature diode, which can be read out on the outer board. The temperature-voltage characteristics is shown in figure 5.2. In addition two PT100 resistance thermometers[5] are attached to the cold-finger and the front side of the mask as an option for redundant temperature measurement.

[2]Measurement by the coefficient of heat dissipation
[3]Measurement by accelerated ionised gas particles
[4]Nitrogen has a boiling point of $-195.8\,^{\circ}$C.
[5]Resistors change their resistivity in relation to the temperature. PT100 derive their name from the fact that they have a positive temperature coefficient and that their resistivity is $100\,\Omega$ at $0\,^{\circ}$C.

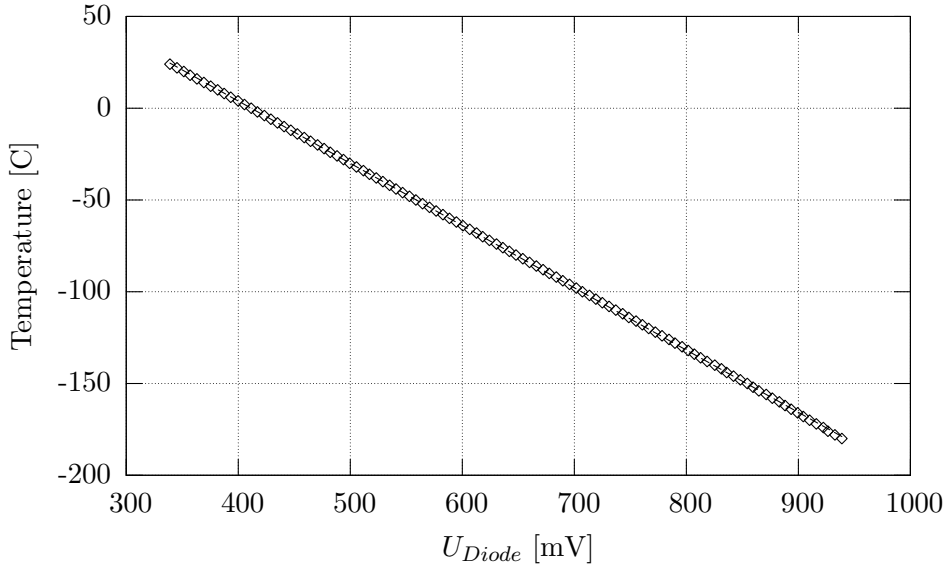

Figure 5.2: Voltage-characteristics of the on-chip temperature diode. The voltage changes by $\approx 3\text{mV}/^{\circ}\text{C}$ [Christian Reich, HLL, priv.com.]

Once the experiment is concluded the chamber can be aerated after the CCD has reached room temperature. Aerating in a cooled state will cause the precipitation described above. Furthermore an aeration with regular air will blow dust particles into the chamber and possibly onto the CCD. For this reason the chamber is aerated with nitrogen gas until atmospheric pressure is reached. In addition, the nitrogen fills the pores in the metal before other molecules like water are able to, which would impede further evacuation.

5.1.2 Inner and Outer Board

The inner and outer board are the electronic connection between the atmospheric side of the chamber and the vacuum side with the detector. Both boards have been designed and manufactured by the *MPI Halbleiterlabor* (HLL) and the *Max-Planck-Institut für extraterrestrische Physik* (MPE), Garching. The inner board is placed inside the vacuum chamber with the CCD inserted in a zero-force socket. Inner board and outer board are connected by flex leads through the front vacuum flange. The outer board is the communication node with the command and readout electronics. A sketch of the connectors and bridges is shown in appendix A. To operate the CCD, the outer board requires the following signals:

- Operating voltages for CAMEX, CCD and for inner/outer board (two 37-pol D-SUB connectors)

- The back contact high voltage input for depletion (bipolar shielded connector)
- The digital driver input signal from the sequencer (68-pol SCSI connector)
- The seperate CAMEX supply voltages `Vddd` and `Vssd` (two unipolar shielded connectors)
- A test pulse input to apply a signal to the CAMEX with disconnected CCD (unipolar shielded connector)
- The sampling timing output signal to the analog-digital converter (RJ45 connector)
- A single ended analog output signal for each CAMEX (two unipolar shielded connectors)
- A differential analog output signal for each CAMEX (two bipolar shielded connectors)
- A trigger output for an oscilloscope (unipolar shielded connector)

In addition, the outer board contains six potentiometers to adjust the CAMEX supply currents `I_REF_A`, `I_REF_S`, `I_REF_V`, `IB1` and `IB2` and the CAMEX-ground `GNDt`. The applied voltages and currents can be measured over the bridges on the outer board (`BRxx`, where `xx` is the number of the bridge), the digital driver signals and the on-chip temperature diode can be monitored on their respective multi-pin connectors.

5.2 Data Acquisition Rack

The 19 inch data acquisition (DAQ) rack shown in figure 5.3 contains the active electronic components for the CCD's operation mounted on double-euro boards. The rack receives its power from an external 28 V power supply. Apart from the sequencer, all boards have been manufactured by the *Max-Planck Institut für extraterrestrische Physik*, Garching. The boards are connected to each other via the backplane, over which the supply voltages and a command bus in the SPI-standard[6] are transmitted. The general setup of the experiment with the DAQ-rack can be seen in figure 5.4. The CCD in the vacuum chamber is connected to the readout electronics via inner and outer board, the DAQ rack supplies power and the driver signals. The analog signal from the CCD is digitalised and preprocessed. The boards in the rack are controlled by a PC which also performs the data-readout. Optionally an oscilloscope or a logic analyser can be connected to the outer board to monitor the analog output signals or the digital driver signals.
The DAQ rack contains:

[6] **S**erial **P**eripheral **I**nterface bus, a synchronous serial data link standard.

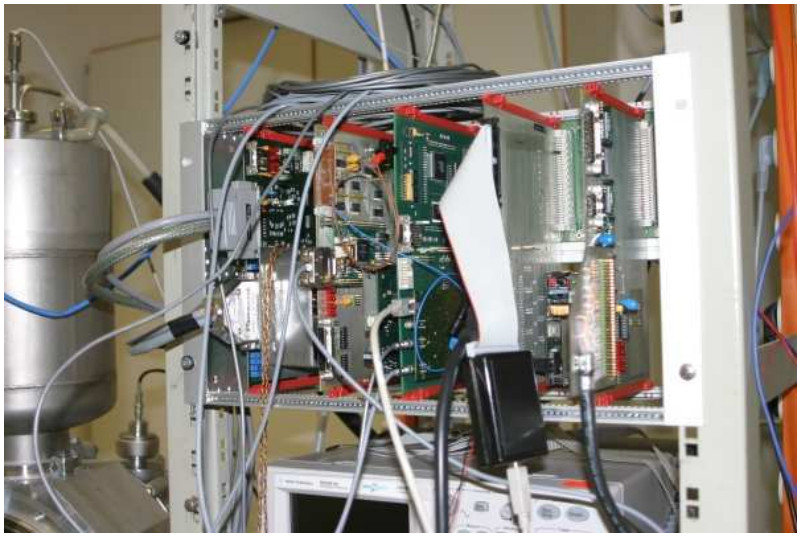

Figure 5.3: The data acquisition rack. The cards from left to right: power supply, housekeeping, ADC and DSP, Sequencer board and NI-interface

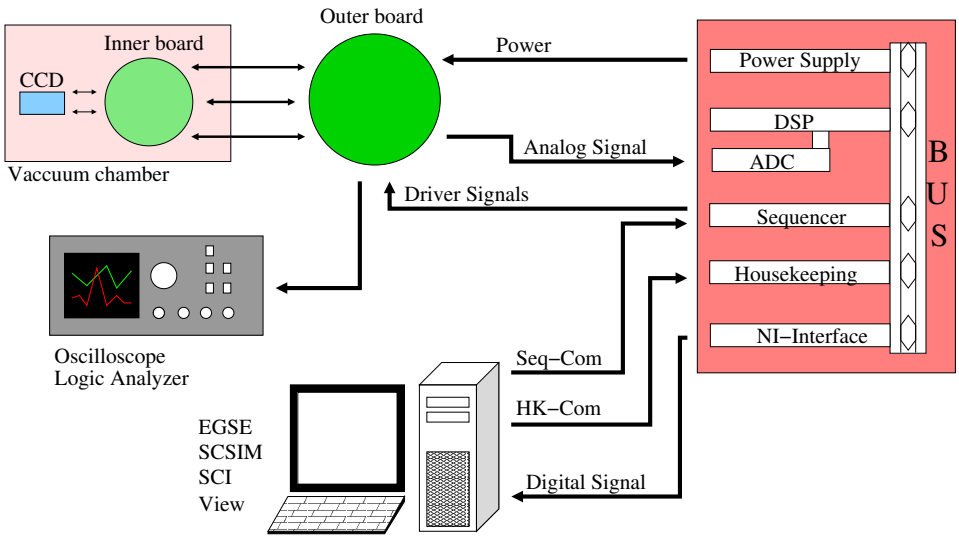

Figure 5.4: Flowchart of the experimental setup.

Table 5.1: Voltages and currents for the operation of the pn-CCD `C11_12_45`. [Meidinger, priv. com.]

Name	Function	Value
`RK`	back-contact	-230 V
`PHI_HIGH`	phi123,456 amplitude "high"	-16 V
`PHI_LOW`	phi123,456 amplitude "low"	-23 V
`GR`	guard ring	-21 V
`FFDr`	first-FET drain	+4 V / 25 mA
`RFGA`	reset first-FET gate anode	10 V
`Vss`	negative supply voltage board	-3.3 V
`Vdd`	positive supply voltage board	+3.3 V
`Vsss`	negative source voltage JFET	-3.2 V
`Vsst`	negative supply voltage	-3.3 V
`Vddt`	positive supply voltage	+3.3 V
`Vssd`	negative CAMEX supply voltage	-3.3 V
`Vddd`	positive CAMEX supply voltage	+3.3 V
`VBST`	CAMEX current source supply	$\approx$ -3.4 V
		so that IFFDr=25 mA
`I_REF_A`	CAMEX: JFET amplifier	13 mA
`I_REF_V`	CAMEX: CDS filter	6 mA
`I_REF_S`	CAMEX: sample & hold	120 μA
`IB1`	CAMEX: serializer	150 μA
`IB2`	CAMEX: serializer	150 μA
`GNDt`		$\approx$ 80 mV

Power Supply Board: The power supply board (DUO-DC Prototype #6) generates the necessary voltages to operate CAMEX, CCD and the other boards in the DAQ rack. With five potentiometers the voltages `FFDr`, `Vss`, `Vdd`, `Vsss`, and `Vssl` (currently not in use) can be adjusted. The other voltages for the CCD's operation can be set via the EGSE software. The supply voltages and currents used to operate the CCD are shown in table 5.1. The high voltage for the back contact is not generated by the power supply board. Instead this is being provided by an external high-voltage power supply "Delta Elektronika" (type E300-0.1).

Housekeeping-Controller: The housekeeping board is the main communication interface of the DAQ rack. It is controlled by the EGSE software, interprets its commands and sends them over the SPI bus to the other boards.

ADC and DSP: The raw analog signal from the CAMEX output has to be digitalised in order to be further processed. A 14-bit two-channel *analog digital converter* (ADC) digitalises the differential analog output signal from each CAMEX. The sampling clock for the ADC is generated by the sequencer and

transmitted from the outer board by an RJ45 connector. The ADC card itself is a piggy-back on the *digital signal processer* (DSP) board, which multiplexes the two 128 channel input lines back to the full 256 channel row.
In addition the DSP can perform corrections to the data like an offset-map substraction or noise- and commonmode-corrections. By default the DSP is in the `IDLE` state in which the data is unprocessed.

NI-Interface: After the raw analog data has been digitalised (and preprocessed) it is sent to the National Instruments-interface (NI) over a 9-pin D-SUB connector. The data is transmitted to a NI-PCI FPGA card[7] via a shielded 68 pin which is hard-wired to the board.

Sequencer Board: The sequencer board was developed at the IAAT. The board contains a "Swatter-board" from DD&T with the sequencer (see below) and a serial EPROM[8] for its configuration. It can be controlled either over the SPI interface or over a separate parallel interface. It was found out that the sequencer frequently startes its configuration over the SPI interface, possibly due to an error in the Swatter-board. In this case the sequencer does not configure itself correctly, and therefore the SPI interface was disconnected and the parallel interface is used.

5.3 Sequencer

The sequencer generates timing and readout signals necessary to operate the CCD. It is realised in a "Swatter-board" which contains a Xilinx Virtex II FPGA[9] and it was developed for the CCD experiment at the IAAT (Schanz, 2007). The sequencer is configured by an EPROM, which contains the program of the sequencer and the look-up-tables (LUT) that determine the timing of all generated signals and the behaviour of the CAMEX. The timing is based on an crystal oscillator with a frequency of 66.666 MHz (the `CLK`-signal). The LUTs contain in detail:

Row-Sequence: The sequencer look-up-table `SEQ_LUT` contains the timing of a row sequence. The most important signal generated is the sequencer-"clock" (`SCLK`) signal, all other generated signals for both CCD and CAMEX are synchronised to it like for example the phi-pulses. These are six logic pulses, which determine the transport of charges in the CCD (see section 4.3.2). In order to operate the CCD in the *framestore mode*, two sets of three pulses (`phi123` and `phi456`) are

[7] NI PCI-7813R 3M Gate Digital R Series Reconfigurable I/O Device

[8] **E**rasable **P**rogrammable **R**ead **O**nly **M**emory

[9] **F**ield **P**rogrammable **G**ate **A**rray, a semiconductor device which contains programmable logic blocks, which can perform basic logic operations. An FPGA "program" refers to a circuit structure which is written in a hardware description language like *VHSIC Hardware Description Language* (VHDL).

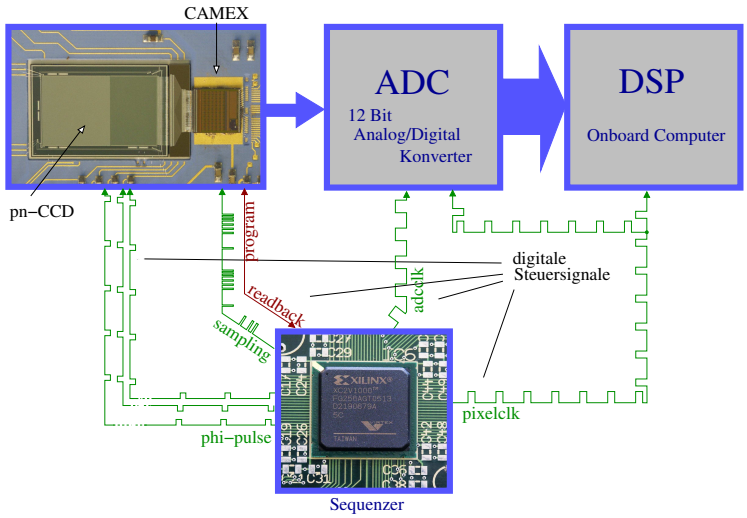

Figure 5.5: A diagram of the sequencer and its generated signals. The CCD shown is a DUO framestore pn-CCD. Image courtesy of Thomas Schanz

needed. The first is used for the fast transfer of the frame into the framestore area after the integration time, the second set transfers the image afterwards slowly to the readout. By changing the timing of the phi-pulses, other readout modes can be achieved. In the *fullframe mode* the pulses are synchronised and timed for slow readout, so that the whole CCD is read out as if it were a non-framestore CCD. By changing the order of the phi pulses the charges can be shifted backwards (*reverse test mode*). In the *2-register mode* the image is integrated under two phi-registers. This should improve the split-event statistics as a larger area for integration should reduce the number of split events (in the forwards-backwards direction). In addition to the readout-sequence the sequencer also generates the signals that multiplex the CAMEX output to the output driver and the timing signals for the ADC and DSP.

CAMEX-Sequence: The 64 × 16 bit CAMEX control register `CMX_LUT` determines the timing of the CAMEX readout sequence described in section 4.3.4. It operates the dynamic switches in the CAMEX like the connection between the CCD and the CAMEX (`S_IN`) or the eight switches of the correlated double sampling (`S1-8`).

CAMEX status register: The CAMEX has an 11-bit programmable status register, that controls its static gain parameters. Unlike the dynamic control register, the values in the status register remain constant during the readout cycle. Apart from the CAMEX gain, the status register also allows to switch the

CAMEX input to a TEST-input. The CCD can be disconnected and a test signal can be applied to the CAMEX to verify its gain and to operate the CAMEX and the readout electronics without a CCD. Each "test" register connects every third channel (for example: 1,4,7,10 etc) to the test-input. The status switches can are shown in figure 4.10.

The LUTs of the sequencer can be changed during its operation. The behaviour of the sequencer and the different signals can be changed comfortably to find the optimal timing settings.

5.4 Readout and Control Software

The software needed to operate the DAQ-rack has been written by Sigfried Müller from MPE. The different programs allow the access of the racks components via the housekeeping board as well as options to display and save the data.

SCSI The spacecraft simulator (SCSI) is the telemetric control interface for the EGSE software. Other hosts can be specified if SCSI and EGSE are running on different computers. The program is written in LabVIEW[10].

EGSE The *electronic ground support equipment* (EGSE) software controls the housekeeping board. Commands for the power supply, DSP, ADC and the sequencer can be prompted in a command window. The commands have the form `ML CMDXX`, where `CMD` is the command associated with a certain housekeeping parameter like a generated voltage and `XX` its hexadecimal value. The housekeeping parameters, including the generated voltages and supply currents, can be read out in a housekeeping window. Due to slight inaccuracies in the displayed voltages, the CCD voltages were calibrated by the bridges on the outer board.
The commands for a full "power-on" or "power-off" sequence were summarised in `PON/POFF` batch files respectively which can be run with the `RUN` commando. In the `PON` batch, the ADCs attenuation is set and the operating voltages are slowly increased to their final value. Breaks for manual input to increase the back contact voltage or start and upload of the sequencer are included . The `POFF` batch shuts the voltages slowly down. The commands for the `PON` batch are shown as an example in appendix A.

Analog-View Analog-View is like the Spacecraft Control a program made in LabView. The program accesses the NI-PCI FPGA card and reads out the frame data. Due to the display speed, the online images in View only show every fourth frame. Five folders contain different options for data readout. The

[10] **L**aboratory **V**irtual **I**nstrumentation **E**ngineering **W**orkbench, a visual programming language by National Instruments

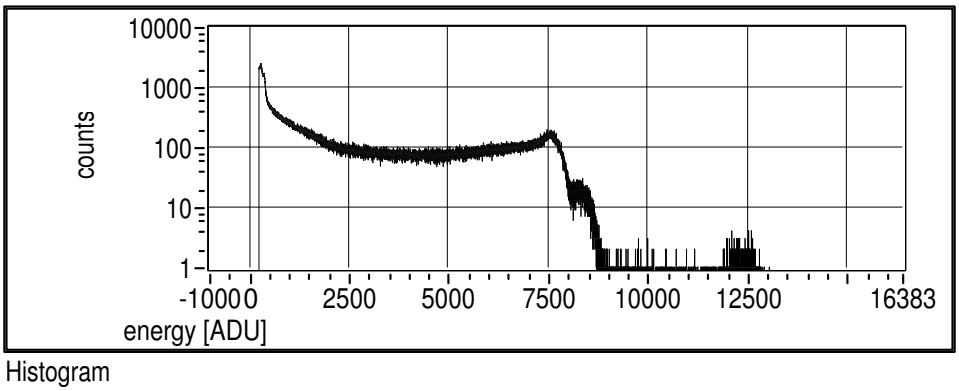

Figure 5.6: A raw spectrum of an ^{55}Fe source recorded with View. The characteristic "bathtub" shape of the split events can be seen as well as the Kα and Kβ peaks at 7 500 and 7 700 ADU respectively.

folder *Pixel data* shows line-wise all 65 536 pixel values. A mean value and a standard deviation is calculated. *Image* shows an online image of the raw data which are transmitted. Any area of the image can be enlarged to examine certain details of the CCD. A mean over all lines and all rows is shown, as well as an unprocessed spectrum. Common mode and the offset can be subtracted. In the *Offset & Noise* folder an offset map and a noise map can be calculated for a specified number of frames. These maps are stored and can be applied to the online image. In addition, the noise map can be shown as a noise spectrum. *Frame data* shows general information of each frame and a frame map with the hexadecimal ADC-values of each pixel. In the *Logging* folder a number of frames can be saved in either the `DAT` or the `FRAMES` format for further processing. A raw spectrum recorded by View is shown in figure 5.6.

Sequencer Control Interface Apart from control through the housekeeping board over the SPI interface, the sequencer can also be controlled and programmed over its parallel interface. The *Sequencer Control Interface* software by Christoph Tenzer can access this interface via an USB2 controller (Schanz, 2007).
The program contains a control panel and two register panels for CAMEX and sequencer. Over the control panel the general function of the sequencer can be switched (Standby / Running), the operating mode of the sequencer can be changed (Framestore, FullFrame etc.) and a log file for the operations of the software is shown. Both register panels allow to change the respective look-up table for CAMEX and sequencer and in addition the CAMEX control register can be modified. Modified LUTs can be saved, loaded from a file or uploaded to the sequencer.

TempWatch A LabVIEW routine that monitors the temperature diode on board via a separate NI-DAQ rack.

5.5 Data Analysis: FITS-Pipe

A problem that is encountered in testing and analysing the data of modern detectors is the multitude of programs that are needed to acquire data, process it into the desired format, analyse it and represent the data in an adequate manner. Often, only a single detector system can be read out with the same set of routines. For this reason, the FITS-Pipe was created (Schwarzburg, 2005). The aim of this project is to provide an analysis software based on the common astronomical data format FITS[11] for a multitude of different X-ray detectors, which is able to process the data online and in real time. The pipe consists of individual program packages (ftools) which are called by a pipeline driver. Even though the pipeline is under development, many ftools are already fully functional and can be used for data processing. FPIPE and ftools are based on the CFITSIO library from the HEASARC (High Energy Astrophysics Science Research Centre). Its main advantage is the use of *extended file name syntax*, which allows basic data processing of the FITS file on its call. A single FITS file can contain multiple sets of data which are stored in different *header data units* (HDU). Calling `data.fits[FRAME1]` would call the HDU of the specified name or `array.fits[0:128,0:128]` would only select the first 128×128 values of a data array.
As an input, a FITS file is expected that contains in each HDU the raw (unprocessed) detector data in form of pulse height amplitudes (PHA). A common measure for PHA is the ADU value from the ADC.
The FITS-Pipe is currently being developed by the *IAAT* and the *Astronomical Institut of Erlangen-Nuremberg*.

FPFrames2FITS: Converts a file from frames format into a FITS file. Detector type, number of rows, number of columns and the number of frames which are to be converted can be specified.

FPCalcOffset: For each pixel the mean value, the median and the standard deviation are calculated for a specified number of `n` frames. Each dataset is written into a separate HDU of an output error-file containing the statistical errors (`[AVERAGE]`,`[MEDIAN]` and`[RAWNOISE]` by default).

FPCommonMode: First, the offset is subtracted from each pixel of the raw data, in this case the Frames2Fits output (the offset can be given as either the `[AVERAGE]` or `[MEDIAN]`). Afterwards, the median for each line is calculated and subtracted (the number of CAMEXs per row and the number of CAMEX channels have to be specified). A line in this context refers to the output of a single CAMEX.

FPCalcNoise: The pixel values from the CommonMode output are sorted by their height and the highest 3% are discarded because they might stem from events.

[11] Flexible Image Transport System

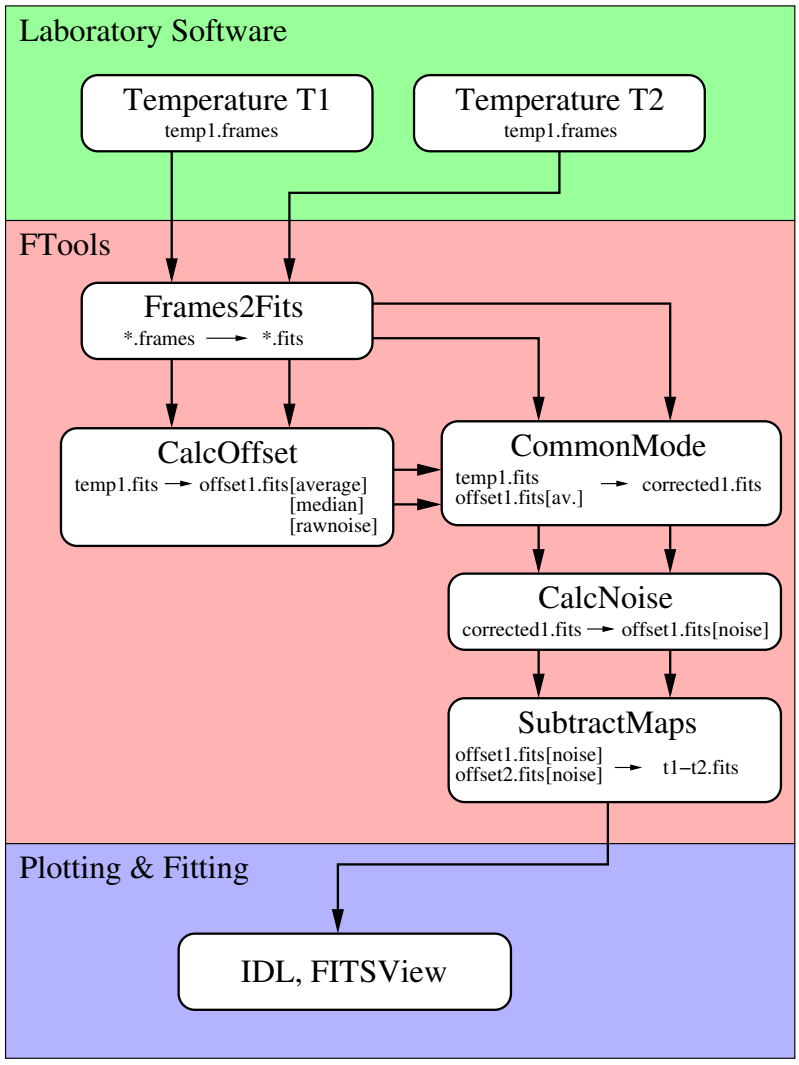

Figure 5.7: Flowchart of the data analysis. The noise at two different temperatures is calculated and the difference plotted in an external program like IDL.

The standard deviation is calculated for each pixel and written into another HDU of the error-file (named `[NOISE]` by default).

FPSubstractmaps: Two single maps (or HDUs) are substracted from each other and written into a file.

FPResidualOffset: A single map is line-wise common mode corrected (the median is calculated and subtracted).

FPGetFrames: A single frame from the Frames2Fits or the CommonMode output is written into an image file.

FPFindEvents: The FPCommonmode output is searched for event-patterns or MIPS. The event list is written into an output file containing frame number, position of the split partner, PHA of the split partner, pattern type (the same classification of split pattern as has been used for XMM-Newton, shown in figure 5.8) and pattern number.

FPSpectrum: The event list is written into a spectrum containing the PHA and the number of events.

FPCalcGain: The weighted average for each event in the event list is being calculated and written into a gain-map for the detector. For the correlation of PHA to energy, a known energy is needed for example the Mn-Kα line at 5.9 keV. The gain is given in eV/ADU.

FPApplyGain: The gain is multiplied with the PHA of each event and each pattern partner to obtain the pixel-dependent energies.

FPPlot2: Plot utility to produce spectra, x-y plots intensity curves etc.

Not all the corrections needed for a full calibration were available at this point, so only a preliminary analysis of a full spectrum is possible. However, the statistic F-tools were applied to great success for the data analysis of noise- and offset maps. In figure 5.7 an exemplary work flow for the difference in an offset map at two different temperatures is shown.

5.6 Optical illumination

One of the main goals of this thesis was to illuminate the CCD with optical light in order to test the shielding performance of the optical coating that is applied to the imaging area of the CCD. This CCD is coated with 100 nm thick layer of Al on Si_3N_4 and SiO_2 (solid yellow line in figure 5.9) [Meidinger, priv. com.]. In this section the experimental set-up for the tests is discussed.

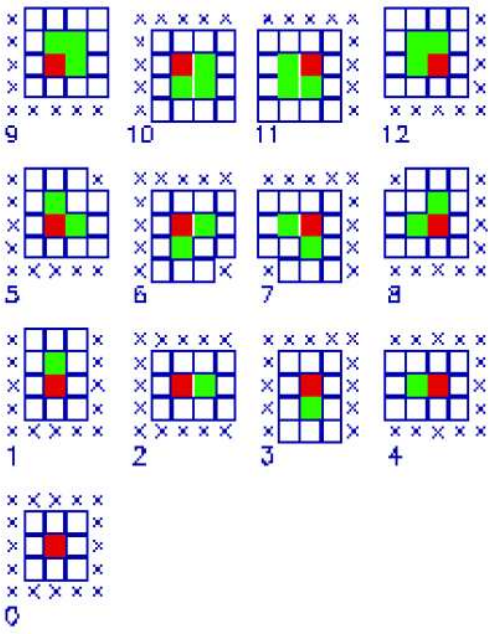

Figure 5.8: Allowed split-event patterns and their pattern type (Turner et al., 2001).

5.6.1 Determination of the Photon Flow

To achieve a clearly visible signal the illumination has to surpass a certain intensity while one the other hand not saturating the detector. Therefore a flow of $\approx 1 \frac{\text{photon}}{\text{frame·pixel}}$ was aimed for, which would cause a clearly visible change in the offset. The luminous intensity of commercial light-emitting diodes (LED) is usually given in candela. For an application, the intensity in candela has to be converted into $\frac{\text{photon}}{\text{frame·pixel}}$ on the CCD surface.
A **candela** is the luminous intensity, in a given direction, of a source that emits monochromatic radiation of frequency $540 \times 10^{12}\,\text{Hz} = 555\,\text{nm}$ and that has a radiant intensity in that direction of $\frac{1}{683} \frac{\text{Watt}}{\text{Steradian}}$. The luminous intensity for a certain wavelength is given by:

$$I_\nu(\lambda) = 683\bar{y}(\lambda)I(\lambda) \tag{5.1}$$

Where $I_\nu(\lambda)$ is the luminous intensity in candela, $I(\lambda)$ the radiant intensity in $\frac{\text{W}}{\text{sr}}$ and $\bar{y}(\lambda)$ the standard luminosity function seen in figure 5.10. The luminosity function is a measure for the eyes sensitivity, which means that our perceived intensity of for example blue light is only a tenth of the actual intensity.

$$[P] = \text{Watt} = \frac{J}{s} = \frac{6.242 \times 10^{18}\,\text{eV}}{s} \tag{5.2}$$

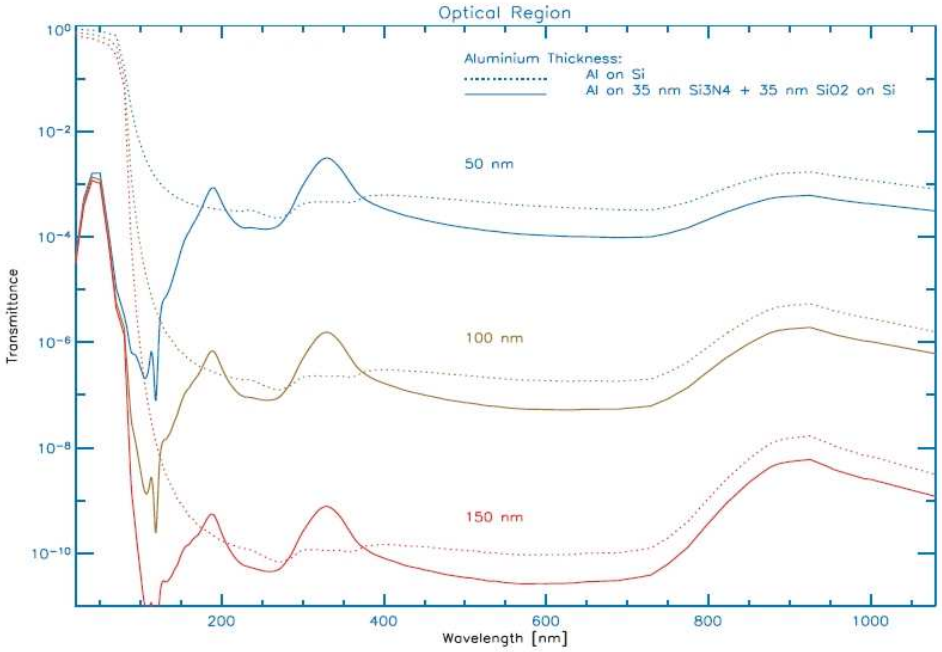

Figure 5.9: The transmittance of radiation in the optical and adjacent energy regions. A different depth and composition of the absorption layer yields a characteristic absorption feature. (Meidinger et al., 2004b)

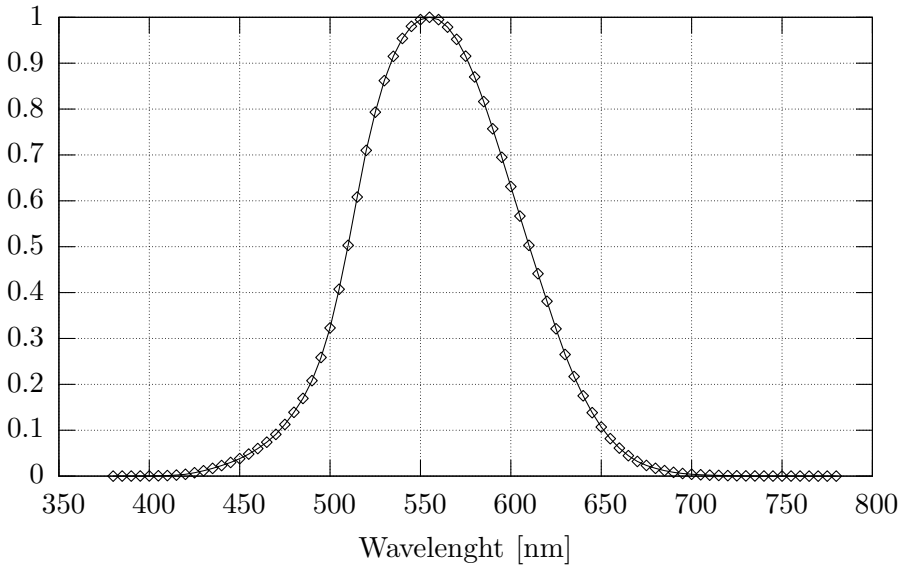

Figure 5.10: The standard photopic luminosity function taken from the Commission Internationale de l'Eclairage (CIE), CIE 1931. [www.cie.co.at]

And since the energy of a single photon is given by

$$E[\mathrm{eV}] = \frac{hc}{\lambda} = \frac{1240\,\mathrm{nm}}{\lambda\,[\mathrm{nm}]}\mathrm{eV} \tag{5.3}$$

it becomes

$$[P] = \frac{6.242 \times 10^{18}\,\mathrm{eV}}{s}\frac{\lambda}{1240\,\mathrm{nm}\cdot\mathrm{eV}} = 5.03 \times 10^{15}\lambda\,[\mathrm{nm}]\frac{Photons}{s} \tag{5.4}$$

So one Watt would equate to $2.79 \times 10^{18}\,\frac{\mathrm{Photons}}{\mathrm{s}}$ when using green photons with $\lambda = 555\,\mathrm{nm}$. The radiant intensity of one candela however would be:

$$\begin{aligned} I(\lambda) &= \frac{1\,\mathrm{cd}}{\bar{y}(\lambda)} \\ &= \frac{1}{683}\frac{\mathrm{W}}{sr}\frac{1}{\bar{y}(\lambda)} \\ &= \frac{5.03 \times 10^{15}}{683}\cdot\lambda\,[\mathrm{nm}]\frac{Photons}{s\cdot sr\cdot\bar{y}(\lambda)} \\ &= 7.36 \times 10^{12}\cdot\lambda\,[\mathrm{nm}]\frac{Photons}{s\cdot sr\cdot\bar{y}(\lambda)} \end{aligned} \tag{5.5}$$

A **steradian** is the solid angle subtended at the centre of a sphere of radius r by a portion of the surface of the sphere having an area r^2. Thus, an area of $1\,\mathrm{m}^2$ at the surface of a sphere of 1 m will cover the solid angle of 1 sr.
The CCD and the luminous source are almost exactly 30 cm apart and the CCD has an area of $1.92\,\mathrm{cm} \times 1.92\,\mathrm{cm} = 3.69\,\mathrm{cm}^2$. Since a steradian would cover an area of $900\,\mathrm{cm}^2$ in a distance of 30 cm, the CCD would be $\frac{3.69\,\mathrm{cm}^2}{900\,\mathrm{cm}^2} = \frac{1}{244}$ of this surface and therefore have a solid angle of $\frac{1}{244}sr$. The CCD was hereby assumed to be part of the spheres surface, even though it is not the case. The error however can be considered small.
The radiant intensity of a one candela source would therefore become, considering that the readout time for one frame is $\frac{1}{20}\,\mathrm{s}$ and a frame contains $256 \times 256 = 65536$ Pixel:

$$\begin{aligned} I_{\mathrm{CCD}}(\lambda) &= 7.36 \times 10^{12}\frac{1}{244}\cdot\lambda\,[\mathrm{nm}]\frac{Photons}{s\cdot\bar{y}(\lambda)} \\ &= 30.2 \times 10^{9}\lambda\,[\mathrm{nm}]\frac{Photons}{s\cdot\bar{y}(\lambda)} \\ &= 1.51 \times 10^{9}\frac{\lambda\,[\mathrm{nm}]}{\bar{y}(\lambda)}\frac{Photons}{Frame} \\ &= 23.0 \times 10^{3}\frac{\lambda\,[\mathrm{nm}]}{\bar{y}(\lambda)}\frac{Photons}{Pixel\cdot Frame} \end{aligned} \tag{5.6}$$

Table 5.2: Properties of the HSMx series SMD-LEDs. The intensities are given in millicandela for the respective test currents. (Agi, 2004)

Colour	Group Number	$\lambda_{\mathbf{Peak}}$ [nm]	I_ν [mcd]	Dice
red	HSMC-A400-S30M1	626	160-400 (50mA)	AlInGaP
red orange	HSMJ-A401-T40M1	615	250-800 (50mA)	AlInGaP
orange	HSML-A401-U40M1	605	400-1260 (50mA)	AlInGaP
amber	HSMA-A400-T35M1	590	250-630 (50mA)	AlInGaP
emerald green	HSME-A401-P4PM1	567	40-130 (50mA)	AlInGaP
green	HSMM-A401-S4YM2	525	160-500 (30mA)	InGaN
cyan	HSMK-A400-T80M2	505	300-1000 (30mA)	InGaN
blue	HSMN-A401-P7QM2	470	50-130 (30mA)	InGaN

Thus, for a source of 1 cd with 555 nm (which would give a value for $\bar{y}(\lambda)$ of 1), a total of $12.8 \times 10^6 \frac{\text{Photons}}{\text{Pixel}\cdot\text{Frame}}$ would hit the CCD. However, since the CCD is coated with a 100 nm thick aluminium layer to prevent low energy photons from entering the CCD, the total number of photons entering the CCD has to be multiplied with the transmittance coefficient for the according wavelength (the coefficients can be seen in figure 5.9 and for the whole optical spectrum, the transmittance is of the order 10^{-7}). In addition, the quantum efficiency of the bulk material greatly differs at the different wavelengths, which can be seen in figure 4.11. However, the absorption coefficient is incorporated into the quantum efficiency, since in this case the quantum efficiency is the efficiency of the whole camera system including the optical shielding. The number of photons for the exemplary green light source (555 nm) emitting 1 cd interacting with the bulk material is thus reduced to

$$I_{\text{CCD,int}}(\lambda) \quad = \quad 2.30 \times 10^{-3} \frac{\lambda\,[\text{nm}]}{\bar{y}(\lambda)} \frac{Photons}{Pixel \cdot Frame}. \tag{5.7}$$

So the total photon flow would be $I_{\text{CCD,int}}(555\,\text{nm}) = 1.28 \frac{\text{Photons}}{\text{Pixel}\cdot\text{Frame}}$. For light sources of a different strength and wavelength, these values have of course to be adjusted. The according values for the used Agilent HSMx series surface-mounted-device (SMD) light-emitting diode (LED) can be found in both tables 5.2 and 5.3. If it is assumed that the interaction probability is still sufficiently high in this energy region, each photon will create one electron-hole pair. Since a single electron has an energy equivalent of ≈ 4.6 ADU, light sources of this or a comparable strength should cause a clearly visible difference in offset. To achieve a photon flow of that order one of any one LED of the Agilent HSMx series can be used, apart from amber (requires 2 LEDs), green (requires 3 LEDs) and emerald green (requires 10 LEDs). In addition all LED have to operated at their nominal current (50 mA and 30 mA respectively)

Table 5.3: The photon flux for the HSMx series LEDs, which is used for illumination. To achieve a photon flow within the same magnitude, ten emerald green, three green, two amber and one of each other LED was used

Colour	$\lambda_{\mathbf{Peak}}$ **[nm]**	$\bar{y}(\lambda)$	**transmittance** $\alpha(\lambda)$	$I(\lambda)[\frac{\text{Photons}}{\text{Pixel}\cdot\text{Frame}}]$
red	626	0.32	10^{-7}	0.72-1.80
red orange	615	0.44	10^{-7}	0.80-2.57
orange	605	0.57	10^{-7}	0.98-3.08
amber	590	0.76	10^{-7}	0.44-1.12 ($\times$2)
em. green	567	0.98	10^{-7}	0.05-0.17 ($\times$10)
green	525	0.79	10^{-7}	0.24-0.76 ($\times$3)
cyan	505	0.41	10^{-7}	0.85-2.83
blue	470	0.09	10^{-7}	0.60-1.56

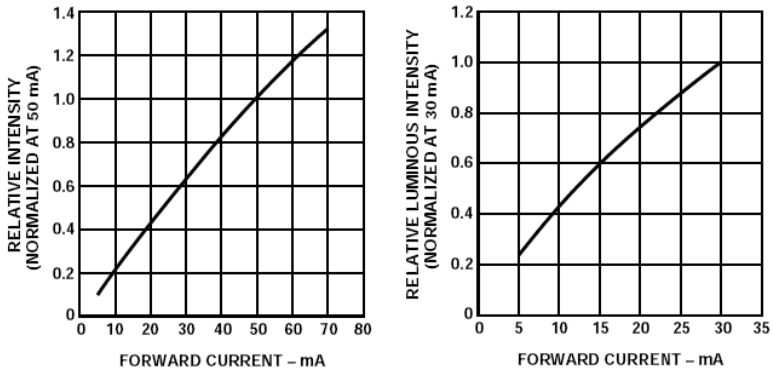

Figure 5.11: The relative intensity of the Agilent HSMx-A4xx series SMD-LEDs. On the left, the characteristics of the AllnGaP diodes (red, red orange, orange, amber and emerald green), on the right that of the InGaN diodes (green, cyan and blue).

5.6.2 LED Board

The main point that had to be considered when designing the LED board and its mount is the low pressure environment. Regularly used electrical components can emit vapours which could contaminate the vacuum or even destroy the component (like for example electrolyte condensators). In addition, the board is to be operated from outside the chamber which requires a feed through on the back flange. As commercial lead throughs like the used VACOM VBBP-1B-10 do not usually have more than a 10-pol connector, the input signal has to be multiplexed outside the vacuum and demultiplexed inside. The demultiplexer inside the vacuum is realised with an Altera MAX 7000 series CPLD[12] so that each LED colour group and every single of the ten emerald green LEDs can be switched on separately. The forward current of the LEDs can be modified with a potentiometer outside the chamber. The luminosity curves in respect to the forward current for the Agilent HSMx series is shown in figure 5.11. The design of the board (see figure 5.6.2) is by Jörg Bayer, its circuit plan is shown in appendix A.
In order to measure the optical illumination and calibrate the signal, a radioactive source had to be installed as well. For this reason a mount for the back flange was produced by the workshop that contained two spacers for the LED board and a socket for a ∅15 mm radioactive source. A rotary feed through on the backside flange can close the source with a 5 mm aluminium shutter. A technical drawing of the mount on the backside flange is shown in appendix A. The LED board is displaced from the centre of the flange to the same direction as the CCD (25 mm for the board, ≈ 20 mm for the CCD). It can be assumed that the intensity of the LEDs is not below 95% due to the angle.

[12] **C**omplex **P**rogrammable **L**ogic **D**evice, a programmable microchip like an FPGA which does not require a configuration from an external device if switched on.

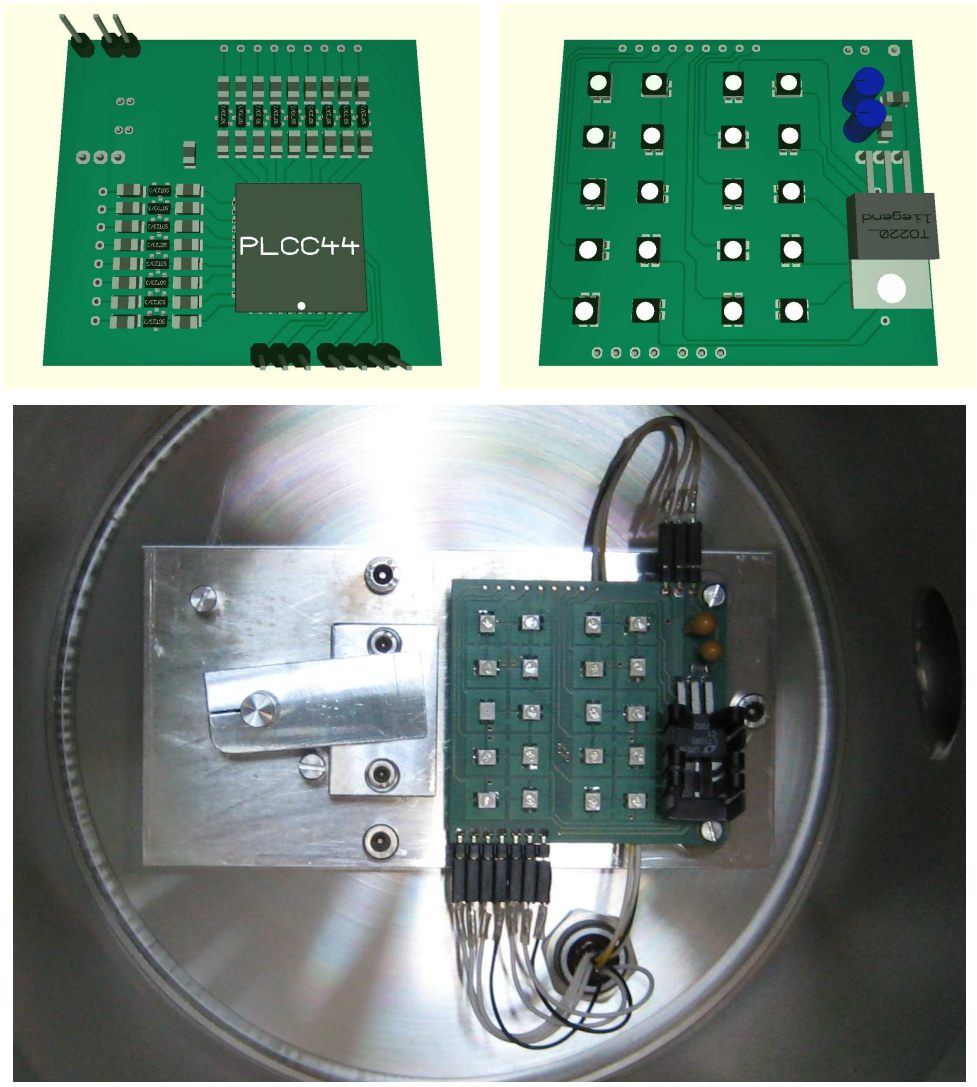

Figure 5.12: A sketch of the LED board (design by Jörg Bayer) and a photo of the LED mount inside the chamber.

Chapter 6

Results

In this chapter the various tests are described that were performed with the CCD. Unless otherwise noted, the default values of sequencer and CAMEX timing were used which are described by Schanz (2007) with the exception of a slightly adjusted `PIXELCLK_delay` signal (25 clock cycles instead of 40). The values of the applied supply voltages were already given in the previous chapter. The default CAMEX status register is (from most to least significant bit):

$\underbrace{0\ \ 0\ \ 0}$	1	$\underbrace{1\ \ 0\ \ 1\ \ 0}$	$\underbrace{1\ \ 0\ \ 0}$
Test-input	MUX-mode	CAMEX gain	bandwidth

With this setting, the Mn-Kα peak of an iron source can be consistently found at 7 500 ADU, which means that one ADU is equal to 0.79 eV.

6.1 First CAMEX Tests

In order to ensure the basic functionality of the experiment before working with the CCD, a number of tests with just the CAMEX were carried out. As already described, the input of each CAMEX channel can either be switched to the first-FET of the CCD or to a separate test-input.
A pulsed test signal is generated by a Hewlett-Packard 8122A pulse generator and transmitted to the CAMEX over an attenuator, which reduces the voltage of the signal by a factor of 100. The generator is triggered by the `frame_clock` signal which marks the beginning of a new CCD frame, so a single pulse is transmitted every frame. The pulse now has to be positioned that it is applied to the CAMEX during the signal sampling but not during the baseline sampling of a single frame which is shown in figure 6.1. A timing signal (`TG`) is set during the time between baseline and signal sampling, the test pulse is applied shortly after. The next row is unaffected because the test pulse stops before the next baseline sampling. Only one third of the CAMEX channels are connected to the test pule (CAMEX status register test-bits: 100), which leads to the comb-like structure of the CAMEX output

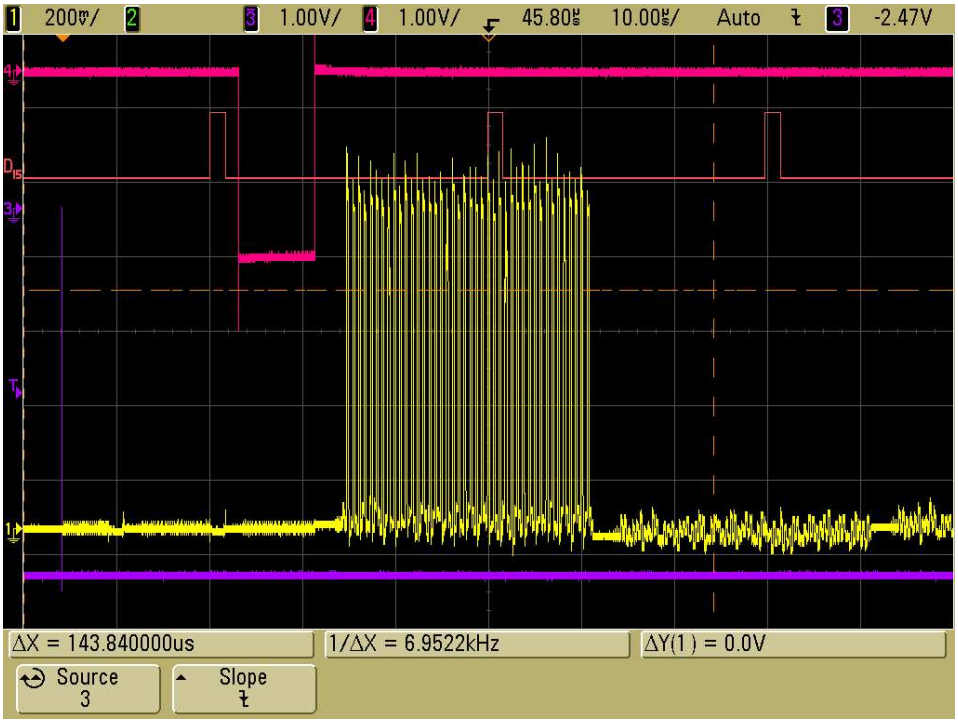

Figure 6.1: Timing of a test signal seen on an oscilloscope with logic analyser. Shown are `frame_clock` (lilac), the test pulse (pink), the analog CAMEX output signal (yellow) and a timing-signal (orange). The CAMEX output shows the analog signal of a single CAMEX (128 channels). The time base of the oscilloscope is set such that two half-rows from a CCD frame are visible, one of which is affected by the test-pulse.

signals in figure 6.1.
The height of the test pulse was varied in order to check the general behaviour of the CAMEX output in relation to a range of input voltages. This is shown in figure 6.2 (top). For input voltages between 0–20 mV (which is the already attenuated value) the CAMEX output is linear. In addition, the number of sampling channels in the CDS filter was stepwise reduced for the respective input voltage. Since the sampled signals from the CDS filter are integrated, the output is also linear with respect to the number of sampling channels. In figure 6.3 the CAMEX gain for a different number of sampling channels is shown. As expected, the gain increases linearly with the number of samplings. The gain of the CAMEX is in this case the mean gain of four selected channels.

In addition, the noise generated by the CAMEX and the ADC was measured while no signal was applied. The number of sampling channels in the CDS filter was stepwise increased from 1 to 8. The CDS does not only amplify the sampled signal by one to eight, it also increases the signal-to-noise ratio. The standard error $\overline{\sigma}$ of a

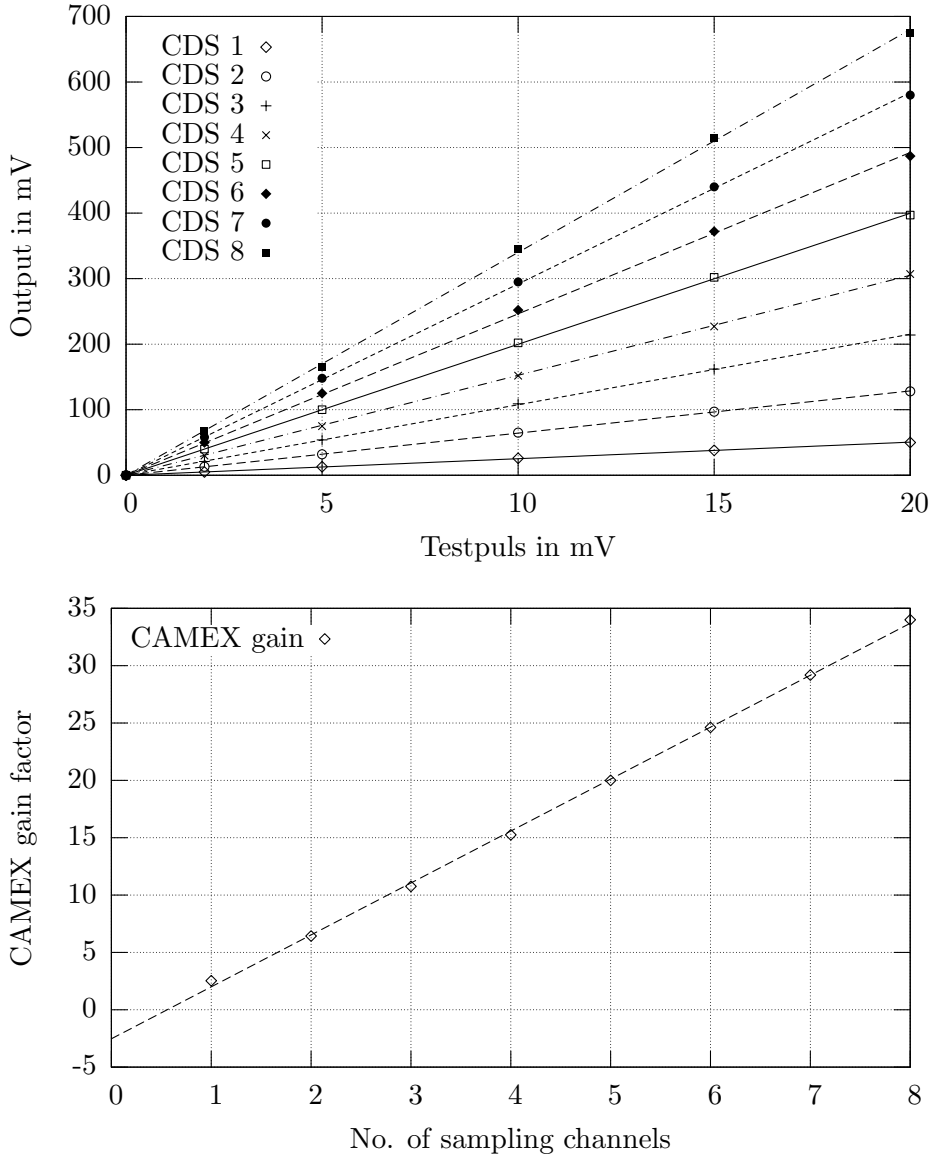

Figure 6.2: Top: CAMEX output with varying strength of a test pulse and a different number of correlated double sampling channels. Bottom: CAMEX gain factor for different numbers of sampling channels. All values are means over four random CAMEX channels from the stimulated row.

measured sample and the standard deviation σ are related to each other by:

$$\sqrt{n} \cdot \overline{\sigma} = \sigma \tag{6.1}$$

where n is the number of samples. Therefore, the total amount of noise will increase

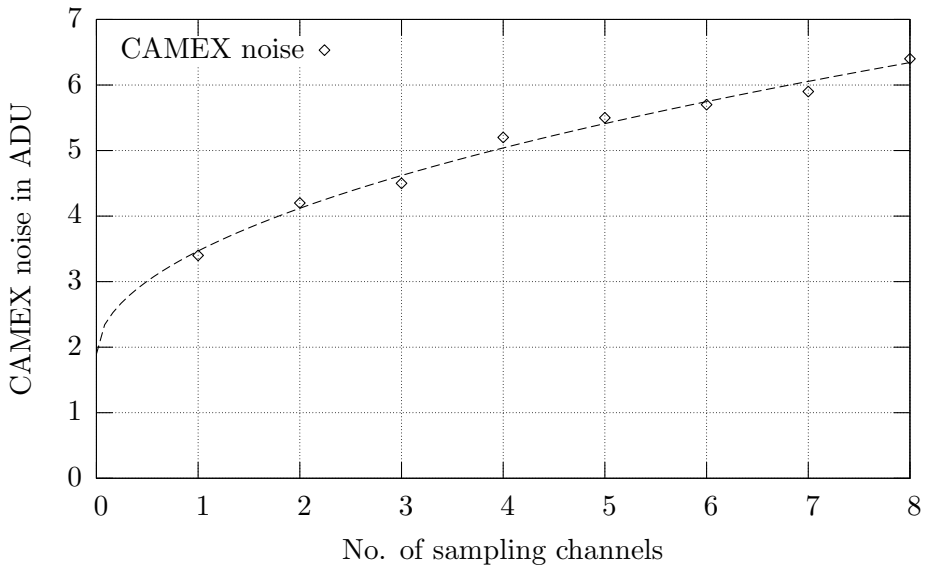

Figure 6.3: CAMEX noise in relation to the number of sampling channels

with more sampling channels, as shown in figure 6.3. The fitted curve shows the square-root behaviour of the noise as well as a noise offset that is caused by the ADC ($\approx$ 1.9 ADU). However, since the value of the signal increases linearly, the signal-to-noise ratio will be improved by the correlated double sampling.

$$\frac{\text{signal}}{\text{noise}} \propto \frac{n}{\sqrt{n}} = \sqrt{n} \tag{6.2}$$

6.2 The ^{55}Fe Spectrum

In order to calibrate the CCD and acquire an ADU-to-eV ratio the CCD was illuminated by an ^{55}Fe source which emits the Mn-Kα and Mn-Kβ lines at 5.9 keV and 6.5 keV respectively. The radioactive source has currently an activity of 29.9 MBq with a photon emission rate of $0.61 \times 10^6\,\mathrm{sr^{-1}s^{-1}}$. The CCD has an area of $(1.92\,\mathrm{cm})^2$ and the source is in a distance of 30 cm, so the CCD covers $\approx \frac{1}{244}$ sr. This equates to a photon flux $\approx 2500\,\mathrm{s^{-1}}$. A 500 frame sample was taken, which recorded a total of 56 804 valid events, which is 91% of the events that are to expected from the source (62 500). The events were sorted by their `Pattern_type` and divided into singles, doubles, triples and quadruples. The spectrum of the different patterns is shown in figure 6.4.
The four pattern-curves show a distinct difference in their behaviour. The singles deposit their energy in just one pixel, so the ADU value in the spectrum is directly

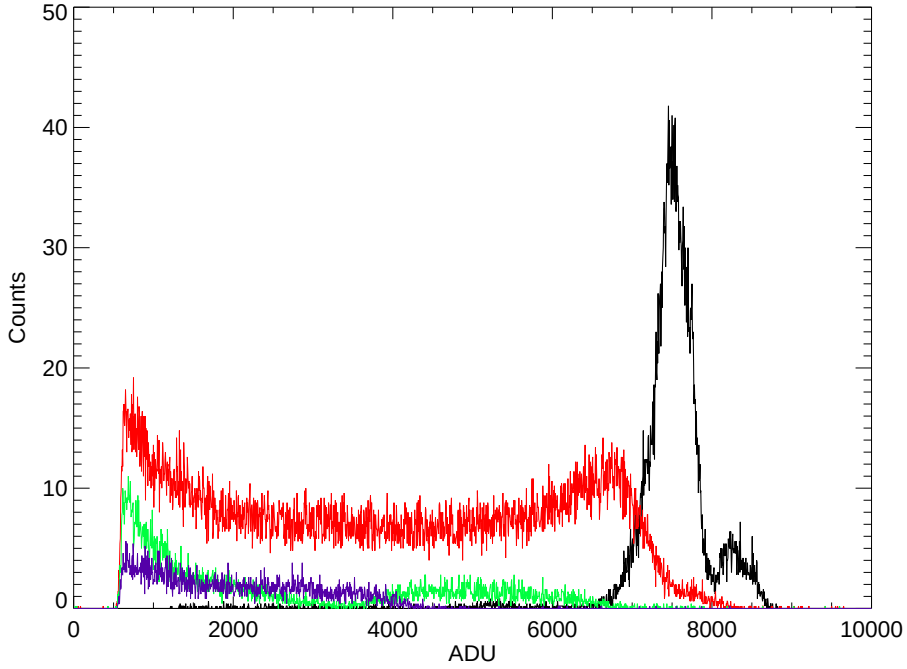

Figure 6.4: Spectrum of a ^{55}Fe source. Shown are the single patterns (black), the doubles (red), the triples (green) and the quadruples (blue).

correlated to the photon energy. The two peaks are caused by the two emission lines. The spectrum of the doubles "bathtub" shaped with a minimal energy at 3 500–4 000 ADU which is half of the single-peaks. This is due to the fact that doubles deposit their energy in two pixels, so both split partners should be distributed symmetrically around half of the energy of the emitted line. Both triples and quadruples usually deposit most of their energy in one pixel and the remaining energy in two or three other pixel, so their spectrum does not increase towards higher energies again like the double's spectrum.
Both the Mn-Kα line at $\approx$ 7500 ADU and the Mn-Kβ line at $\approx$ 8250 ADU are clearly visible in the single spectrum, which leads to an eV-ADU ratio of

$$1\,\mathrm{eV} = 0.79\,\mathrm{ADU} \tag{6.3}$$

for both the Mn-Kα and Mn-Kβ peaks. In order to create a single electron-hole pair, a mean energy of 3.63 eV has to be spent, so the mean ADU value for its creation is 4.59 ADU.

The total number of split events for each respective type is listed in table 6.1. The percentages of the split pattern distribution clearly differ from the values given by Meidinger et al. (2003). This is mainly due to the current status of the analysis

Table 6.1: Split pattern distribution for a ^{55}Fe source.

singles	22852	40.2%
doubles	28711	50.5%
triples	3556	6.3%
quadruples	1685	3.0%
total	56804	100%
invalid	2015	

software. Currently the lower threshold has to be set as high as 500 ADU which is of course far too high to be physically sensible. Doubles with low-energy split-partners are treated as singles hence the broad single peak and the shift of the high energy double peak to lower energies. Triples with one or two low energy partners are treated as doubles or singles and so on. So a recombination without the lowest energy part of the spectrum will result in a much broader overall energy resolution than what is actually observed. However, for a threshold in a more physical region ($\approx$3–5 σ for the split-partner threshold and $\approx$8–10 σ for an event threshold) a treatment of the according datafile was not yet possible. For the same reason, an energy resolution of the spectrum cannot yet be given. In addition the routines for gain correction, charge-transfer efficiency correction and pattern recombination are currently being developed. However, the measured ^{55}Fe spectra are used as a verification of the software's function. A corrected spectrum can hopefully be produced soon.

6.3 Temperature Dependency of Noise and Offset

Before each observation with eROSITA an offset map will be generated and used during the following observation. For an accurate energy measurement it is important that the offset remains constant during the entire observation. Of special interest is the stability of the offset map with temperature. The question remains what effect a temperature change has on the measured data. The CCDs used for the eROSITA telescope are planned to be operated at -80°C.
First the temperature was varied in the range of -115°C to -25°C and the noise was measured every 5°C. The effect can be seen in figure 6.5 (top). Up to a temperature of about -60°C the noise is almost constant at $\approx$ 11 ADU (2.4 ENC). Above that temperature the noise and the standard deviation of the noise increase steeply. The total noise is a compound of electronic noise and temperature effects. Electronic noise is mostly a constant effect of chaotic behaviour of the electrons caused by impurities and traps in the conductors. This effect is only weakly dependent of the temperature. The high-temperature part of the spectrum is caused by thermally generated electron-hole pairs. The spectral photon flux from a body is given by the Stefan-Boltzmann law $\Phi \propto T^4$. The emitted photons can then create electron-hole pairs by inner photo effect. In the operating range of eROSITA, the impact of the

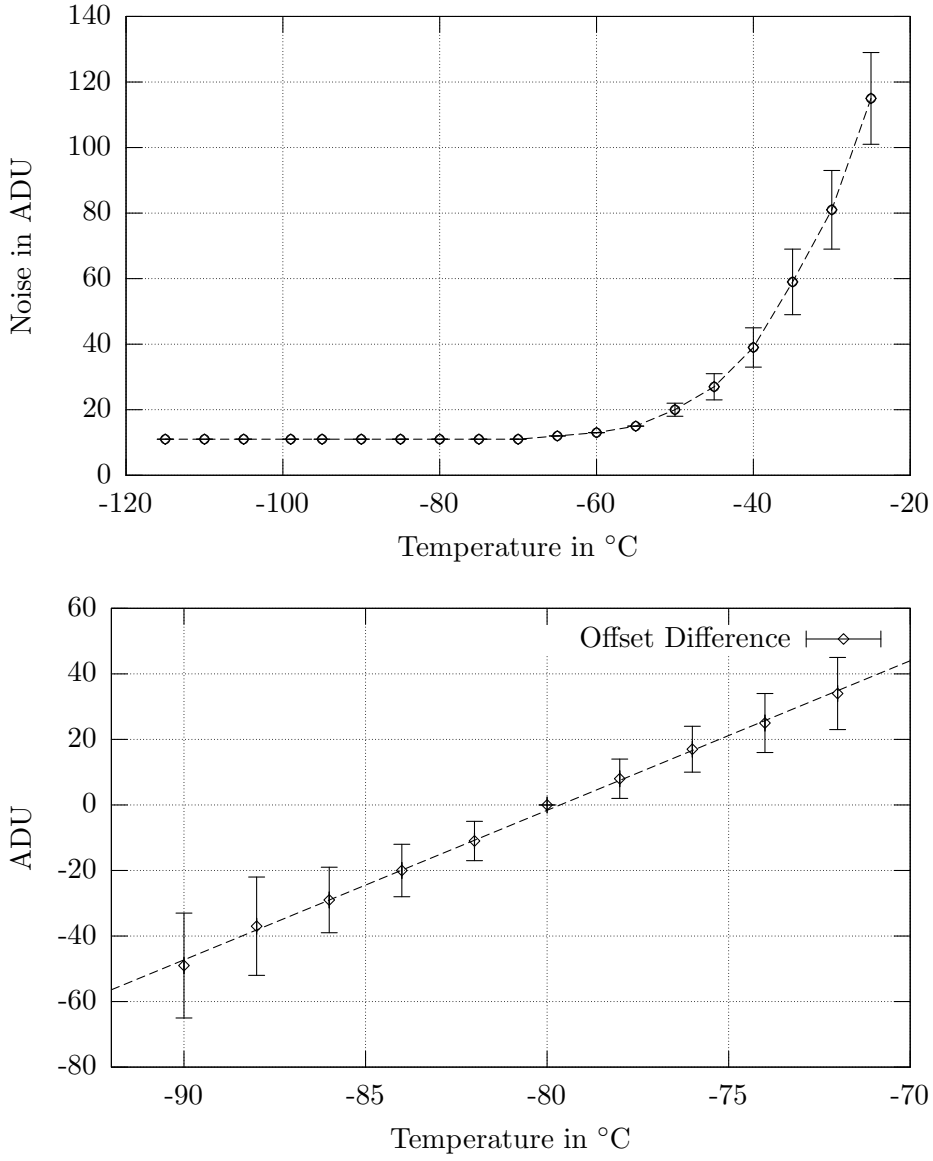

Figure 6.5: Difference in the CCD's noise and offset in relation to the temperature. The error margins in both cases are the standard deviations of the noise at the according temperature.

thermal noise can therefore be considered negligible.
Additionally, the offset was measured in the temperature range from -90°C to -70°C in steps of 2°C, which is shown in figure 6.5 (bottom). The offset-map at -80°C was taken as a gauge for the curve. In this temperature range the offset difference linearly increases with 4.56 ADU/°C. One degree difference would therefore cause an offset difference equivalent to an electron per pixel (0.99 e^-/°C). A stable tem-

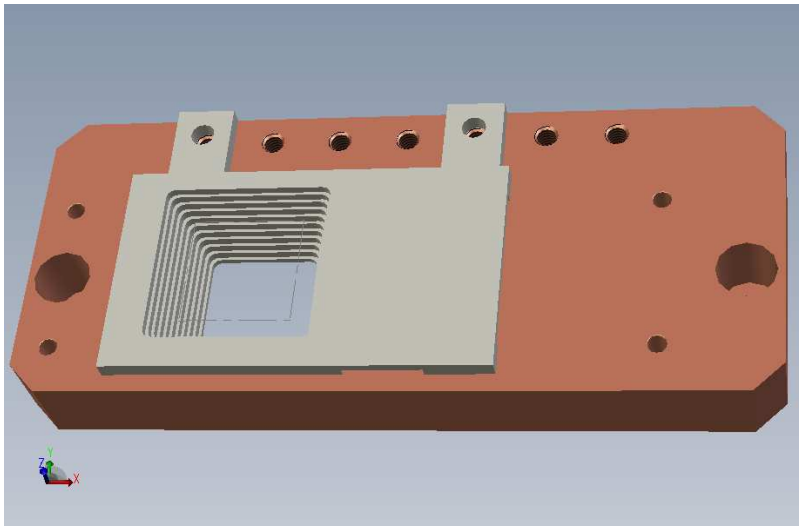

Figure 6.6: Collimator for the cooling mask.

perature environment or frequent offsets are advisable.
The offset in general is mostly caused by the CAMEX as the CDS filter eliminates most of the offset generated by the CCD and the first amplifiers in the CAMEX. The linearity of the offset difference can explained with the Shockley diode equation, which states that the thermal voltage of a diode (in this case: transistors within the CAMEX' operational amplifiers) is dependent on the temperature by $U_T \propto T$.

6.4 Optical Illumination of the CCD

The experimental setup for the illumination of the CCD with optical light was already discussed in the previous chapter. However, when the illumination is used as described with a photon of $\approx 10^7 \frac{\text{photon}}{\text{frame}\cdot\text{pixel}}$ before shielding is taken into account., the CCD is immediately saturated (`I_FFDr` drops to zero). Every LED group shows this behaviour. Only when the forward current is set to a value of about $\frac{1}{5}$–$\frac{1}{10}$ of the nominal current and a less luminous LED is used (for example one or few of the emerald green LEDs from the group of ten), the CCD is not immediately saturated. Even with a very low current, the stronger LEDs (cyan, orange) saturate the CCD with the described setting or bring it close to or over the ADC limit.
All CCD-images in this section show the difference in offset between the illuminated and the non-illuminated CCD. Both maps are taken immediately after each other in order to minimise the influence of temperature effects on the offset. A CCD image in a non-saturated regime is shown in figure 6.7. In this case, a single emerald green LED with a forward current of 6 mA was used (this is a reduction to $\approx 10\%$

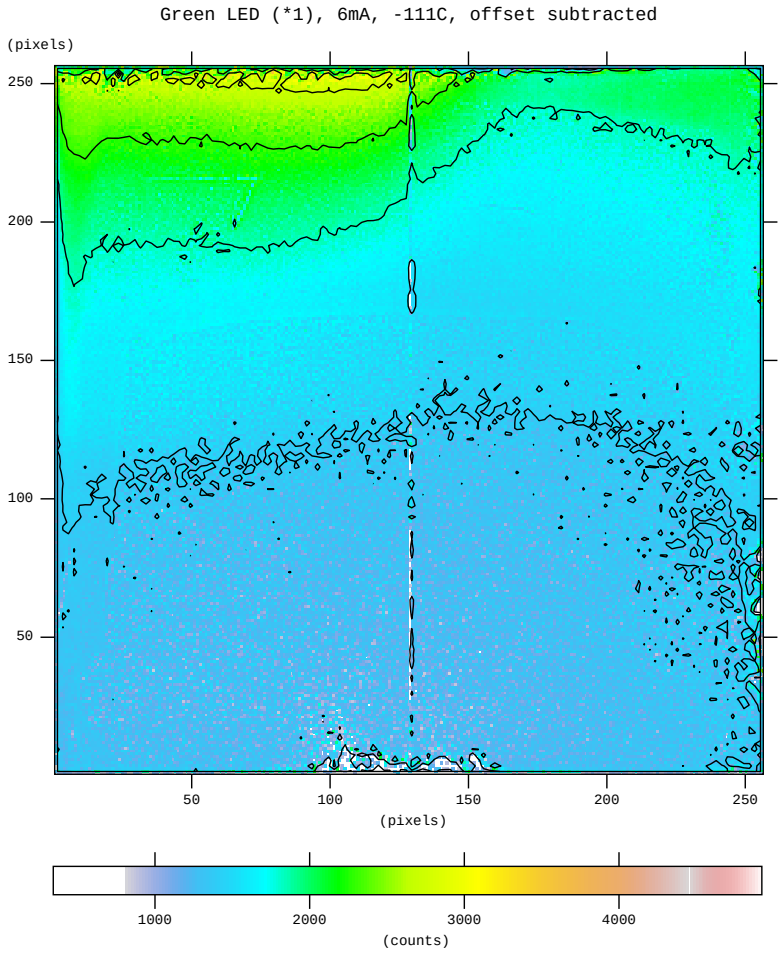

Figure 6.7: Optical illumination with a low-current emerald green LED. The CAMEX chips are located at the bottom.

of its nominal intensity according to figure 5.11). With this setting a photon flux of $10^5 \frac{\text{photons}}{\text{frame}\cdot\text{pixel}}$ is expected on the entrance window of the CCD. There is a clearly visible gradient between the lower part of the image ($\approx 1\,000$ ADU offset difference) and the upper part ($\approx 3\,000$ ADU offset difference). It has to be noted that the LED is operated at the lower border of the operating current for which a corresponding light output is given by the manufacturer (Agi, 2004).
The contour-map highlights the structure of the inhomogeneous illumination. The upper part of the image is the side of the CCD opposite to the CAMEX which is much closer to the edge of the ceramic. It was therefore assumed that light from the LED is either scattered onto the front-side of the CCD by reflection or by transmission through semi-transparent areas of the ceramic. In order to mostly prevent

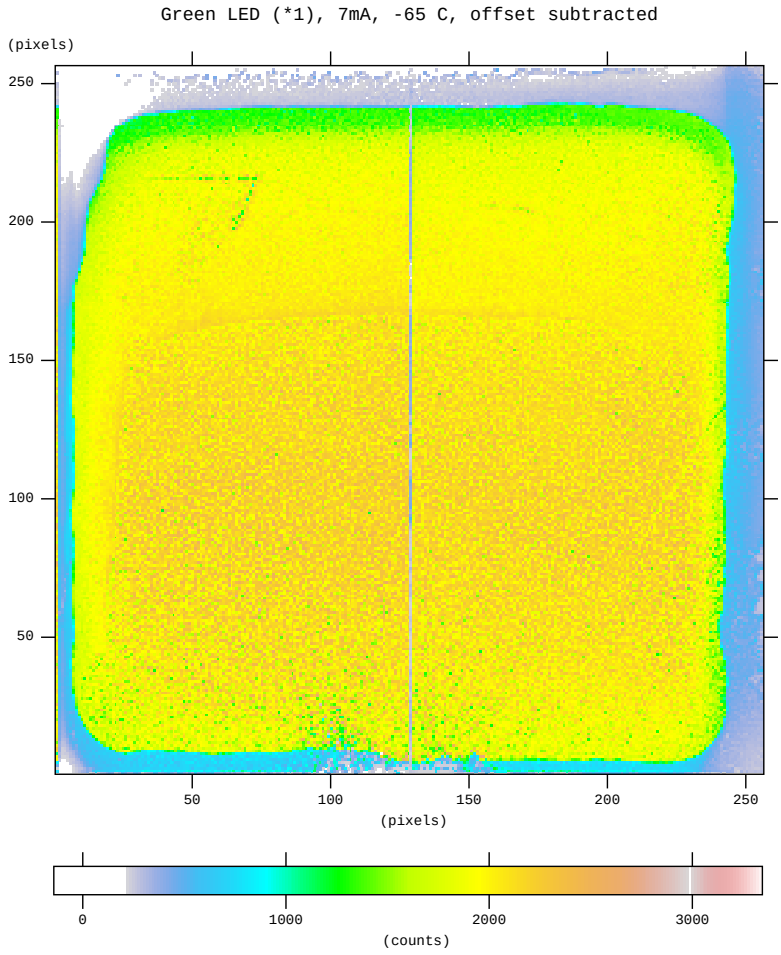

Figure 6.8: Optical illumination with collimator and blackened mask / CCD.

any light from illuminating the front-side of the CCD, an aluminium collimator was manufactured by the workshop which is shown in figure 6.6. The collimator does not only cover the frame store area and the ceramic in the cooling mask's window but also the outmost millimetre of the image area. When installed, the gap between collimator and CCD is 1 mm.
The collimator, the inside of the two-piece cooling mask and the semi transparent parts of the ceramic were coloured black in order to minimise reflection and transmittance. The colour used is the *NEXTEL Primer 5523* in conjunction with the *NEXTEL Suede-Coating 3101* both of which have been kindly supplied to us by the Halbleiterlabor (HLL).
The effect of both collimator and black colour can be seen in figure 6.8. All effects described below can be reproduced with different temperatures and slightly differ-

ent LED currents. The image now shows a margin, which is due to the collimator's geometry. The inhomogeneities of the border region can be explained with either residues of the colour on the milled edges of the collimator or geometrical effects. The only LED that could be used for this measurement is displaced from the centre of the CCD in the direction of the upper righthand corner. Three other notable features are:

- The "separator" line between the left and the right half of the picture. The line in question is line 129 and therefore the first line of the second CAMEX. The image suggests that the first line of each CAMEX are interchanged possibly due to an addressing issue in the readout software.
- The angular structure in the upper left-hand corner. The signal is significantly lower under the structure so that a scratch in the coating can be ruled out. The angle is visible under the microscope on the backside of the CCD in form of a thin trace.
- The upper third of the image is much less grainy than the lower two thirds. In figure 6.9 the spectrum of two 70×70 pixel areas are shown. The spectrum of the upper area is indeed much smoother, however the spectrum for the lower area is only 10% displaced in comparison to the upper spectrum.

The intensity of the transmitted light can also be derived from the map shown in figure 6.9. The two peaks give an exemplary offset difference for two areas which is of the order of 1 000 ADU. This equates to ≈ 220 generated electron-hole pairs and therefore photons per pixel and frame. However, the CCD is only illuminated with one of the ten designated LEDs and in addition it is operated at a tenth of its nominal current. The observed value therefore exceeds the theoretical value of $\approx 1 \frac{\text{photon}}{\text{frame}\cdot\text{pixel}}$ for the nominal current by a factor of $\approx 2 \times 10^4$. A possible explanation of an effect of this magnitude could be an unforseen behaviour of the CCD's coating. The transmittance of different coating thicknesses was shown in figure 5.9 and a coating of for example 50 nm would transmit a factor of 10^3–10^4 more light than the 100 nm coating that was assumed.
The offset difference in the shielded area (under the collimator) ranges from few ten ADU in the upper lefthand corner to about half of the maximum signal on the righthand side. Even if this effect is considered an additional offset for the whole image, it would only explain a factor of two.
The number of electrons that the CCD has to shift and the CAMEX to amplify is of the order of 10^7 per frame, which is not within the CCD's specification. An effect of this "overload" is currently discussed that the anode of the first-FET is not correctly reset. Remaining charges could influence the amplification of the next line and be a possible cause for the "grainy" structure.

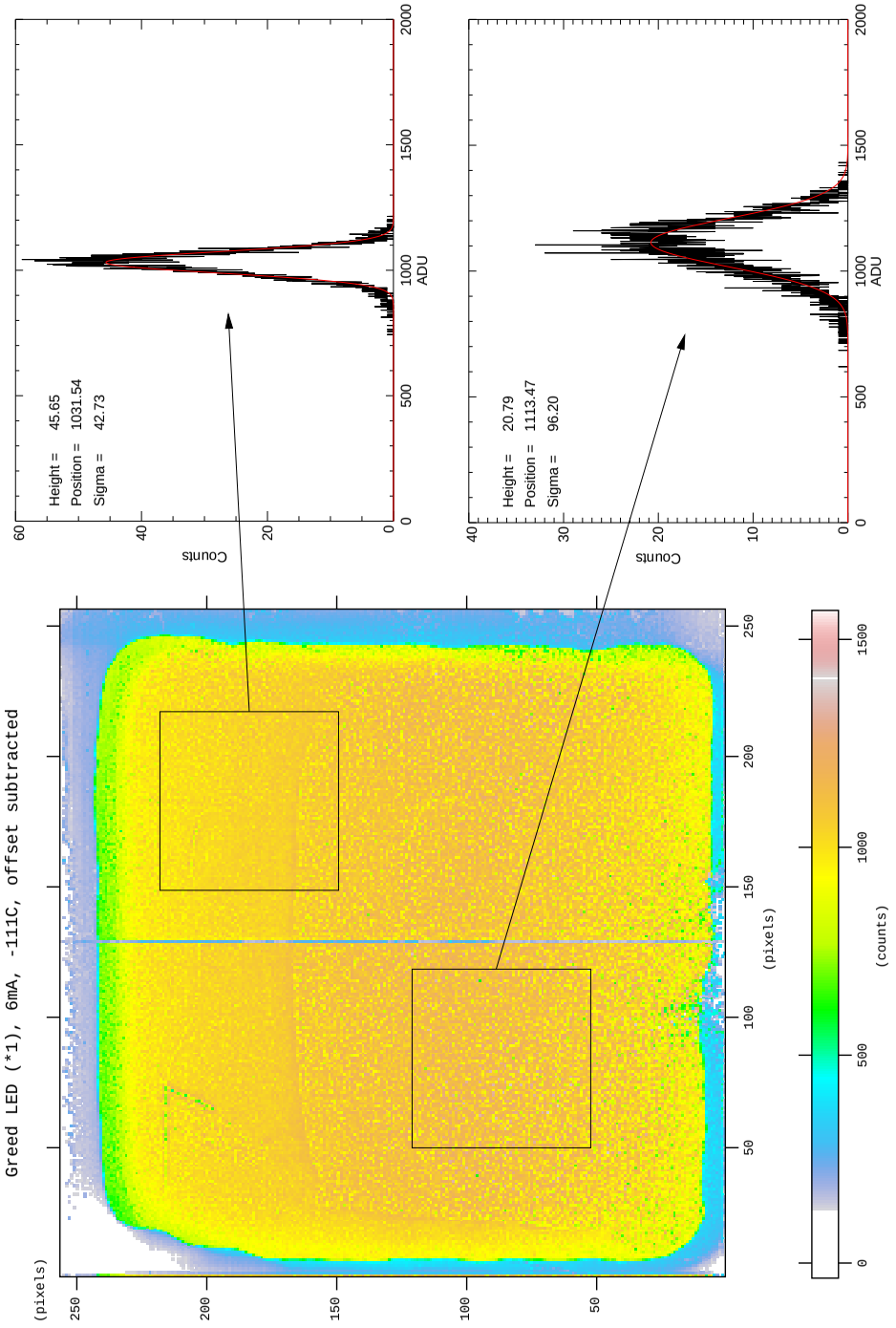

Figure 6.9: Illumination spectra of two select areas on the CCD.

Chapter 7

Summary and Outlook

In this thesis, the framestore pn-CCD experiment at the IAAT has been successfully modified to operate and calibrate the pn-CCD for the eROSITA mission. The basic functionality was tested to ensure the correct behaviour of the CCD. The FTools packages from the FITS-pipe project were first used with detector data to analyse and visualise the measured data. With the instruments available, several measurements were performed. A spectrum of an ^{55}Fe source was used to calibrate the detector and surveys about the behaviour of the CCD when exposed to a temperature change or an illumination with optical light were carried out. However, there are still many open questions and projects.

While the basic FTools of the FITS-pipe are already performing as intended, a full analysis of the spectrum from the iron source was not yet possible. Once the appropriate tools for gain and charge transfer corrections are completed and tested, a true energy resolution and split distribution can be found in order to compare the performance of the detector and maximise its performance. The value given for the ADU-to-eV ratio can be considered almost mature however, as it was derived from the maximum of the emission peak the position of which will not be changed by an additional gain correction and the CTE will only change the position of the peak by $\leq 1‰$.

The most work still needs to be done around the issue that was discovered with the optical illumination. The excess of photons that are measured with the CCD is a factor of 10^4 more than the theoretical value and this behaviour needs to be further tested and explained. A first step is to further eliminate the possibility of photon scattering within the chamber. A collimator in the cooling mask was already used to great effect, but photons which are scattered from the chamber walls between LED board and CCD will still contribute to the signal. Therefore another collimator will be constructed that converges from the sources on the LED mount to the cooling mask. The inside of the collimator tube will be coated with an absorbing colour to prevent scattering within the tube.

In order to operate the CCD with the originally intended photon flux ($\approx 1 \frac{\text{photon}}{\text{pixel}\cdot\text{frame}}$) the LEDs will be operated with their nominal forward currents, however a filter will

be used which absorbs the excess photons. With an illumination of the originally intended magnitude, overloading effects will be ruled out, which are a possible explanation for the grainy structure seen on the CCD. In addition, the integration time will be varied (the current frame-time is 50 ms) to ensure that the seen effect is indeed caused by the in-falling photons. Since signal strength and integration time are directly correlated, an increase in the integration time should increase the signal by the same factor.

A possible explanation for the excess photon flux was a differing thickness of the optical shielding. This could be tested by an illumination with a source in the soft X-ray region. While the transmittance of the shielding is almost constant in the detector range regardless of its thickness, it clearly differs for energies $\approx 0.5\,\mathrm{eV}$. A photon source that emits a gauged flux of photons in this energy region could be used to verify the thickness of the shielding.

In conclusion can be said that even though newer semiconductor detectors are being developed, the framestore pn-CCD is a reliable and well-studied device and therefore a good candidate for satellite missions like eROSITA. It is hoped that with the results of the Spectrum-RG mission with its seven pn-CCDs, more “light” will be shed onto the topic of dark energy and cosmology.

Appendix A

Flange

A drawing of the backside flange and the mount (magenta) for the LED board (green) and the socket for the radioactive source (orange). The flange is a DN 160 ISO-K blank flange. Designed and manufactured by Siegbert Renner and Klaus Lehmann.

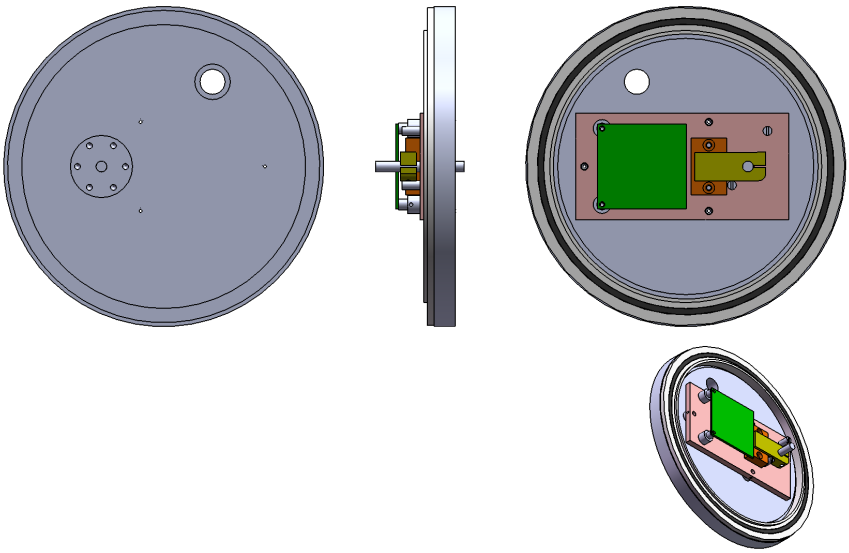

Connectors on the outer board

A sketch of the connectors and bridges of the outer board. Included are the voltages and signals that can be measured at their respective pins or bridges. The denotation of the connectors `STxx` and the bridges `BRxx` is taken from the boards circut plan. [Walter Kink, MPE, priv.com.]

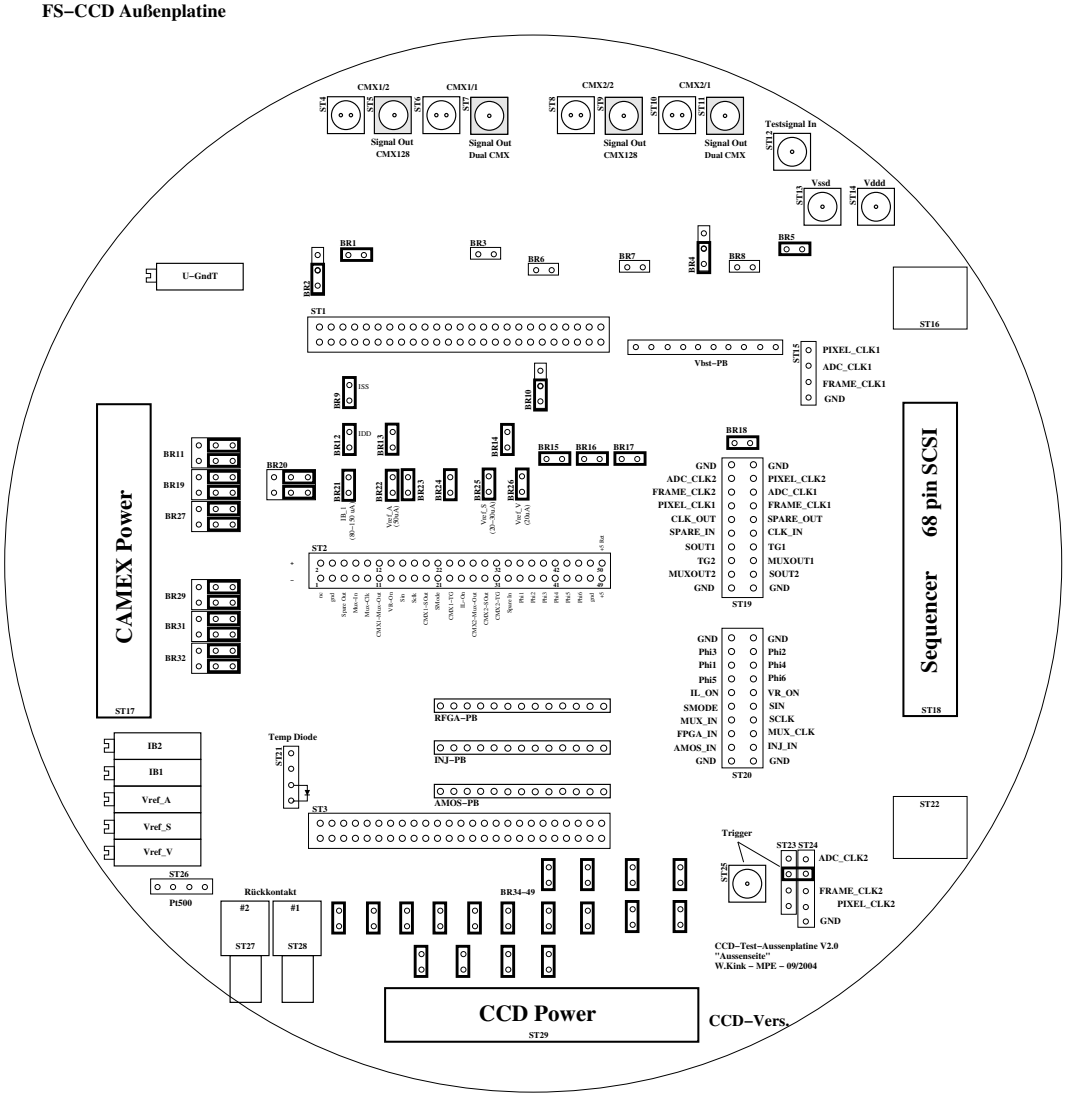

The EGSE Commands of the PON-batch

Prompt	EGSE commando	function
cmd window	`#RUN PON`	starts batch
batch	`#ML PDAC,0,50`	set attenuation ADC 1
	`#ML PDAC,2,50`	set attenuation ADC 2
	`#ML PADC,0000`	set ADC sample at pipeline entry 1
	`#ML PADC,0000`	
	`#ML PADC,0504`	
	`#ML PADC,0001`	
manually	*Switch on back contact power supply*	
	increase back contact slowly to -160 V	
cmd window	`#BATCH CONT`	(continue batch)
manually	*program CAMEX via the sequencer control interface*	
cmd window	`#BATCH CONT`	(continue batch)
batch	`#ML CUGRNG,44`	set U_GRNG to first level
	`#ML CPHI123O,50`	set PHI123 offset to first level
	`#ML CPHI456O,50`	set PHI456 offset to first level
	`#ML CPHI123A,78`	set PHI123 amplitude to first level
	`#ML CPHI456A,78`	set PHI456 amplitude to first level
	`#ML CUGRNG,88`	set U_GRNG to second level
	`#ML CPHI123O,CA`	set PHI123 offset to second level
	`#ML CPHI456O,CA`	set PHI456 offset to second level
	`#ML CUGRNG,88`	set U_GRNG to third level
manually	*increase back contact slowly to -200 V*	
cmd window	`#BATCH CONT`	(continue batch)
batch	`#ML CFFDRON`	set V_FFDR ON
	`#ML CVSSSON`	set V_SSS ON
manually	*increase back contact slowly to -230 V*	
cmd window	`#BATCH CONT`	(continue batch)
batch	`#ML CRFGALP,D8`	set RFGA level
	`#ML CUVBST,78`	adjust U_VBST for I_FFDR=25mA
	`#ML CUVBST,6C`	
	`#ML CUGRNG,88`	toggle U_GRNG
	`#ML CUGRNG,B8`	
	`#ML CUGRNG,CF`	

LED-Board

The circuit plan of the LED board designed by Jörg Bayer.

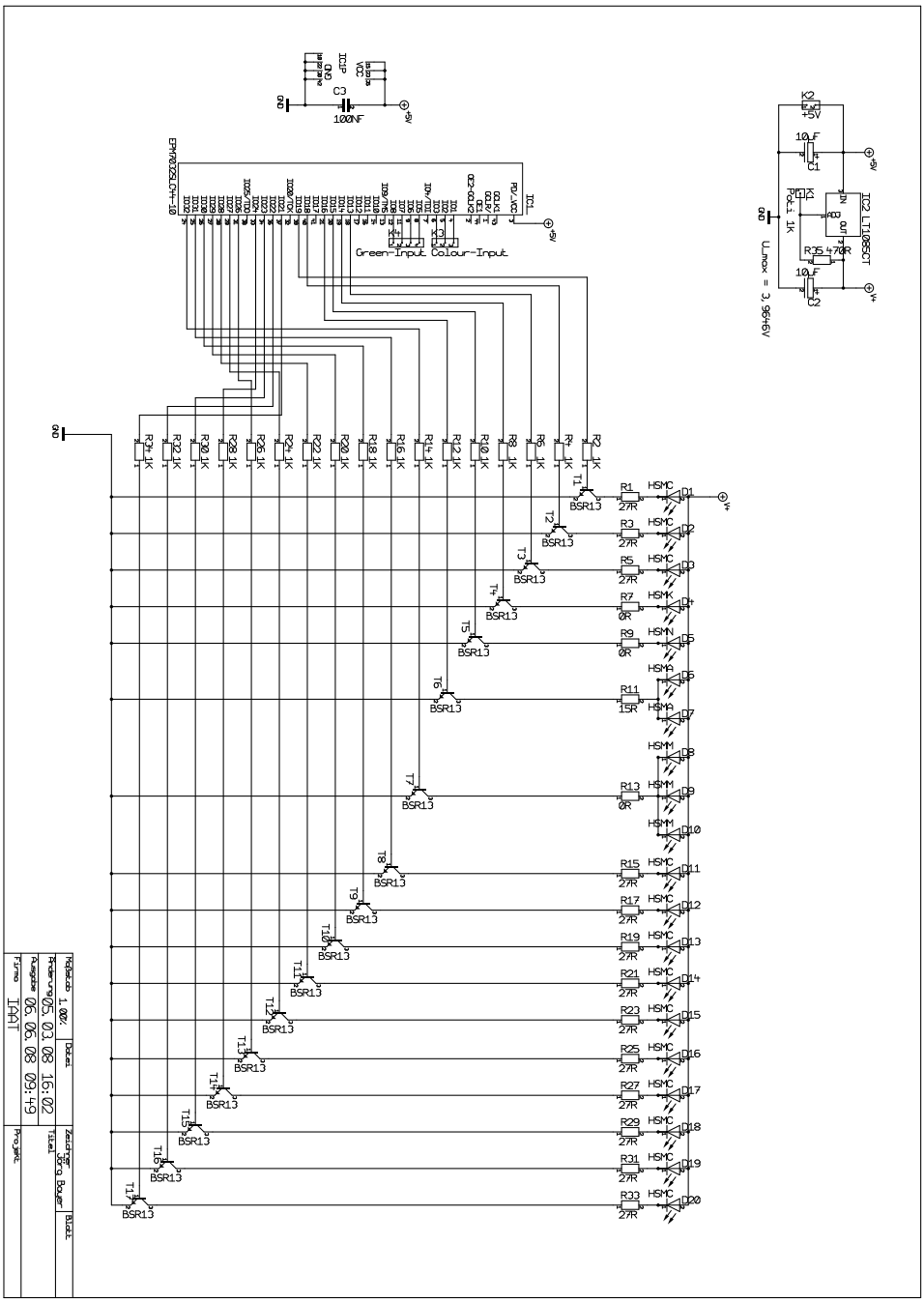

Bibliography

2004, Agilent HSMx-A4xx-xxxxx SMT LED Surface Mount LED Indicator, Agilent Technologies, Inc.

Aschenbach B., 1985, Reports of Progress in Physics 48, 579

Bondi H., Hoyle F., 1944, MNRAS 104, 273

Bravin M., Bruckmayer M., Bucci C., et al., 1999, Astroparticle Physics 12, 107

Burger S., 2005, *Master's thesis*, Institut für Astronomie und Astrophysik der Universität Tübingen

Dabagov S.B., Nikitina S.V., Kumakhov M.A., et al., 1995, Nuclear Instruments and Methods in Physics Research B 103, 99

Dmitriev G., Hasinger G., Parmar A., et al., 2005, SPECTRUM-RG/eROSITA/LOBSTER Mission Definition Document

Eckart A., 2002, Nature 415, 128

Gamov G., 1970, My World Line: An Informal Autobiography, Viking Press

Giacconi R., Gursky H., Paolini F.R., Rossi B.B., 1962, Physical Review Letters 9, 439

Giacconi R., Kellogg E., Gorenstein P., et al., 1971, Astrophys. J., Lett. 165, L27+

Giacconi R., Murray S., Gursky H., et al., 1974, ApJ 27, 37

Hempelmann A., Schmitt J.H.M.M., Schultz M., et al., 1995, A&A 294, 515

Hinshaw G., Weiland J.L., Hill R.S., et al., 2008, ArXiv e-prints 803

Hubble E., 1929, Proceedings of the National Academy of Science 15, 168

in 't Zand J., 1996, Coded aperture camera imaging concept, http://www.sron.nl/ jeanz/cai/coded_intr.html Visited: 29.05.2008

Jansen F., Lumb D., Altieri B., et al., 2001, A&A 365, L1

Lucy L.B., White R.L., 1980, ApJ 241, 300

Lutz G., 2001, Semiconductor Radiation Devices, Springer, 2nd edition

Meidinger N., Andricek L., Bonerz S., et al., 2004a, In: Flanagan K.A., Siegmund O.H.W. (eds.) X-Ray and Gamma-Ray Instrumentation for Astronomy XIII. Edited by Flanagan, Kathryn A.; Siegmund, Oswald H. W. Proceedings of the SPIE, Volume 5165, pp. 26-36 (2004)., Vol. 5165. Presented at the Society of Photo-Optical Instrumentation Engineers (SPIE) Conference, p.26

Meidinger N., Andritschke R., Hälker O., et al., 2006, In: High Energy, Optical, and Infrared Detectors for Astronomy II. Edited by Dorn, David A.; Holland, Andrew D.. Proceedings of the SPIE, Volume 6276, pp. 627618 (2006)., Vol. 6276. Presented at the Society of Photo-Optical Instrumentation Engineers (SPIE) Conference

Meidinger N., Bonerz S., Eckhardt R., et al., 2003, Nuclear Instruments and Methods in Physics Research A 512, 341

Meidinger N., Bonerz S., Englhauser J., et al., 2004b, In: Holland A.D. (ed.) High-Energy Detectors in Astronomy. Edited by Holland, Andrew D. Proceedings of the SPIE, Volume 5501, pp. 66-77 (2004)., Vol. 5501. Presented at the Society of Photo-Optical Instrumentation Engineers (SPIE) Conference, p.66

Pavlinsky M., Hasinger G., Parmar A., et al., 2006, In: Space Telescopes and Instrumentation II: Ultraviolet to Gamma Ray. Edited by Turner, Martin J. L.; Hasinger, Günther. Proceedings of the SPIE, Volume 6266, pp. 62660O (2006)., Vol. 6266. Presented at the Society of Photo-Optical Instrumentation Engineers (SPIE) Conference

Penzias A.A., Wilson R.W., 1965, ApJ 142, 419

Predehl P., Hasinger G., Böhringer H., et al., 2006, In: Space Telescopes and Instrumentation II: Ultraviolet to Gamma Ray. Edited by Turner, Martin J. L.; Hasinger, Günther. Proceedings of the SPIE, Volume 6266, pp. 62660P (2006)., Vol. 6266. Presented at the Society of Photo-Optical Instrumentation Engineers (SPIE) Conference

Reidy W.P., Vaiana G.S., Zehnpfennig T., Giacconi R., 1968, ApJ 151, 333

Riess A.G., Strolger L.G., Tonry J., et al., 2004, ApJ 607, 665

Rosswog S., Bruggen M., 2003, Introduction to High-Energy Astrophysics, Introduction to High-Energy Astrophysics, by Stephan Rosswog and Marcus Bruggen, pp. 376. Cambridge University Press, 2003

Schanz T., 2007, Sequencer für eine Framestore CCD-Kamera, Technical report, Institut für Astronomie und Astrophysik der Universität Tübingen

Schneider P., 2006, Einführung in die extragalaktische Astronomie und Kosmologie, Einführung in die extragalaktische Astronomie und Kosmologie / Peter Schneider. Berlin: Springer, XV+452 pp.

Schwarzburg S., 2005, *Master's thesis*, Institut für Astronomie und Astrophysik der Universität Tübingen

Spieler H., 2005, Semiconductor Detector Systems, Oxford Science Publications

Strüder L., Briel U., Dennerl K., et al., 2001, A&A 365, L18

Truemper J., 1982, Advances in Space Research 2, 241

Truemper J., Pietsch W., Reppin C., et al., 1978, Astrophys. J., Lett. 219, L105

Turner M.J.L., Abbey A., Arnaud M., et al., 2001, A&A 365, L27

Ubertini R., Lebrun F., di Cocco G., et al., 2000, In: McConnell M.L., Ryan J.M. (eds.) American Institute of Physics Conference Series, Vol. 510. American Institute of Physics Conference Series, p.684

Unsöld A., Baschek B., 1999, Der neue Kosmos, Einführung in die Astronomie und Astrophysik, XIV, 571 S. 278 Abb., 20 in Farbe. Springer-Verlag Berlin Heidelberg New York

Urry C.M., Padovani P., 1995, PASP 107, 803

van Albada T.S., Bahcall J.N., Begeman K., Sancisi R., 1985, ApJ 295, 305

Wilms J., 1996, *Master's thesis*, Institut für Astronomie und Astrophysik der Universität Tübingen

Wilms J., 1998, Ph.D. thesis, Institut für Astronomie und Astrophysik der Universität Tübingen

Wilms J., 2002, X-Ray Astronomy 2, http://pulsar.sternwarte.uni-erlangen.de/wilms/teach/xray2/index.html Visited: 16.05.2008

Ziolkowski J., 2002, Memorie della Societa Astronomica Italiana 73, 1038

Zombeck M.V., 1990, Handbook of space astronomy and astrophysics, Cambridge University Press, 1990, 2nd edition

Zwicky F., 1937, ApJ 86, 217

Danksagung

Nur ein Schwein
Säuft allein.
–Volksweisheit

An dieser Stelle möchte ich mich ganz herzlich bei all denen bedanken, die mir geholfen haben, diese Arbeit zu einem Abschluss zu führen. Ob nun in der Form von wissenschaftlichen-technischen Fragen oder von entspannenden Pausen, ohne einen Austausch macht die Arbeit wenig Sinn und Spass. Besonders möchte ich bei folgenden Personen bedanken:

Dr. Eckhard Kendziorra für die Betreuung dieser Arbeit und die zahllosen einfachen Lösungen der "schweren" Probleme.

Prof. Dr. Andrea Santangelo für die Vergabe des Themas und Korrektur dieser Arbeit.

Michael Martin ohne dessen Geduld, Fachwissen und rote Tinte diese Arbeit wohl nie den heutigen Zustand erreicht hätte.

Thomas Schanz für all die interessanten Anregungen und die Motivation als es mal wieder nicht voran ging.

Guiseppe Distratis, meinem Büronachbarn, für die Rückbesinnung darauf, was wirklich wichtig ist, nämlich Kaffee.

Siegfried Vetter und Jörg Bayer für allerlei Hilfe mit der Elektronik, insbesondere Herrn Vetter für die abendlichen Gespräche über Gott und die Welt.

Wolfgang Gäbele, Klaus Lehmann und Siegbert Renner für die prompte und professionelle Anfertigung aller Teile für den Messstand.

Meinen Eltern, die es mir durch die fortwährende Unterstüzung nicht nur im finanziellen Bereich überhaupt erst ermöglicht haben zu studieren.

Stefan Arbeiter und Rosa Freund für guten Zuspruch insbesondere während des Schreibens dieser Arbeit, sowie für zahlreiche "last-minute" Korrekturen.

Erklärung

Hiermit erkläre ich, dass ich die Diplomarbeit mit dem Titel “Chracterisation of Specific Parameters of the Framestore pn-CCD for eROSITA” selbstständig verfasst und dabei keine anderen als die angegebenen Quellen und Hilfsmittel benutzt habe.

Tübingen, den 17. Juni 2008